Alma Mater Studiorum – Università di Bologna

DOTTORATO DI RICERCA IN

CHIMICA

Ciclo XVII

Settore Concorsuale di afferenza: 03/C2 - CHIMICA INDUSTRIALE

Settore Scientifico disciplinare: CHIM/04

TAILORING PROPERTIES AND FUCTIONALITIES OF TiO_2 AND Ag NANOPARTICLES INVOLVED IN SURFACES ENGINEERING PROCESSES

Presentata da: Simona Ortelli

Coordinatore Dottorato

Prof. Aldo Roda

Relatore

Prof.ssa Stefania Albonetti

Correlatore

Prof. Angelo Vaccari

Dott.sa Anna Luisa Costa

Esame finale anno 2015

TABLE OF CONTENTS

Abstract

Nanotechnology is exploited to create new materials using atomic scale tailoring of their properties. Among the most promising nanomaterials are nano-TiO_2 and nano-Ag, which are highly used in surface functionalization, due to their photocatalytic and antibacterial properties. The functionalization of substrates through the application of nanostructured coatings allows to create new materials, with enhanced properties. In recent years, the textile industry has increasingly focused its interest on nanotechnologies, and the functionalization of textile is expected to improve textiles high-grade functionality.

In this work, the development of self-cleaning and antibacterial textiles, through the application of TiO_2 and Ag based nanostructured coatings was carried out. The production of TiO_2 and Ag functionalized materials was achieved both by the classical dip-padding-curing method and by the innovative electrospinning process to obtain nanofibers doped with nano-TiO_2 and nano-Ag. In order to optimize the production of functionalized textiles, starting from lab-made and commercial nanosols, the study focused on the comprehension of mechanisms involved in the photocatalytic and antibacterial processes and on the real applicability of the products. In particular, a deep investigation on the relationship between nanosol physicochemical characteristics, nanocoating properties and their performances was accomplished. Self-cleaning textiles with optimized properties were obtained by properly purifying and applying commercial TiO_2 nanosol while the studies on the photocatalytic mechanism operating in self-cleaning application demonstrated the strong influence of hydrophilic properties and of interaction surface/radicals on final performance. In addition, a study about the safety in handling of nano-TiO_2 was carried out and risk remediation strategies, based on “safety by design” approach, were developed. In particular, the coating of TiO_2 nanoparticles (NPs) by a SiO_2 shell was demonstrated to be the best risk remediation strategy in term of biological response and preserving of photoreactivity. The obtained results were confirmed determining the reactive oxygen species (ROS) production by a multiple approach. Antibacterial textiles for biotechnological applications were also

studied and Ag-coated cotton materials, with significant anti-bacterial properties, were produced.

Finally, composite nanofibers were obtained merging biopolymer processing and sol-gel techniques. Indeed, electrospun nanofibers embedded with TiO_2 and Ag NPs, starting from aqueous keratin based formulation were produced and their functional properties, in degrading organic materials and in killing microorganisms, were assessed. The results confirmed the capability of electrospun keratin nanofibers matrix to preserve nanoparticle properties.

Aim of the work

Nanotechnology is an evolving interdisciplinary area expected to have growing implications in all fields of science and technology such as material science, mechanics, electronics, optics, medicine, energy, and aerospace, plastics and textiles. Therefore, nanotechnology can be applied to several commercial application whereof the textile industry is one of the foremost beneficiary. Starting from 1997, textile industry pioneers were already using nanoparticles to coat on yarns, fiber and fabric to introduce innovation in their production. Indeed, the use of nanotechnology could create radically new textiles and enhance the conventional textiles with greater functionality.

In recent years, several attempts have been made by researchers and industries to exploit the concepts of surface-engineered modifications through nanotechnology to produce high-performance fabrics. In addition to the development of improved textile fabrics and materials, several advances in the area of textile processing have also been made.

Moreover, the expansion of nanotechnologies, occurred in the recent years, has led to a significant increase of interest in the safety of nanomaterials. However, it is widely acknowledged that there is a lack of information concerning the human health and environmental implications of nanomaterials and concerns have been expressed regarding potential risks to health which might arise during their manufacture, use and disposal.

In this regard, the aim of my work was the development of self-cleaning and antibacterial textiles through their functionalization with TiO_2 and Ag nanoparticles. In particular, my work was focused on:

- production of self-cleaning textiles, by classical dip-padding-curing application, starting from TiO_2 nanosol. Deep investigation on the relationship between nanosol properties, nanocoating characteristics and photocatalytic performances was carried out. An exploratory study on the photocatalytic mechanism was

performed in order to identify the factors affecting the photocatalytic reactivity, following a “performance by design” approach.

- development of a risk remediation strategies, based on “safety by design” approach, in order to control and harmonize the biological reactivity of TiO_2 nanoparticles, involved in photocatalytic processes.

- production of antibacterial textiles, using nano-Ag functionalization, suitable for biotechnological applications.

- production of nanoreactive media by embedding of TiO_2 and Ag nanoparticles onto nanofibers. These materials were obtained by electrospinning, and led to improved properties towards bacteria removal (antimicrobial, low bio-fouling) and photocatalytic activity (removal of drugs, antibiotics, pesticides, and fertilizers). A deep study relative to the compatibility between two phases (polymeric phase that constitutes the nanofibrous structure and nanoparticles embedded) was made, preparing stabile and well dispersed electrospinnable formulations.

Chapter 1: NANOMATERIALS

The nanometer (nm) is a metric unit of length, and denotes one billionth of a meter or 10^{-9} m. Popularly, “nano” is also used as an adjective to describe objects, systems, or phenomena with characteristics arising from nanometer scale structure. While “micro” has come to mean anything small, “nano” emphasizes the atomic granularity that produces the unique phenomena observed in nanoscience. While there are some exceptional examples, most of the exciting properties of “nano” begin to be apparent in systems smaller than 100 nanometers. Nanostructured materials did not first come into existence with the recent emergence of the field of nanotechnology. Many existing materials are structured on the micro- and nanometer scales, and many industrial processes that have been used for decades (e.g. polymer and steel manufacturing) exploit nanoscale phenomena. The most advanced nanotechnological fabrication process is microelectronic fabrication, where thin film coatings and lithography are used to create micro- and nanosized features on computer chips. The natural world is replete with examples of systems with nanoscale structures, such as milk (a nanoscale colloid), proteins, cells, bacteria, viruses etc. Moreover, many materials that seems smooth to the naked eye have an intricate structure on the scale of nanometers (Fig. 1.1). Thus in many ways nanomaterials are not new. Recent advances in synthesis and characterization tools, however, have fueled a boom in the study and industrial use of nanostructured materials [1].

1.1 Nanomaterials

Nanomaterials (NMs) are materials that have structural components smaller than 100 nm in at least one dimension. It is useful to classify the NMs based on their number of dimensions (Fig. 1.2a). This is a generalization of the concept of aspect ratio.

- 1D nanomaterials. Materials with one dimension in the nanometer scale are typically thin films or surface coatings, and include the circuitry of computer chips and the antireflection and hard coatings on eyeglasses. Thin films have been developed and used for decades in various fields, such as electronics,

chemistry, and engineering. Thin films can be deposited by various methods [2] and can be grown controllably to be only one atom thick, a so-called monolayer.

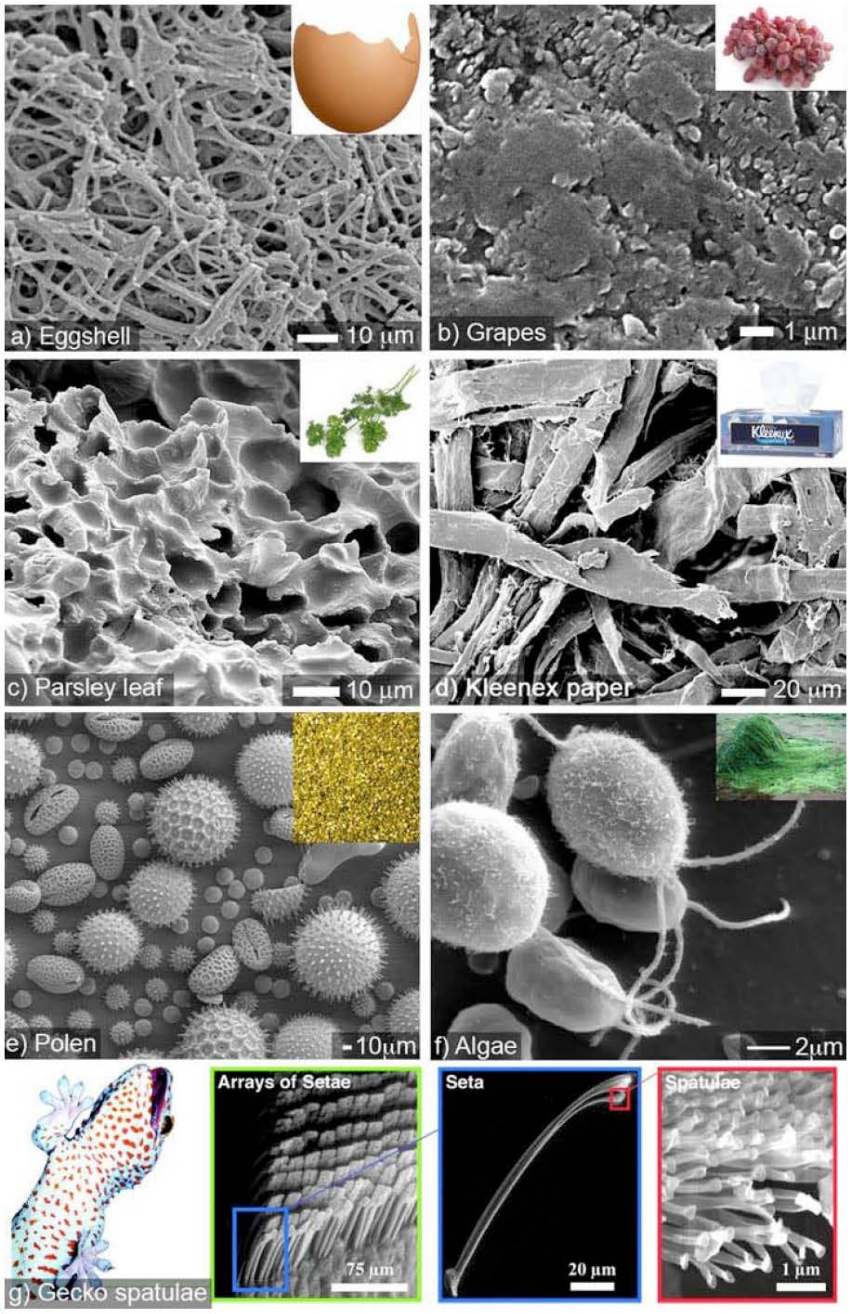

Figure 1.1 SEM images showing the complexity of the world at the micro and nanoscale: a) the inner surface of a bird's eggshell; b) the rough surface of table grape; c) the textured surface of a parsley leaf; d) Kleenex paper; e) pollen from a variety of common plants; f) green algae; g) Gecko nanoadhesive system, with increasing magnification from left to right: gecko climbing vertical glass, adhesive surface microstructure, individual setae, nanostructure of spatular endings [1].

- 2D nanomaterials. Two-dimensional nanomaterials have two dimensions in the nanometer scale. These include 2D nanostructured films, with nanostructures firmly attached to a substrate, or nanopore filters used for small particle separation and filtration. Free particles with a large aspect ratio, with dimensions in the nanoscale range, are also considered 2D nanomaterials. Asbestos fibers are an example of 2D nanomaterials.
- 3D nanomaterials. Materials that are nanoscaled in all three dimensions are considered 3D nanomaterials. These include thin films deposited under conditions that generate atomic scale porosity, colloids, and free nanoparticles with various morphologies.

In alternative, NMs are mainly classified according to morphological structure, composition and agglomeration degree. Morphological characteristics to be taken into account are: flatness, sphericity, and aspect ratio. A general classification exists between high- and low-aspect ratio particles (Fig. 1.2b). High aspect ratio nanoparticles include nanotubes and nanowires, with various shapes, such as helices, zigzags, belts, or perhaps nanowires with diameter that varies with length. Small aspect ratio morphologies include spherical, oval, cubic, prism, helical, or pillar. Collections of many particles exist as powders, suspension, or colloids.

Within the 3D NMs, nanoparticles are very exploited. So, nanoparticles (NPs) are particles with three dimensions smaller than 100 nm and potentially as small as atomic and molecular length scales (~0.2 nm). Nanoparticles can have amorphous or crystalline form and their surfaces can act as carriers for liquid droplets or gases. To some degree, nanoparticulate matter should be considered a distinct state of matter, in addition to the solid, liquid, gaseous, and plasma states, due to its distinct properties (large surface area and quantum size effects). Examples of materials in crystalline nanoparticle (NP) form are fullerenes and carbon nanotubes, while traditional crystalline solid forms are graphite and diamond.

NPs can be composed of a single constituent material or be a composite of several materials (Fig. 1.2c). The NPs found in nature are often agglomerations of materials

with various compositions, while pure single composition materials can be easily synthesized today by a variety of methods (see Section 1.1.1).

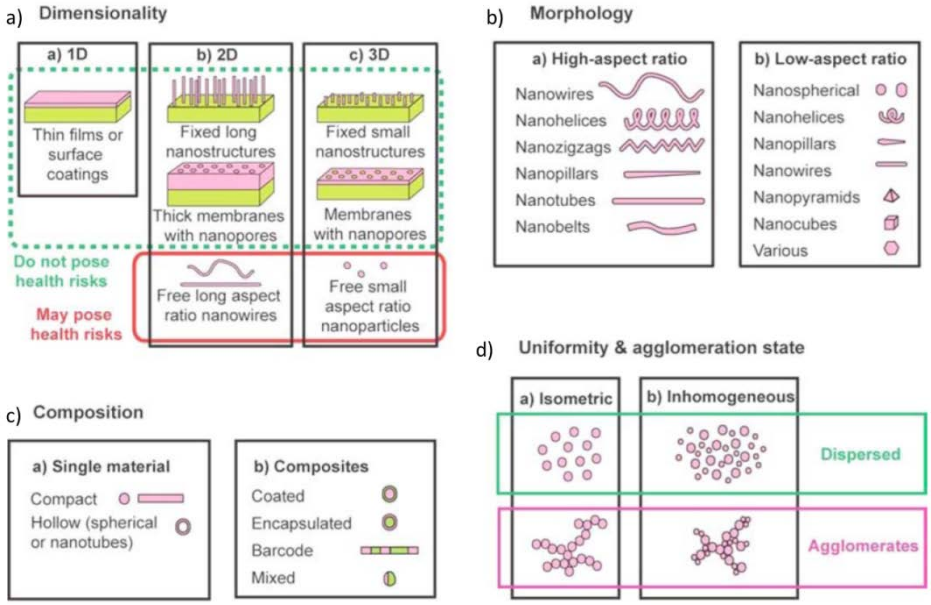

Figure 1.2 Classification of nanostructured materials from the point of view of nanostructure dimensions, morphology, composition, uniformity and agglomeration state [1].

Based on their chemistry and electro-magnetic properties, NPs can exist as isometric or inhomogeneous phases at dry powder or suspensions/colloids, both dispersed or in an agglomerate state (Fig. 1.2d). For example, magnetic NPs tend to cluster, forming an agglomerate state, unless their surfaces are coated with a non-magnetic material. In an agglomerate state, NPs may behave as larger particles, depending on the size of the agglomerate. Hence, it is evident that nanoparticle agglomeration, size and surface reactivity, along with shape and size, must be taken into account when deciding considering health and environmental regulation of new materials. Furthermore, such characteristics influence the engineering processes, in which the NMs are involved.

NMs owe their uniqueness to the synergy between common properties of material, such as conductivity, hardness, melting point and their specific characteristics, as the wave-particle duality and quantum effects. NMs have aroused great interest due to their unusual properties resulting from peculiar nanostructure [3]. When the dimensions are controlled in the range of 1–100 nm, the physical and chemical properties of materials

can be significantly different from those of bulk materials owing to space confinement and surface effects [4,5].

Two primary factors cause NMs to behave significantly differently than bulk materials: surface effects (causing smooth properties scaling due to the fraction of atoms at the surface) and quantum effects (showing discontinuous behavior due to quantum confinement effects in materials with delocalized electrons) [6]. These factors affect the chemical reactivity of materials, as well as their mechanical, optical, electric, and magnetic properties.

The fraction of the atoms at the surface in NPs is increased compared to microparticles or bulk. Compared to microparticles, nanoparticles have a very large surface area and high particle number per unit mass. For illustration, one carbon microparticle with a diameter of 60 μm has a mass of 0.3 μg and a surface area of 0.01 mm^2. The same mass of carbon in nanoparticulate form, with each particle having a diameter of 60 nm, has a surface area of 11.3 mm^2 and consists of 1 billion nanoparticles (Fig. 1.3a).

The ratio of surface area to volume (or mass) for a particle with a diameter of 60 nm is 1000 times larger than a particle with a diameter of 60 μm (Fig. 1.3b). As the material in nanoparticulate form presents a much larger surface area for chemical reactions, reactivity is enhanced roughly 1 000-fold. While chemical reactivity generally increases with decreasing particle size, surface coatings and other modifications can have complicating effects, even reducing reactivity with decreasing particle size in some instances.

The atoms situated at the surface have less neighbors than bulk atoms, resulting in lower binding energy per atom with decreasing particle size. A consequence of reduced binding energy per atom is a melting point reduction with particle radius, following the Gibbs-Thomson equation. For example, the melting temperature of 3 nm gold NPs is more than 300 degrees lower than the melting temperature of bulk gold, as shown in Figure 1.3c [6].

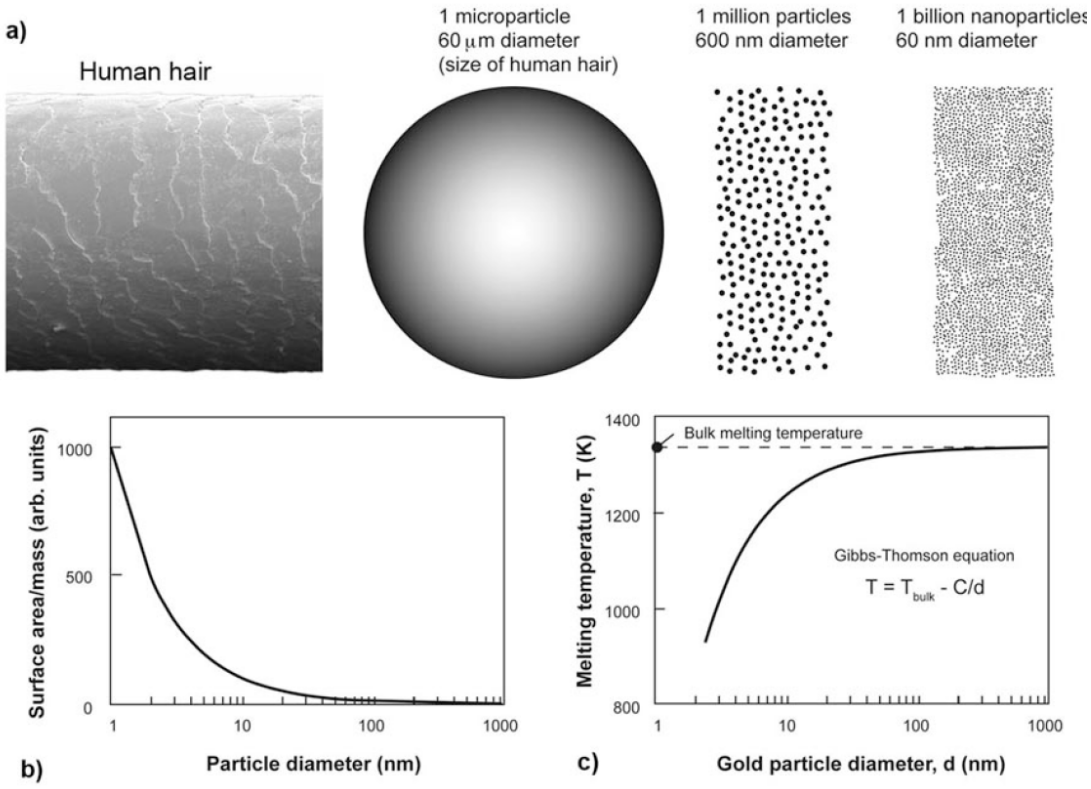

Figure 1.3 a) Schematics illustrating a microparticle of 60 μm diameter, about the size of a human hair - shown in the left at scale, and the number of nanoparticles with diameter of 600 nm and 60 nm having the same mass as one microparticle of 60 μm diameter; b) surface area normalized to mass versus particle diameter; c) gold melting temperature as a function of particle diameter, according to Gibbs-Thomson equation, shown inset; the gold bulk melting temperature is 1336 K [1].

1.1.1 Synthesis methods for nanomaterials

NMs are highly influenced by the synthesis method used, in terms of physicochemical properties and structure. There are two different approaches in making nanoscale materials:

1. Top down: the method consists in reaching nanometric dimensions, starting from a material of larger dimensions. The massive material, "bulk", is split into smaller particles, using mechanical, chemical or other forms of energy.
2. Bottom up: the NM is obtained from the individual atoms, suitably assembled, by chemical reactions, allowing the precursor to increase with the size and the desired characteristics.

In particular, NMs can be synthesized utilizing a variety of methods. Different methods are used in order to optimize specific properties of the materials. These properties include, but are not limited, to size (diameter, length, volume), size distribution, symmetry, surface properties, surface coating, purity, ease of manipulation, yield and suitability for scaling up. The main methods used for the commercial or deliberate manufacture of NMs are:

- *Gas phase processes*, which may be used to produce a wide range of materials. Most (but not all) nanoparticle synthesis methods in the gas phase are based on homogeneous nucleation of a supersaturated vapour or aereosol and subsequent particle growth by condensation, nucleation and capture. The methods can be categorized by the heating or evaporation process used [7]. These include:

    - flame pyrolysis
    - furnace flow reactors
    - laser induced pyrolysis
    - laser vaporisation
    - thermal plasma
    - microwave plasma
    - sputtering
    - laser ablation
    - droplet evaporation

    Gas phase synthesis methods are considered to be able to produce improved specification and control in aspects such as particle size, crystallinity, degree of agglomeration, porosity, chemical homogeneity, purity and stoichiometry [7] and are generally considered to offer good possibilities for scaling up to industrial level processes.
- *Vapour deposition synthesis*. Chemical Vapour Deposition (CVD) methods are based on well established methods for the manufacture of semiconductors [8]. These systems have conventionally been used to deposit thin films of silicon and

other semiconductors on to semiconductor wafers. Vapour is formed in a reaction chamber by pyrolysis, reduction, oxidation and nitridation. Deposited film growth, in several stages beginning with nucleation as the first few atoms, deposit on the surface. These first atoms form islands which spread and coalesce into a continuous film. After this transition film is formed, growth continues until thicker film develops. Areas of growth on the wafer is controlled using various patterning processes (also known as photolithography or photomasking) in which deposition patterns are etched on to the surface layers of the wafers.

- *Colloidal, liquid phase or sol-gel methods* in which chemical reactions in solvents lead to the formation of colloids. Colloidal methods are well established "conventional" wet chemistry precipitation processes in which solutions of the different ions are mixed under controlled conditions of temperature and pressure to form insoluble precipitates. These provide a simple route to the synthesis of NPs.
- *Mechanical processes* including grinding, milling and alloying. In contrast to the previous three groups, where NPs were built "bottom up" from individual molecules, in attrition methods nanoparticles are produced top down from larger particles. Size reduction by grinding and milling is a very well established industrial process used to produce progressively finer forms of materials including minerals such as clay, coal and metals. Production rates of materials can be of the order of tonnes per hour. Production of the finest grades of material was previously referred to as micronizing. Production of particles in the nanometer size range is referred to as ultrafine grinding [9] or nanosizing [10].

1.2 Colloidal nanosuspension (nanosol)

The metal oxide and metal particles with nanometric size have acquired considerable importance in technological innovation, in traditional areas such as ceramics, catalysts, electronics components. Their contribution allows to improve the technology and expand the application fields of these materials. The interest to metal oxide and metal NPs, in scientific and industrial field, derived from their various applications. Indeed

their conductive, magnetic, catalytic, and optical properties make them interesting for numerous sectors: catalytic, electronic, ceramic, biomedical, …etc.

In this regard, colloidal nanosuspension (nanosol) has started to collect success. A colloid is a substance in which dispersed insoluble particles are suspended throughout another substance. The dispersed-phase particles have a diameter of between approximately 1 and 1000 nm. The colloidal particles are typically much larger than molecules of the dispersing medium and have a surface area/volume ratio much higher than the bulk systems, so the surface has significant control on the properties of the colloid itself.

The stability of a colloidal system is defined by particles remaining suspended in solution at equilibrium. Stability is hindered by agglomeration and sedimentation phenomena, which are driven by the colloids tendency to reduce surface energy. The interfacial tension will stabilize the colloidal system by reducing this driving force. Electrostatic stabilization and steric stabilization are the two main mechanisms for stabilization against agglomeration (Fig. 1.4).

- Electrostatic stabilization is based on the mutual repulsion of like electrical charges. In general, different phases have different charge affinities, so that an electrical double layer forms at any interface. Small particle sizes, as NPs, lead to enormous surface areas, and this effect is greatly amplified in colloids. In a stable colloid, mass of a dispersed phase is so low that its buoyancy or kinetic energy is too weak to overcome the electrostatic repulsion between charged layers of the dispersing phase.
- Steric stabilization consists in covering the particles with polymers which prevents the particle to get close in the range of attractive forces.

The nanosols are mainly synthesized by sol-gel methods (wet chemical methods). This approach enables the relatively straightforward production of significant quantities of nanoparticle material at modest capital cost. As with other approaches, much of the recent emphasis has been on the development of more monodisperse particles with better defined shape.

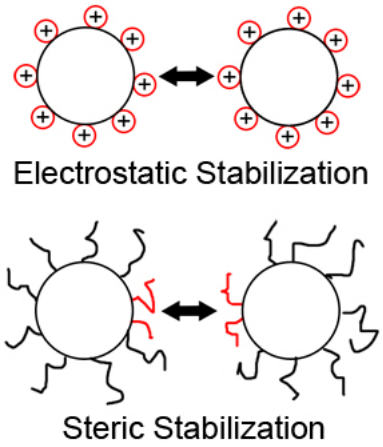

Figure 1.4 Schematic representation of electrostatic and steric stabilization of particles.

The earliest reported colloids were metals. Preparation of metallic colloids dates back several centuries, but scientific investigation of their preparation on properties were first reported by Faraday (1857) in his experiments with gold. Development of colloidal theory, processes and methods have been ongoing since that time. Nanomaterials produced by colloidal process include metals, metal oxides, organics, and pharmaceuticals.

Key papers by Brust et al describe the preparation of high quality nanometre sized gold particles [11,12]. Other nanometer sized metal particles such as silver [13], platinum, iridium and palladium [14,15] have been prepared by analogous routes.

1.2.1 TiO_2 and Silver nanoparticles

Among colloidal nanosupsensions, titanium dioxide and silver based nanosols are the most widely studied, thanks to their applicability in various fields.

Nano-TiO_2 is of all NMs the one with the highest production amount [16]; it has an estimated yearly production of 30000 tonnes in the U.S. [17]. In fact, in recent years, crystalline TiO_2 has received much attention due to their interesting properties as photocatalyst [18-20].

The commercial use of nano-TiO_2 as photocatalyst is becoming in the areas of: water purification [21], air purification [22], sterilization/disinfection [23] and system involving applications of the recently reported superhydrophilic effect [24].

Silver materials have been broadly used since ancient time, in different applications as pigments, photographics, wound treatments, conductive/antistatic composites, catalysts and as biocide [25,26].

Colloidal silver (liquid suspension of silver particles in the size of nanoscale, Ag NPs) has been commercialized for health and medical reasons since the early twentieth century and is now marketed as a dietary supplement and alternative medicine cure-all [27]. Nevertheless, improved capabilities in nanoscience and nanoparticles synthesis and engineering, justify the novel/revived attention on Ag NPs antimicrobial applications, with an estimated amount of about 320 tonnes/year produced and used worldwide [28].

1.3 References

[1] C. Buzea, I. I. Pacheco Blandino, K. Robbie, Biointerphases 2 (2007) MR17–MR172.

[2] K. Seshan, Handbook of Thin-Film Deposition Processes and Techniques, William Andrew Publishing/Noyes, 2007, 1–657.

[3] G. G. Siu, M. J. Stokes, Phys. Rev. B 59 (1999) 3173–3179.

[4] J. Karch, R. Birringer, H. Gleiter, Nature 330 (1987) 556–558.

[5] R. E. Sherriff, R. P. Devaty, Phys. Rev. B 48 (1993) 1525–1536.

[6] E. Roduner, Chem. Soc. Rev. 35 (2006) 583–592.

[7] F.E. Kruis, H. Fissan, A. Peled, J. Aerosol Sci. 29 (1998) 511–535.

[8] V. Zant, Microchip fabrication. A practical guide to semiconductor processing, McGraw Hill Book company, 2000.

[9] S. Mende, F. Stenger, W. Peukert, J. Schwedes, Powder Technol. 132 (2003) 64–73.

[10] E. Merisko-Liversidge, G.G. Liversidge, E.R. Cooper, Eur. J. Pharm. Sci. 18 (2003) 113–120.

[11] M. Brust, M. Walker, D. Bethell, D.J. Schiffrin, R. Whyman, J. Chem. Soc., Chem. Commun. (1994) 801–802.

[12] M. Brust, J. Fink, D. Bethell, D.J. Schiffrin, C. Kiely, J. Chem. Soc., Chem. Commun. (1995) 1655–1656.

[13] S. Murthy, T.P. Bigioni, Z.L. Wang, J.T. Khoury, R.L.Whetten, Mater. Lett. 30 (1997) 321–325.

[14] C. Yee, M. Scotti, A. Ulman, H. White, M. Rafailovich, J. Sokolov, Langmuir 15 (1999) 4314–4316.

[15] C.K. Yee, R. Jordan, A. Ulman, H. White, A. King, M. Rafailovich, J. Sokolov, Langmuir 15 (1999) 3486–3491.

[16] F. Gottschalk, T. Sonderer, R. W. Scholz, B. Nowack, Environ. Toxicol. Chem. 29 (2010) 1036–1048.

[17] C. O. Hendren, X. Mesnard, J. Dröge, M. R. Wiesner, Environ. Sci. Technol. 45 (2011) 2562–2569.

[18] A. Mills, S.K. Lee, J. Photochem. Photobiol. A 152 (2002) 233–247.

[19] A. Fujishima, T.N. Rao, D. Tryk, J. Photochem. Photobiol. C: Photochem. Rev. 1 (2000) 1–21;

[20] M. Langlet, A. Kim, M. Audier, J.-M. Herrmann, J. Sol–Gel Sci. Technol. 25 (2002) 223–234.

[21] T. Oppenlaender, Photochemical Purification of Water and Air, Wiley-VCH, Winheim, Germany, 2003.

[22] M. Kaneko, I. Okura, Photocatalysis Science and Technology, Kodasha-Springer, Tokyo, 2002.

[23] G. Rincon, C. Pulgarin, Appl. Catal. B 49 (2004) 99–112.

[24] R. Wang, K. Hashimoto, A. Fujishima, M. Cjikuni, E. Kojima, A. Kitamura, M. Shimohigoshi, Nature 388 (1997) 431–432.

[25] H. H. Lara, E. N. Garza-Treviño, L. Ixtepan-Turrent, D. K. Singh, J. Nanobiotechnology 9 (2011) 30.

[26] B. Nowack, H. F. Krug, M. Height, Environ. Sci. Technol. 45 (2011) 1177–1183.

[27] N. Seltenrich, Environ. Health Perspect. 121 (2013) A220–A225.

[28] http://www.nanotechproject.org/inventories/silver/.

Chapter 2: NANOMATERIAL APPLICATIONS AND NANOSAFETY

2.1 Nano-TiO_2

Titanium dioxide (TiO_2) exists in nature in three main polymorphs: anatase (tetragonal), rutile (tetragonal) and brookite (orthorhombic). All the polymorphs are formed by TiO_6 octahedra linked to each other in different way (Fig. 2.1).

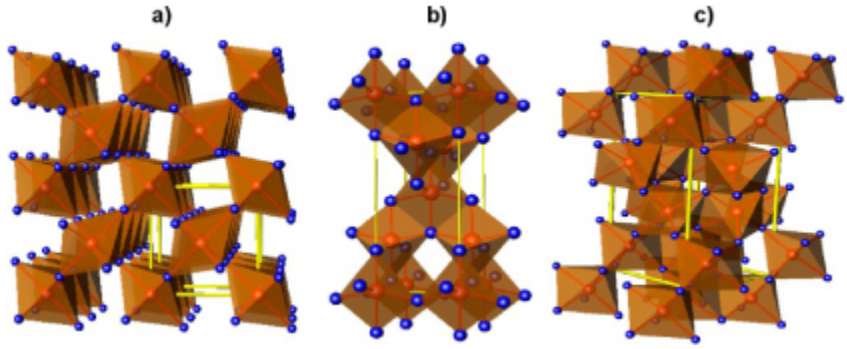

Figure 2.1 Crystal structures of TiO_2 polymorphs. Red spheres are Ti^{4+}, blue spheres are O^{2-} and yellow lines represent the unit cell. (a) Rutile (b) Anatase (c) Brookite [1].

The rutile is the most thermodynamically stable phase whereas anatase and brookite are metastable phases and transform into rutile by thermal treatments.

The chemical and physical properties of the three phases are very different from each other, and moreover they are strictly connected to the synthesis conditions.

The anatase polymorph is prevalently used as photocatalyst, rutile in optical devices whilst the physicochemical properties of brookite are not much known because pure brookite without rutile or anatase is rather difficult to be prepared. However, the anatase form is reported to have the highest photoactivity among the crystalline phases [2].

Nano-TiO_2 is the most used photocatalyst, because of its high nanoscale reactivity, facility of synthesis, stability under various reactions media, cheapness, and bands position compatible with the oxidation of many organic compounds [3].

2.1.1 Photocatalytic process

The catalytic activity of TiO_2 is based on the electron$^-$/hole$^+$ pair formation due to photoexcitation. Nanosized particles show high photoactivity because they have a large surface area per unit mass and volume, and hence facilitate the diffusion of excited electrons and holes towards the surface before their recombination.

In particular, during the photocatalytic process of TiO_2 (Eq. 2.1), two events must simultaneously occur to have a successful production of radicals. First, reduction of an electron acceptor (usually dissolved oxygen) by photoexcited electrons (Eqs. 2.2-2.4); second, dissociative oxidation of adsorbed H_2O by photogenerated holes (Eqs. 2.5-2.7). Both events lead to the formation of highly oxidizing radicals (in particular hydroxyl radicals $^{\bullet}OH$) which are involved in the degradation of adsorbed pollutant molecules [4,5], in fact these radicals are very reactive species that are able to decompose most organic compounds and biological contaminants present in aqueous media [6]. In addition, singlet oxygen ($^1O_2$) is formed through a mechanism which is still under debate [7].

$$TiO_2 + h\nu \rightarrow h_{VB}^{+} + e_{CB}^{-} \quad \text{(Eq. 2.1)}$$

$$O_2 + e_{CB}^{-} \rightarrow O_2^{\bullet -} \quad \text{(Eq. 2.2)}$$

$$O_2^{\bullet -} + e_{CB}^{-} + 2H^{+} \rightarrow H_2O_2 \quad \text{(Eq. 2.3)}$$

$$H_2O_2 + e_{CB}^{-} \rightarrow {}^{\bullet}OH + OH^{-} \quad \text{(Eq. 2.4)}$$

$$H_2O + h_{VB}^{+} \rightarrow {}^{\bullet}OH + H^{+} \quad \text{(Eq. 2.5)}$$

$$^{\bullet}OH + h_{VB}^{+} + H_2O \rightarrow H_2O_2 + H^{+} \quad \text{(Eq. 2.6)}$$

$$H_2O_2 + h_{VB}^{+} \rightarrow O_2^{\bullet -} + 2H^{+} \quad \text{(Eq. 2.7)}$$

The light containing ultraviolet radiation (both natural and artificial) of type A (wavelength ~365 nm) trigger the photocatalytical action that cleanses the surface of TiO_2 from pollutants and microbes. The accepted mechanism for the generation of highly oxidative radicals on the TiO_2 surface when light (below 400 nm) is applied on the photocatalyst surface [8,9] is shown in Figure 2.2.

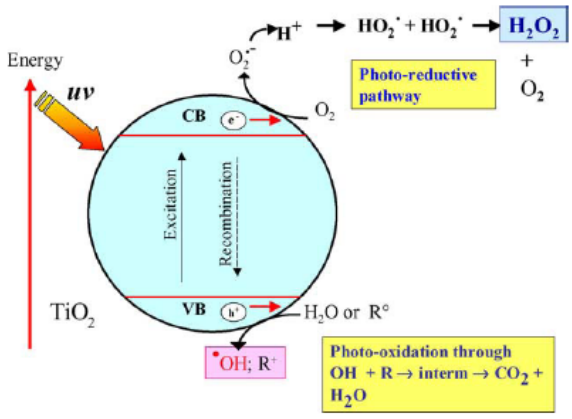

Figure 2.2 Classical scheme for the production of highly oxidative species by TiO_2 under light irradiation with wavelengths <400 nm [10].

2.2 Nano-Ag

Silver has long been know to exhibit a strong toxicity to a wide range of microorganisms [11], for this reason Ag based compounds have been used extensively in many bactericidal applications [12,13].

The bactericidal effect of silver ions on microorganisms is very well known; however, the bactericidal mechanism is only partially understood. It has been proposed that ionic silver strongly interacts with thiol groups of vital enzymes and inactivates them [14,15]. Experimental evidence suggests that DNA loses its replication ability once the bacteria have been treated with silver ions [16]. Thus, silver ions have been demonstrated to be useful and effective in bactericidal applications. Due to not stoichiometric mechanism of Ag^+ ions dissolution at surface level, Ag NPs represent a reasonable alternative for development of new bactericides. Furthermore, metal particles in the nanometer size range exhibit physical properties that are different from both the ion and the bulk material. This allows them to exhibit remarkable properties such as increased catalytic activity due to morphologies with highly active facets [17-22].

2.2.1 Antibacterial mechanism

The mechanisms by which silver nanoparticles (Ag NPs) exert toxicity, and consequently antimicrobial effects, are not fully understood but it is commonly accepted that the released of silver ions (Ag^+) represent the primary mechanism of antibacterial

action, with a particle specific activity negligible [23-25]. As deeply reviewed by Liu et al. [26], the majority of silver ions comes from oxidation of the exposed zerovalent metallic particle, typically by reaction with dissolved O_2 and mediated by protons and other components in the surrounding fluid phase. At the base of the ion-based toxicity pathway, there is a strong interaction with respiratory and transport proteins, due to the high affinity of Ag^+ ions with thiol groups present in the cysteine residues of those proteins [27].

The function of Ag NPs in these processes is both to generate a sustained flux of Ag^+ ions from nano-Ag surfaces and to transport and let available active Ag^+ to sensitive biological targets on cell membranes or within cells, following particle attachment or endocytosis, respectively. Such a role clearly justify many discrepancies already found in literature between “Ag-ion” and “particle-specific” mechanisms. Studies supporting [28-33] a particle specific antibacterial activity, in fact, are based on the resulting lower toxicant reactivity of Ag^+ ions solution in comparison to colloidal silver samples containing an equivalent amount of dissolved Ag^+ ions. Nevertheless, the explanation is not due to different toxicity pathways but to different bioavailabilities of Ag ions to bacterial cells, if they are dissolved or released in the aqueous phase or are transported by Ag NPs surface [34].

In order to definitively overcome confusion arising when solubility of Ag NPs is discussed, and the complicate coexistence of the particle and ionic forms are related to biological reactivity, it is necessary to understand that Ag NPs in their metallic form (noble metal) are totally insoluble and chemically inert. What happens when Ag NPs become in touch with water, in aerobic conditions, is that the surface is oxidized with the creation of a Ag_2O layer with a consequent release of Ag^+ ions [35]. Silver NPs alone can induce toxicity [36]; however a major role is played by the released Ag^+ ions from their surface upon its contact with water (Fig. 2.3). So, a particle specific toxicity is observed and could be explained by the higher bioavailability of Ag^+ ions both adsorbed on Ag NPs surface and released in intracellular environment, by Troyan-horse pathway [37,38].

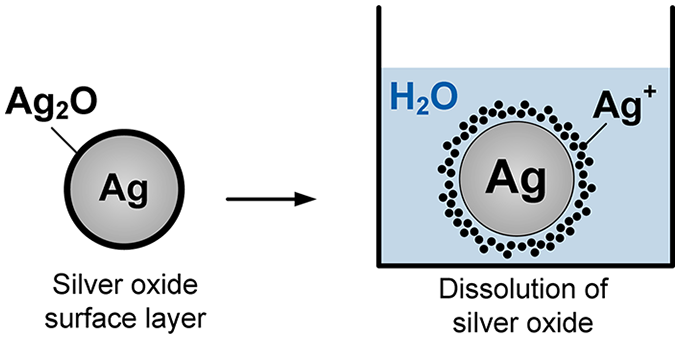

Figure 2.3 Ag^+ ion release from Ag NPS in water [35].

2.2.2 Antibacterial tools for biotechnological application

Silver compounds have also been used in the medical field to treat burns and a variety of infections [16] and are still exploited in medical and biotechnological applications. For example, Lee and Mi report the study about nanocomposite fibers of polyamide 6 (PA6) and hydroxyapatite (HA) that after silver doping show excellent antibacterial activities demonstrating that they can be exploited as functional antibacterial materials in various application fields.

Some papers report examples [13,36], such as inorganic composites with a slow silver release rate that are currently used as preservatives in a variety of products; another current application includes new compounds composed of silica gel microspheres, which contain a silver thiosulfate complex, that are mixed into plastics for long lasting antibacterial protection.

The use of antibacterial nanomaterials is particularly interesting in biotechnological application. An innovative application involves Ag based compounds in the development of methodologies and tools to support the design and management of a processes for the production of biodegradable biopolymers, such as polyhydroxyalkanoates (PHAs), at the expense of a reduction of the PLA and plastics from starch. At this aim, new technologies for isolating PHAs from mixed cultures are developed, combining innovative bacterial pre-treatments and polymer purification strategies by means of Ag nanophases supported on process compatible substrates, as textile and ceramic support. Thus, the study about the design of Ag based nanostructured substrates to be applied into bacteria treatments is needed in order to produce antibacterial tools for biotechnological application. The activity carried out

within Italian project “Probiopol” (Innovative and sustainable production of biopolymers - FdF SP2 – T4.1) demonstrated the possibility to exploit the antibacterial properties of Ag based nanostructured materials in innovative biotechnological applications.

2.3 Nanosafety

The most relevant mechanisms driving the potential impact of nano-TiO_2 are summarized in the followings.

2.3.1 Reactive oxygen species (ROS) production

The presence of nanomaterials (NMs) on to the market as a key to industrial innovation is enhancing, in the recent years. Their great bio-accessibility/availability allows innovative applications in many fields but can also produce negative effects on health of humans and environment exposed to NMs, so justifying a close attention to safety issues. The hazard potential of NMs must be evaluated in order to define biologically effects. The sheer multiplicity of the physicochemical parameters of NM such as size, shape, structure, and elemental constituents makes the investigation of their toxic effects complex and challenging. Some of the paradigms for nanoparticles-mediated toxicity include oxidative stress, inflammation, genetic damage, and the inhibition of cell division and cell death [39-42]. Changes in structural and physicochemical properties of NPs can lead to changes in biological activities including reactive oxygen species (ROS) generation, one of the most frequently reported nanoparticles-associated toxicities. Oxidative stress induced by engineered NPs is due to acellular factors such as particle surface, size, composition, and presence of metals, while cellular responses such as mitochondrial respiration, NPs-cell interaction, and immune cell activation are responsible for ROS-mediated damage. ROS generation (which can be either protective or harmful during biological interactions) and consequent oxidative stress are frequently observed with NP toxicity [43,44]. The physicochemical characterization of NP including particle size, surface charge, and chemical composition is a key indicator for the resulting ROS response and NP-induced injury since many of these NP intrinsic properties can catalyze the ROS production [45].

2.3.2 Oxidative stress

The principal factors for NP-induced oxidative stress involve the oxidative properties of the NPs themselves and oxidant generation upon interaction of NPs with cellular material [46]. Of all the NMs, the metal oxide NPs are more prone to these phenomena, in particular, due to widespread use in industry for several applications ranging from sunscreens, pigments and construction materials to solar cells [47-51] many studies concerning TiO_2 NPs were performed [52,53]. Overall, it is evident that ROS could cause oxidative damage of a range of key structures and components of cells including DNA, proteins and lipids leading to significant functional changes to the cell, cell death, induction of inflammatory pathways or even alterations in terms of cell signaling or communication [54]. For these reason, the measure of oxidative stress and subsequent damage is an important consideration in nanoparticle induced toxicity. Numerous studies have found that oxidative stress is a prominent feature of the cellular response to TiO_2 NPs, including evidence of increased ROS production, depletion of cellular antioxidants, increase in oxidative products or evidence that toxicity is diminished on pretreatment with antioxidant [55]. Moreover, most studies confirm the ability of titania NPs to induce oxidative stress when illuminated with ultraviolet (UV) light [56,57].

2.4 “Safety by design” approach to control and harmonize the biological activity

The number of publications on the topic of NMs has increased at an almost exponential rate since the early 1990s, reaching about 40000 in the year 2005 (Fig. 2.4), as indicated by a search on ISI Web of Knowledge database.

There is also a notable rise in the number of publications discussing their toxicity, particularly in the past five years. The total number of papers on toxicity, however, remains low compared to the total number of publications on nanomaterials, with only around 500 publications in 2005 [58]. The large number of publications on NMs can be explained by the fact that nanoscience and nanotechnology encompass a wide range of fields, including chemistry, physics, materials engineering, biology, medicine, and electronics. However, there are several reviews addressing nanotoxicology aspects. In fact, in the recent years, the interest in the safety of NMs is increasing significantly [59].

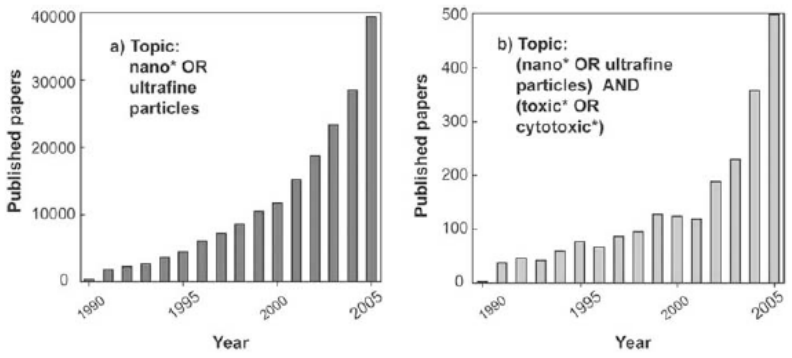

Figure 2.4 Statistics on scientific articles published on a) nanomaterials and b) their toxicity [58].

Owing to increasing knowledge in the nanotechnological development and occupational health and safety issues, there is a new awareness that safety options should also include "smart" nanoparticle design (i.e. "safe by molecular design") to ensure effectiveness of preventive measure [60]. The development of "safety by molecular design" (SbD) risk remediation strategies (RRSs) is a challenging and beyond the state of the art objective aimed to design out risks rather than address them when they occur. These strategies become breakthrough tools to control the risk of occupational exposure to NMs when are integrated within manufacturing processing lines. The main design option that drive the SbD approach is the coating of NMs surface. It is a versatile, practical, cost-effective and easily up-scalable approach, useful to engineer NMs surface and prevent their potential risk. The surface coating is based on mechanisms and kinetics of self-assembled monolayer formation (SAM) [61]. A self-assembled monolayer is an organized layer of amphiphilic molecules in which one end of the molecule, the hydrophilic "head group" shows a specific affinity for a substrate, whilst the hydrophobic "tail group" sticks out on the other side. Self-assembled monolayers on solid surface are formed spontaneously in a solid-liquid dispersion by the adsorption of a surfactant with a specific affinity of its head group to a substrate (Fig. 2.5).

SAMs on NPs including colloids and nanocrystals, stabilize the reactive surface of the particle and present a simple way to control the surface reactivity at the particle-solvent interface. Adsorbate molecules adsorb readily because they lower the surface free-energy of the substrate and are stable due to the strong specific adsorption of the "head groups". These bonds create monolayers that are more stable than the physisorbed

bonds of Langmuir–Blodgett films [62] and still remain bonded to the surface even when the solid substrate is removed from the solution.

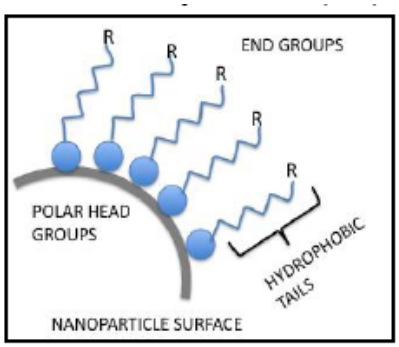

Figure 2.5 Self-assembled monolayer.

The functionalization of colloidal/nano particles by SAM is particularly attractive for the following reasons [63]:

- the ease of preparation
- the tunability of solid/liquid dispersion state
- the tunability of surface properties via modification of adsorbed layer molecular structure and functions
- the use of SAMs as building blocks in more complex structures, e.g., for "grafting" additional layers to a surface
- the possibility of lateral structuring in the nanometer regime
- the large amount of applications made possible by these features.

Due to these features, this method is a powerful design option tool to control the NMs surface reactivity, to improve the manufacturing process of NMs and prevent adverse interaction with biological system. Even though the SAM approach is generally applied to the deposition of organic film to the surface of liquid or solid substrate, self-assembly, defined in a general sense as the spontaneous formation of complex hierarchical structures from pre-designed building blocks, can be extended to inorganic film deposition, typically involving multiple energy scales and multiple degrees of

freedom. In order to select suitable organic and inorganic coating, it is advisable to consider the following several criteria:

- established biocompatibility
- availability of toxicity data that encourages their use in nanomedicine
- low cost
- widespread use in colloidal processes.

From the analysis of literature data describing the interactions at the NP-biological interface [64,65], it is clear that the nano-bio interface is not in a steady state. It undergoes continuous changes as a result of NPs interacting with proteins, membranes, cells, DNA and organelles, depending on colloidal forces as well as on specific bio-physicochemical interactions. Coating of NPs with protective shells (for example biocompatible polymers or inorganic SiO_2) is an effective means of preventing the dissolution and release of toxic ions while also providing a physical barrier against biologically nonspecific events. The prevention of biologically nonspecific events, in fact, such as binding with complement protein C3b, immunoglobulins G and M, fibronectin and apolipoproteins in the process of opsonisation or direct interaction with cells of the reticuloendothelial system (RES), seems to be a key goal to decrease adverse biological responses such as acute toxicity or accumulation in the RES organs. So, the application of surface coating, controlling the nano-bio interactions, is an efficient method to prevent non-specific biomolecules adsorption events and hinder the direct interaction with cellular membrane. Furthermore, the presence of surface coating can directly influence the emission potential. The increased dispersability in aqueous media, in fact, reduce the potential of aerosolization and decrease the probability of exposure through inhalation point of entry. On the basis of these concepts, it is possible to control and harmonize the biological activity of TiO_2 NPs, developing RRSs based on SbD approach [66]. NPs surface functionalization with organic or inorganic is expected to influence mechanisms driving NPs-cell chemical interactions and exposure routes. Nevertheless, the surface engineering must be carried out, by preserving the functional properties of NMs.

2.5 References

[1] V.C. Fuertes , C.F.A. Negre, M.B. Oviedo, F.P. Bonafé, F.Y. Oliva, C.G. Sánchez, J. Phys. Condens. Matter 25 (2013) 115304.

[2] A. Kato, H. Tsuzuki, Y. Taoda, T. Torii, Y. Kato, J. Butsugan, Mater. Sci. 29 (1994) 5911–5915.

[3] R.I. Bickley, T. González-Carreno, J.S. Lees, L. Palmisano, R.J.D. Tilley, J. Solid State Chem. 92 (1991) 178–190.

[4] A. Fujishima, X. Zhang, D.A. Tryk, Surf. Sci. Rep. 63 (2008) 515–582.

[5] M. Zhang, L. Shi, S. Yuan, Y. Zhao, J. Fang, J. Colloid Interface Sci. 330 (2009) 113–118.

[6] T. Yuranova, D. Laub, J. Kiwi, Catal. Today 122 (2007) 109–117.

[7] T. Daimon, T. Hirakawa, M. Kitazawa, J. Suetake, Y. Nosaka, Appl. Catal. A 340 (2008) 169–175.

[8] A. Nozik, Photo-Effects at the Semiconductor-Electrolyte Interfaces, ACS Symposium Series 146, Am. Chem. Soc., Washington, DC, 1981.

[9] S.Roy Morrison, Electrochemistry at Semiconductor and Oxidized Metal Electrodes, Plenum Press, New York, 1982.

[10] A. Bozzi, T. Yuranova, I. Guasaquillo, D. Laub, J. Kiwi, J. Photochem. Photobiol. A: Chem. 174 (2005) 156–164.

[11] S.Y. Liau, D.C. Read, W.J. Pugh, J.R. Furr, A.D. Russell, Lett. Appl. Microbiol. 25 (1997) 279–283.

[12] K. Nomiya, A. Yoshizawa, K. Tsukagoshi, N. Chikaraishi Kasuga, S. Hirakawa, J. Watanabe, J. Inorg. Biochem. 98 (2004) 46–60.

[13] A. Gupta, S. Silver, Nat. Biotechnol. 16 (1998) 888.

[14] Y. Matsumura, K. Yoshikata, S. Kunisaki, T. Tsuchido, Appl. Environ. Microbiol. 69 (2003) 4278–4281.

[15] L. Nover, K.D. Scharf, D. Neumann, Mol. Cell. Biol. 3 (1983) 1648–1655.

[16] Q.L. Feng, J. Wu, G.Q. Chen, F.Z. Cui, T.N. Kim, J.O. Kim, J. Biomed. Mater. Res. 52 (2000) 662–668.

[17] S. Iijima, T. Ichihashi, Phys. Rev. Lett. 56 (1986) 616–619.

[18] P.M. Ajayan, L.D. Marks, Phys. Rev. Lett. 60 (1988) 585–587.

[19] N. Doraiswamy, L.D. Marks, Surf. Sci. 348 (1996) 67–69.

[20] M. Haruta, Catal. Today 36 (1997) 115–123.

[21] M.J. Yacaman, J. J. Velázquez-Salazar, M. Jose-Yacaman, J. Vac. Sci. Technol. B 19 (2001) 1091–1103.

[22] G. Somorjai Nature 430 (2004) 730.

[23] Z. Xiu, Q. Zhang, H.L. Puppala, V.L. Colvin, P.J.J. Alvarez, Nano Lett. 12 (2012) 4271–4275.

[24] R. Ma, C. Levard, S.M. Marinakos, Y. Cheng, J. Liu, F.M. Michel, G.E. Brown, G.V. Lowry, Environ. Sci. Technol. 46 (2012) 752–759.

[25] A. Ivask, A. ElBadawy, C. Kaweeteerawat, D. Boren, H. Fischer, Z. Ji, C. Hyun Chang, R. Liu, T. Tolaymat, D. Telesca, J.I. Zink, Y. Cohen, P.A. Holden, H.A. Godwin, ACS Nano 8 (2014) 374–386.

[26] J. Liu, D.A. Sonshine, S. Shervani, R.H. Hurt, ACS Nano 4 (2010) 6903–6913.

[27] C. Marambio-Jones, E.M.V. Hoek, J. Nanopart. Res. 12 (2010) 1531–1551.

[28] C.N. Lok, C.M. Ho, R. Chen, Q.Y. He, W.Y. Yu, H. Sun, P. K.H. Tam, J.F. Chiu, C. Che, J. Proteome Res. 5 (2006) 916–924.

[29] S. Pal, Y.K. Tak, J.M. Song, Appl. Environ. Microbiol. 73 (2007) 1712–1720.

[30] C. Gunawan, W. Teoh, C. Marquis, J. Lifia, R. Amal, Small 5 (2009) 341–344.

[31] X. Jin, M. Li, J. Wang, C. Marambio-Jones, F. Peng, X. Huang, R. Damoiseaux, E.M.V. Hoek, Environ. Sci. Technol. 44 (2010) 7321–7328

[32] J.S. McQuillan, G.H. Infante, E. Stokes, A.M. Shaw, Nanotoxicology 6 (2012) 857–866.

[33] A. Ivask, S. George, O. Bondarenko, A. Kahru, Metal-containing nanoantimicrobials: differentiating the impact of solubilized metals and particles. Nano-antimicrobials- Progress and Prospects, Springer, 2012, 253–290.

[34] O. Bondarenko, A. Ivask, A. Käkinen, I. Kurvet, A. Kahru, PLoS ONE 8 (2013) e64060.

[35] A.G. Sotiriou, A. Meyer, J.T.N. Knijnenburg, S. Panke, S.E. Pratsinis, Langmuir 28 (2012) 15929−15936.

[36] J.R. Morones, J.L. Elechiguerra, A. Camacho, K. Holt, J.B. Kouri, J.T. Ramírez, M.J. Yacaman, Nanotechnology 16 (2005) 2346–2353.

[37] S.N. Luoma, Silver nanotechnologies and the environment: old problems or new challenges?, The Pew Charitable Trusts, 2008.
[38] E.-J. Park, J. Yi, Y. Kim, K. Choi, K. Park, Toxicol. in Vitro 24 (2010) 872–878.
[39] V. Stone, H. Johnston, M. J. D. Clift, IEEE Trans. Nanobiosci. 6 (2007) 331–340.
[40] Y. Ju-Nam, J. R. Lead, Sci. Total Environ. 400 (2008) 396–414.
[41] N. Li, T. Xia, A. E. Nel, Free Radical Bio. Med. 44 (2008) 1689–1699.
[42] H. J. Johnston, G. Hutchison, F. M. Christensen, S. Peters, S. Hankin, V. Stone, Crit. Rev. Toxicol. 40 (2010) 328–346.
[43] N. Li, M. Hao, R.F. Phalen, W.C. Hinds, A.E. Nel, Clin. Immunol. 109 (2003) 250–265.
[44] A. Nel, T. Xia, L. Madler, N. Li, Science 311 (2006) 622–627.
[45] A. A. Shvedova, A. Pietroiusti, B. Fadeel, V. E. Kagan, Toxicol. Appl. Pharm. 261 (2012) 121–133.
[46] A. Manke, L. Wang, Y.Rojanasakul, BioMed Res. Int. 2013 (2013) 942916.
[47] X. Chen, S.S. Mao, Chem. Rev. 107 (2007) 2891−2959.
[48] R. Kaegi, A. Ulrich, B. Sinnet, R. Vonbank, A. Wichser, S. Zuleeg, H. Simmler, S. Brunner, H. Vonmont, M. Burkhardt, M. Boller, Environ. Pollut. 156 (2008) 233−239.
[49] G. Li, S. Ciston, Z.V. Saponjic, L. Chen, N. M. Dimitrijevic, T. Rajh, K.A. Gray, J. Catal. 253 (2008) 105−110.
[50] J. Lee, S. Mahendra, P.J.J. Alvarez, ACS Nano 4 (2010) 3580−3590.
[51] N. Sadrieh, A. M. Wokovich, N.V. Gopee, J.W. Zheng, D. Haines, D. Parmiter, P.H. Siitonen, C.R. Cozart, A.K. Patri, S.E. McNeil, P.C. Howard, W.H. Doub, L.F. Buhse, Toxicol. Sci. 115 (2010) 156−166.
[52] L.D. Sanchez, S.F.M. Taxt-Lamolle, E.O. Hole, A. Krivokapic, E. Sagstuen, H.J. Haugen, Appl. Catal. B Environ. 142–143 (2013) 662–667.
[53] Z. Barbieriková, M. Mihalíková,V. Brezová, Photochem. Photobiol. 88 (2012) 1442–1454.
[54] M. Valko, D. Leibfritz, J. Moncola, M. T.D. Cronin, M. Mazura, J. Telser, Int. J. Biochem. Cell B. 39 (2007) 44–84.
[55] L. Reijnders, Polym. Degrad. Stabil. 94 (2009) 873–876.

[56] S. George, H. Gardner, E.K. Seng, H.Chang, C.Y. Wang, C.H.Y. Fang, M. Richards, S. Valiyayeettil, W.K. Chan, Environ. Sci. Technol. 48 (2014) 6374−6382.

[57] G. Janer, E. Mas del Molino, E. Fernández-Rosas, A. Fernández, S. Vázquez-Campos, Toxicol. Lett 228 (2014) 103–110.

[58] C. Buzea, I. I. Pacheco Blandino, K. Robbie, Biointerphases 2 (2007) MR17–MR172.

[59] RJ Aitken, KS Creely, CL Tran, Nanoparticles: An occupational hygiene review, HSE BOOKS, 1999.

[60] G. Morose, J. Clean. Prod. 18 (2010) 285–289.

[61] D.K. Schwartz, Annu. Rev. Phys. Chem. 52 (2001) 107–137.

[62] A. Kaifer, Supramolecular Electrochemistry. Coral Gables. Wiley VCH. 2001, 191–193.

[63] F. Schreiber, Prog. Surf. Sci. 65 (2000) 151–257.

[64] A.E. Nel, L. Mädler, D. Velegol, T. Xia, E.M.V. Hoek, P. Somasundaran, F. Klaessig, V. Castranova, M. Thompson, Nature Materials 8 (2009) 543–557.

[65] L. Yan, F. Zhao, S. Li, Z. Hu, Y. Zhao, Nanoscale 3 (2011) 362–382.

[66] D. Gardini, M. Blosi, C. Delpivo, S. Ortelli, A.L. Costa, J. Phys. Conf. Ser. 429 (2013) 012052.

Chapter 3: NANOSTRUCTURED MATERIALS AND SURFACE FUNCTIONALIZATION

3.1 Nanostructured material

The nanostructured materials are materials with phase heterogeneities, “buildings blocks”, in the range of nanometric dimensions (typically from 1 to 100 nm and not longer than 500 nm), in at least one direction. These constituents are generally crystallites, but can also be amorphous (as polymers) differing in atomic structure, crystallographic orientation and chemical composition. The nanostructured materials consisting of nanometer-sized blocks and interfaces can be classified according to their chemical composition and shape of their nanostructural constituents (Fig. 3.1) [1].

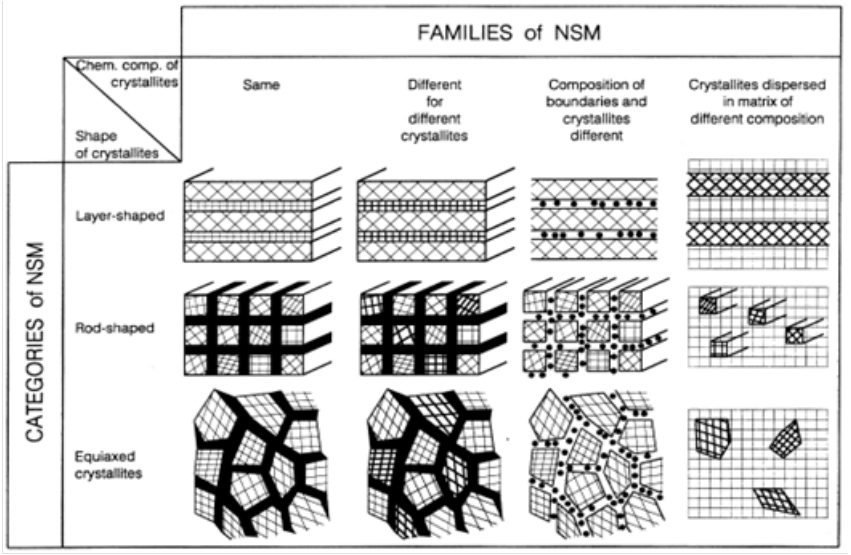

Figure 3.1 Classification scheme for nanostructured materials according to the chemical composition and shape of their structural elements (crystallites) [1].

3.2 Nanocomposite

Nanocomposite is a multiphase solid material where one of the phases has one, two or three dimensions of less than 100 nanometers, or structures having nanoscale repeat distances between the different phases that make up the material. In the broadest sense

this definition can include porous media, colloids, gels and copolymers, but is more usually taken to mean the solid combination of a bulk matrix and nanodimensional phases differing in properties due to dissimilarities in structure and chemistry.
Nanocomposites are divided in three main groups:

- *Ceramic-matrix nanocomposites*. In this group of composites the main part of the volume is occupied by a ceramic. In most cases, ceramic-matrix nanocomposites encompass a metal as the second component. Ideally both components, the metallic one and the ceramic one, are finely dispersed in each other in order to elicit the particular nanoscopic properties. Nanocomposite from these combinations were demonstrated in improving their optical, electrical and magnetic properties [3] as well as tribological, corrosion-resistance and other protective properties [4]. The concept of ceramic-matrix nanocomposites was also applied to thin films that are solid layers of a few nm to some tens of µm thickness deposited upon an underlying substrate and that play an important role in the functionalization of technical surfaces. Gas flow sputtering by the hollow cathode technique turned out as a rather effective technique for the preparation of nanocomposite layers. The process operates as a vacuum based deposition technique and is associated with high deposition rates up to some µm/s and the growth of nanoparticles in the gas phase. Nanocomposite layers in the ceramics range of composition were prepared from TiO_2 and Cu by the hollow cathode technique [5] that showed a high mechanical hardness, small coefficients of friction and a high resistance to corrosion.
- *Metal-matrix nanocomposites*. Metal matrix nanocomposites (MMC) can also be defined as reinforced metal matrix composites. This type of composites can be classified as continuous and non-continuous reinforced materials. One of the more important nanocomposites is carbon nanotube metal matrix composites, which is an emerging new material that is being developed to take advantage of the high tensile strength and electrical conductivity of carbon nanotube (CNT) materials. Critical to the realization of CNT-MMC possessing optimal properties in these areas are the development of synthetic techniques that are (a)

economically producible, (b) provide for a homogeneous dispersion of nanotubes in the metallic matrix, and (c) lead to strong interfacial adhesion between the metallic matrix and the carbon nanotubes. In addition to carbon nanotube metal matrix composites, boron nitride reinforced metal matrix composites and carbon nitride metal matrix composites are the new research areas on metal matrix nanocomposites [6].

- *Polymer-matrix nanocomposites*. In the simplest case, appropriately adding nanoparticles to a polymer matrix can enhance its performance, often dramatically, by simply capitalizing on the nature and properties of the nanoscale filler (these materials are better described by the term "nanofilled polymer composites" [7]). This strategy is particularly effective in yielding high performance composites, when good dispersion of the filler is achieved and the properties of the nanoscale filler are substantially different or better than those of the matrix. NPs such as graphene, carbon nanotubes, molybdenum disulfide and tungsten disulfide are being used as reinforcing agents to fabricate mechanically strong biodegradable polymeric nanocomposites for bone tissue engineering applications. The addition of these nanoparticles in the polymer matrix at low concentrations (~0.2 weight %) leads significant improvements in the compressive and flexural mechanical properties of polymeric nanocomposites [8,9]. Potentially, these nanocomposites may be used as a novel, mechanically strong, light weight composite as bone implants. The results suggest that mechanical reinforcement is dependent on the nanostructure morphology, defects, dispersion of nanomaterials in the polymer matrix, and the cross-linking density of the polymer. In general, two-dimensional nanostructures can reinforce the polymer better than one-dimensional nanostructures, and inorganic nanomaterials are better reinforcing agents than carbon based nanomaterials. In addition to mechanical properties, multi-walled carbon nanotubes based polymer nanocomposites have also been used for the enhancement of the electrical conductivity [10]. In this regards, the incorporation of inorganic nanomaterials as fillers within a polymeric matrix has expanded opportunities to produce a multifunctional nanocomposite membrane

that is capable of performing tasks beyond separation alone [11]. So, the morphology of the added inorganic nanomaterials determines the size of the interphase between the fillers and polymer chains and then stabilizes the nanocomposite membrane by a possible molecular-level synergic effect between the organic and inorganic constituents. A key parameter for the successful implementation of nanocomposite membrane is to increase the dispersion of the inorganic nanofiller in polymer matrix through the establishment of specific interaction between the two phases [12]. In nanocomposite membrane field, the use of nanofibers coupled to NP embedding (seen Section 3.4.3.3) represents an innovative strategy to produce multifunctional membrane with high efficiency.

3.3 Nanostructured coating

With the rapid development of nanotechnology, nanostructured materials in various forms are finding wider applications than before because of their specifically size-related properties. For example, the energy band structure becomes discrete for nanometer-scale TiO_2, and its photophysical, photochemical, and surface properties are quite different from those of the bulk ones due to the quantum size effect, and therefore, many works have focused on the synthesis of nanocrystalline TiO_2 with a large specific surface area [2], which are integrated in photocatalytic devices.

In particular, recently, nanocoated materials are widely studied, in fact the application of nanostructured coatings allows to create new materials, in which the properties of NPs, that constitute the coating, are transferred to the surface.

Nanotechnology applications in coatings have shown remarkable growth in recent years. This is a result of two main factors:

1) increased availability of nanoscale materials such as various types of NPs
2) advancements in processes that can control coating structure at the nanoscale.

Nanocoatings are opening new market opportunities in the global surface coatings scenario, offering new applications in various sectors. In particular, new approaches

have been used to design, create or model nanocoating systems, opening new prospective in the food, health and biomedical industry.
The potential use of novel nanosurfaces and more reliable nanomaterials by employing nanostructured thin films and nanocomposites have been fruitfully exploited in relevant industrial application:

- food packaging
- security pharmaceutical labels
- novel polymeric containers for food contact
- medical surface instruments
- bio-implants/bio-inspired materials
- metal and ceramic industrial devices.

Nanostructured materials and coatings offer the potential for significant improvements in engineering properties based on improvements in physical and mechanical properties resulting from reducing microstructural features by factors of 100 to 1000 times compared to current engineering materials. For example, the potential benefits include higher hardness and strength in metals and cermets resulting from reduced grain size and slip distance, respectively. In ceramics, higher hardness and toughness may be accomplished with reduced defect size and enhanced grain boundary stress relaxation, even at ambient temperature. Diffusivity is greatly increased, associated with a larger volume of grain boundaries. Thermal conductivity may be reduced because of enhanced phonon scattering from grain boundaries and other nanoscale features.

3.4 Surface functionalization

The functionalization of substrates through the application of nanostructured coatings allows to create new materials, with enhanced functional properties.
The functionalization of surfaces may be exploited for many applications: barrier coatings [13], self-cleaning hydrophobic [14] or photocatalytic coatings [15,16], antistatic coatings [17,18], superparamagnetic coatings [19] with consequently very

important technological feedback. The type of support, the nature of the coating and the way to interact affect the final properties of material.

3.4.1 Textile support

In recent years, the textile industry has increasingly focused its interest on nanotechnologies.

The functionalization of textile is expected to allow the textiles high-grade functions by adding value to a specific attribute or function or effect. The main source of inspiration for advances in textile material innovation is rapid development and commercialization of surface modification and nanotechnology in many other fields.

Review papers recently published strengthen the awareness that the introduction of nanotechnologies in a traditional sector like textiles has the chance to carry out an actual technological revolution [20-22].

The use of nanometric particles increases the degree of adhesion of a given treatment and its functionality. Furthermore, the tiny particle sizes render them transparent to visible light and therefore their presence does not alter colors, “hand” and “breathability” of fabrics [23]. NPs of metal oxides have a particular affinity for the natural hydrophilic fibers and may be used in the finishing processes of fabrics to modify their surface properties and impart new functions to the product [24]. For example, Shi and Liu et al. [25] prepared water repellent coating (hydrophobic coating) on cotton textile from fluorinated diblock copolymers. Xu et al. [26] deposited nanoscale TiO_2 films on the surface of polyester (PET) nonwovens by using reactive magnetron sputtering in order to obtain antistatic materials. Chattopadhyay and Patel [27] reported the fabrication of nano-Zinc coated cotton textile with antimicrobial properties. Bozzi and Kiwi et al. [28] demonstrated photodiscoloration and mineralization of stains of red wine and coffee on nano-TiO_2 coated textile with self-cleaning properties. In fact because of their excellent photocatalytic properties, nanostructured TiO_2 anatase based coatings are widely exploited in process of stains removal from textile, under UV irradiation [29,30].

3.4.2 Functionalization methods on textile support

The functionalization of textile support can be performed following two main processes:

1) *Functional finishing technology* allows to obtain high performance textiles by adding value to a specific attribute or function or effect [31], on a textile product previously weaved. The well known textile functional finishing, in particular, has a vital role in modifying the appearance, texture, handle and performance of all kinds of fabrics to be suitable for the end-use. Therefore, the functional finishing approach is particularly appreciated by textile industry since it involves surface modification technique which can be done at the very last stages of material production. Functional finishing technology enable producers to continue to use traditional textile fibres and at the same time to achieve added-value that captures the potential consumer markets. Surface structure and the behaviour of textile fibres are of utmost importance for the properties of textile materials in processing and exploitation [32].

   By using appropriate surface modification technology on traditional textile materials, new functionalities can be easily implemented and new added-value textile materials can be created to provide consumers with greater levels of comfort, safety, aesthetics and functional performance.

   The main advantage of modifying a very thin surface layer (as nanocoating) of the material is that the positive values of the textile material such as mechanical strength, flexibility and wear resistance are maintained. Generally, surface modification technologies for textilefunctional finishing can be divided into two categories: physically based technology and chemically based technology. However, many times the exact classification it is difficult as modifying effects usually come from both physical and chemical reactions. The nature of physical functional finishing is non-contact and non-aqueous treatment. Recently, the numbers of developments in physically based technology, which can harmonize the environment and production, have increased because regulations on chemical substances have become stricter. Some examples of physically based technologies that currently attract high attention are: low-temperature plasma,

ozone treatment, UV irradiation and laser irradiation. The examples of chemically based technologies are: surface activation by incorporation of reactive groups, surface coating by grafting of organic substances, surface coating by incorporation of inorganic substances and sol-gel condensation. At present chemically based technologies are still major, but their combination with physically based technologies is steadily increasing. In recent years, the surface modification approach has been dominated by application of nanostructured coating.

2) *Spinning technology with the functionality embedding.* In this case, the production of textile and functionality occur in the same time. This approach allows to develop functional fibers, incorporating the active phase (functionality) into the fibers in its manufacturing stage. This technology is rather increasing today, mainly being supported by fiber manufactures. The desired characteristics of textile are achieved as a combination of fiber properties and set-up of the spinning process. The classical spinning technologies are: ring spinning, compact spinning, rotor spinning technology (OE spinning = open end spinning) and friction spinning. The choice of spinning technology determines the strength and hard (harshness and softness) of the final fabric [33]. A novel method, belonging to spinning technology, is the electrospinning (described in detail in Section 3.4.2.2). This technique allows to produce fibers with nanometric diameters and is able to an easy functional embedding.

Technical requirements to be satisfied at the development stage of new performance textile (Fig. 3.2) influence process an finishing technologies, strengthening the important role that nanotechnology has in the field.

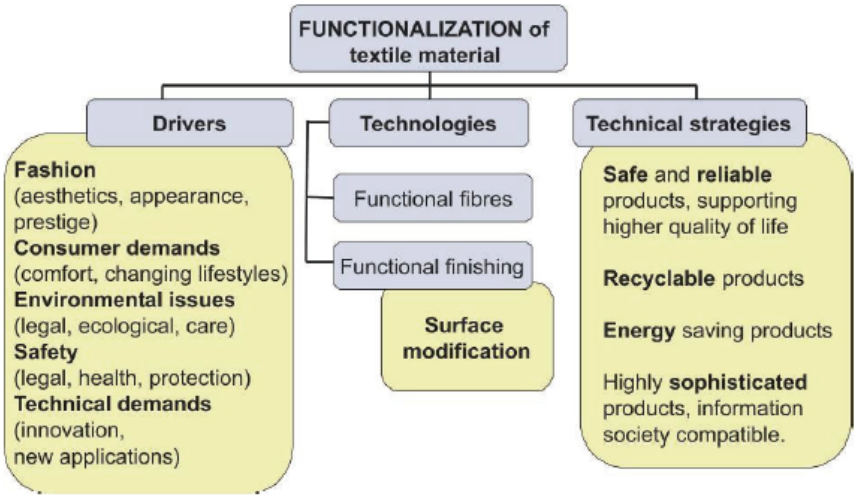

Figure 3.2 Available technologies for obtaining functionalized textile material [31].

3.4.2.1 Finishing through dip-padding-curing method

A very important challenge in the application of nanotechnologies to textile is resolving the problem of binding NPs to the fabric. The central problem is to assure tight binding of NPs to the surface of textiles in order to increase the durability of the desired properties. This also ensures that nanoparticles are not released in the environment, fulfilling also the ecological requirements [34]. Furthermore, the films applied on textile must be colourless and optically transparent, so that there is no disturbance of the original colour of the fabric, and finally, the mechanical properties must remain intact.

Among finishing technologies, the dip-padding-curing method is the most promising, due to its cost, simplicity, and easy industrial scale-up [35,36]. It consists to dip the fabric in the nanosol, for a given time, and then passing through a padding mangle (squeezing), to remove excess solution; finally, the fabric is dried and cured in oven. The dip-padding-curing process has been already proposed to create bonds between TiO_2 and fabrics.

For example, Qi et. al. [37] examined the colorant decomposition activities of TiO_2-treated cotton fabric by the dip-padding-curing process, before and after 10 and 20 washings. The obtained results showed that after 20 washings, self-cleaning properties were not significantly impaired in comparison to the situation after 10 washings, which may be due to the creation of strong bonds between the titanium layer and the surface of

cotton which is the result of dehydration reaction of the hydroxyl groups of cellulose and titanium [38,39]. This demonstrates the good affinity between TiO_2 and cotton based fabrics and confirms the dip-padding-curing as excellent method to functionalize textile with NPs.

3.4.2.2 Electrospinning

An innovative method to produce fibers is the electrospinning process, used, in particular, for the synthesis of nanofibers [40].

Electrospinning is a cheap and relatively simple technique of producing nanofibers. Electrospinning is an electro-hydrodynamic process that is widely considered the most promising and versatile platform technology for the production of nanofibrous materials.

The process takes place between a spinning head with a capillary opening, where a high voltage is applied and a static (usually grounded) plate acting as a nanofiber collecting counter-electrode. The spinning head is connected with a reservoir of polymer solution under pressure. The high voltage difference between the spinning head and the ground results in a nano- to micron-sized electrically-driven polymer solution jet which is drawn out from the apex of a cone (so-called Taylor cone) formed at the capillary opening of the spinning head. The solvent rapidly evaporates from the jet during the travel and, under optimal conditions, a continuous nanosized filament is deposited to the collecting electrode in a random fashion forming a non-woven structure.

The Figure 3.3 shows the electrospinning process for a basic system. Electrospun nanofibers are unique compared to other conventional materials due to their high surface to volume ratio, high fiber interconnectivity and nanoscale interstitial spaces. Nanofibers with further functional desired properties can be obtained by adding nanoparticles, as functionalities, into a polymer solution (feed solution).

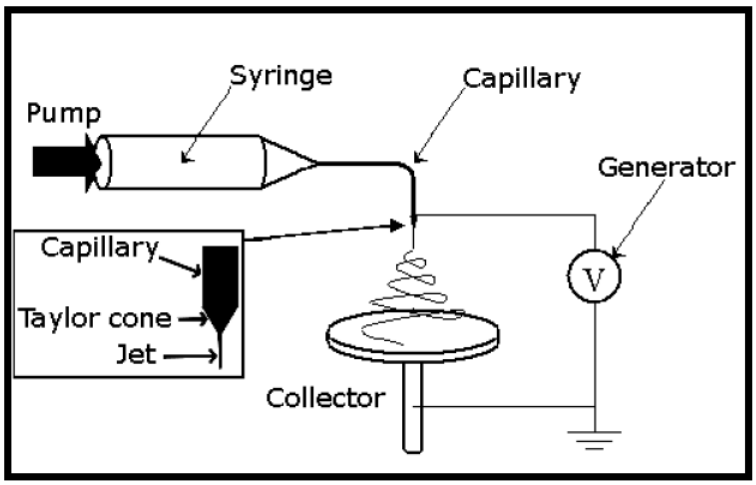

Figure 3.3 Schematic illustration of the basic set-up for electrospinning.

3.4.3 Functionalized textile applications

3.4.3.1 Self-cleaning textile

Recently, the application of nano-TiO_2 in textile finishing has become an important area of research because of the self-cleaning effect provided by nano-TiO_2 coatings to textile substrates. The application of TiO_2 to textile, in fact, may result in efficient levels of self-cleaning activity, with the actual capability to degrade stains, bacteria, volatile organic compounds (VOCS) adsorbed onto fibers and transform them into CO_2 and H_2O.

The photocatalytic activity of TiO_2 is induced by UV light excitation, with consequent formation of electron$^-$/hole$^+$ pairs. The released electrons are able to react with water and oxygen molecules on the surface to form free radicals. These radicals are very reactive species that are able to decompose most organic stains as well as biological contaminants present in aqueous media (seen Section 2.1.1). Interphase domain plays a crucial role in governing the photocatalytic activity of TiO_2 coated materials, and macroscopic properties, such as surface hydrophilicity, affect directly the photocatalytic performances [41-43]. The common effort of nanomaterial scientist community towards the development of new materials by design and engineering at nanoscale level, requires an increasing knowledge of structure-reactivity relationships, in order to get the wished control on final properties. As demonstrated by numerous papers [44-46] coatings based on TiO_2 have attracted a particular attention due to their photocatalytic properties,

exploitable in processes of stain removal [47,48] as well as for antibacterial [49-51] and deNOx activity [52,53]. In this scenario, titanium oxide is playing the main role, compared to other semiconductor photocatalysts, due to its cost effectiveness, inert nature and photostability.

Supported TiO_2 films, on different substrates, can be prepared by many methods, such as anodic oxidation [54-57], sputtering [58,59] and sol‑gel process [28,60-65], nevertheless sol-gel deriving processes such as dip- or spray-coating are the most widely employed. The cited sol-gel methods describe the preparation of TiO_2 nanosol by sol-gel synthesis from precursors or by colloidal dispersion from commercial powder. Both these procedures present some disadvantages in a view of a large scale application. In particular, the first suffers from the complexity and low reproducibility of wet chemicals processes and the second from problems related to the stability and the degree of transparency of the nanopowder dispersion. The used of dip-padding-curing method (seen Section 3.4.2.1) starting from commercial stableTiO_2 nanosols overcomes these problems producing self-cleaning photocatalytic textile with stabilized characteristics and a guaranteed reproducibility.

3.4.3.2 Antibacterial textile

Currently, one of the most popular functionalization is the development of antibacterial materials. In this field, the very important issues are maintaining the resistance of these antibacterial coating to washing, drying, and dry-cleaning operations, no toxicity to humans and to the environment, easy application without any loss of function, and low cost of textile production. Recently, there was observed a significant increase in use of silver compounds into the antibacterial finishing of the textile products, especially concerning the application of the nanosilver particles. The impact of nanotechnology in the textile industry made it possible to produce a new generation of the antibacterial textiles by innovative functionality on fabric surface. The role of Ag as an effective antimicrobial agent is well-known. In general, it can inhibit the growth of a wide variety of micro-organisms including fungi, viruses, and bacteria (seen Section 2.2). Nano-Ag is very reactive with proteins, and when it comes into a contact with the bacteria or fungi it inhibits cell growth, due to the fact that Ag affects a cellular metabolism. It also

suppresses respiration, the basal metabolism of the electron transfer system, and the transport of the substrate into the microbial cell membrane. Furthermore, it inhibits the multiplication and growth of those bacteria and fungi, which can cause infection [66]. Nowadays, the use of Ag NPs is the most popular method to produce antibacterial fabrics, as many papers demonstrate [67-70]. The promising potential of silver was promptly recognized by textile industry. Silver in both ionic and colloidal form ensures excellent antimicrobial activity. However, ionic silver based textile materials when exposed to light turns the color of the material to black–brown [71], and present well known safety problems, due to the high ions leaching. These disadvantages can be avoided by the application of silver nanoparticles (Ag NPs). Despite the use of antibacterial chemicals in solution, it seems that the functionalization with Ag NPs not only improves antimicrobial durability but also does not significantly alter the fabric breathability and handle [72].

Small size i.e., high surface to volume ratio of Ag NPs makes them very reactive. In other words, considerable amount of silver atoms on the surface of the NPs is exposed toward surrounding medium, providing an extraordinary bactericidal efficiency. Furthermore, small amount of Ag NPs ensures high antimicrobial efficiency. The loading of textile materials with Ag NPs is performed in two different ways: Ag NPs can be embedded into synthetic fibers during the spinning process or they can be deposited on textiles in different forms (fibers, yarns, and fabrics) during finishing. Classical dip-coating method, as dip-padding-curing process, is the most frequently applied where the fabrics are immersed in colloidal suspension of Ag NPs. However, the studies on in situ silver ion reduction and formation of Ag NPs on the fibers are also reported [73,74].

3.4.3.3 Multifunctional filter media based on nanofibers

Recent advances in comprehension of the electrospinning process have greatly contributed to the development of functional nanofibers. The variety of polymer-based materials used in electrospinning is growing and now includes biopolymers and nanocomposites.

Electrospun nanofibers have generated increasing interest in the field of materials science in last two decades and have been proposed for several value-added applications such as filtration, personal protective equipment, barrier, bio-medical, personal care, wipes, garments, acoustic and thermal insulation, sensors and energy storage [75-78]. The electrospinning process is considered one of the most versatile and effective method for the production of continuous nanofibrous media from a huge range of materials: polymers, ceramics, composites. Electrospun nanofibrous materials are physically versatile, but different chemical functionalities may be introduced through the use of functional polymers and/or functional nanofillers. The inclusion of inorganic nanoparticles, let available by electrospinning technique, matches well with one of the most ambitious challenge of materials science: create multifunctional material by design. This process allows the formation of materials with complex nanostructures, defined by particle and fiber morphology, composition, interface features.

Nanoparticles with antibacterial or photocatalytic/self-cleaning properties, can transfer such new functions to final polymeric product towards the creation of innovative hybrid multifunctional materials. The extremely high surface area of the electrospun nanofibers can further increase the functionality and applicability of the processed material.

The aforementioned active filtering media, that can offer both adsorption and high-efficiency filtration properties, can be obtained by electrospinning functional polymers able to react with toxic substances and pollutants. Among the functional polymers, bio-based polymers as proteins (keratin or fibroin) or carbohydrates, (chitosan), offer an attractive solution for the preparation of nanofibrous membranes able to adsorbs heavy-metal ions, dyes and VOCs. Furthermore, the incorporation of nanoparticles into nanofibers improve final performance, adding antimicrobial, self-cleaning and photocatalytic properties to keratin electrospun nanofibers.

The development of multifunctional filter media based on keratin nanofibers with TiO_2 and Ag NPs embedded has been carried out within the project “Nanotwice” (Composite Nanofibres for Treatment of air and Water by an Industrial Conception of Electrospinning - FdF SP1 – T1.2).

The fabrication of electrospun nanofibers with inorganic nanoparticles gives advantages in producing materials with a huge range of applications, not just limited to filtration, but also in developing biomaterials, bioelectronics and new textile materials.

3.5 References

[1] H. Gleiter, Acta Mater. 48 (2000) 1–29.

[2] A. N. Barenjee, Nanotechnol. Sci. Appl. 4 (2011) 35–65.

[3] F. E. Kruis, H. Fissan, A. Peled, J. Aerosol Sci. 29 (1998) 511–535.

[4] S. Zhang, D. Sun, Y. Fu, H. Du, Surf. Coat. Technol. 167 (2003) 113–119.

[5] M. Birkholz, U. Albers, T. Jung, Surf. Coat. Technol. 179 (2004) 279–285.

[6] S. R. Bakshi, D. Lahiri, A. Argawal, Int. Mater. Rev. 55 (2010) 41–64.

[7] E. Manias, Nature Materials 6 (2007) 9–11.

[8] G. Lalwani, A.M. Henslee, B. Farshid, L. Lin, F.K. Kasper, Y.X. Qin, A.G. Mikos, B. Sitharaman, Biomacromolecules 14 (2013) 900–909.

[9] G. Lalwani, A.M. Henslee, B. Farshid, P. Parmar, L. Lin, Y.X. Qin, F.K. Kasper, A.G. Mikos, B. Sitharaman, Acta Biomater. 9 (2013) 8365–8373.

[10] B.P. Singh, D. Singh, R.B. Mathur, T.L. Dhami, Nanoscale Res. Lett. 3 (2008) 444–453.

[11] P. S. Goh, B. C. Ng, W. J. Lau, A. F. Ismail, Separ. Purif. Rev. 44 (2015) 216–249.

[12] J.M. Arsuaga, A. Sotto, G. del Rosario, A. Martinez, S. Molina, S.B. Teli, J. de Abajo, J. Membr. Sci. 428 (2013) 131–141.

[13] S.-H. Park, H.S. Lee, J.H. Choi, C.M. Jeong, M.H. Sung, H.J. Park, J. Appl. Polym. Sci. 125 (2012) E675–E680.

[14] D. Ebert, B. Brushan, J. Colloid Interface Sci. 368 (2012) 584–591.

[15] V. Petrovič, V. Ducman, S.D. Škapin, Ceram. Int. 38 (2012) 1611–1616.

[16] D. Wu, M. Long, Surf. Coat. Technol. 206 (2012) 3196–3200.

[17] L.H. Mahajan, S.T. Mhaske, Mater. Lett. 68 (2012) 183–186.

[18] Y. Xu, H. Wang, Q. Wei, H. Liu, B. Deng, J. Coat. Technol. Res. 7 (2010) 637–642.

[19] B.H. Zhu, D. Wu, Y.H. Yang, Y.G. Chen, W.J. Li, J.F. Guo, Q.G. Wang, J. Chem. Eng. Data 57 (2012) 553–560.

[20] I. Sas, R.E. Gorga, J.A. Joines, K.A. Thoney, J. Polym. Sci. Pol. Phys. 50 (2012) 824–845.

[21] G. Li , H. Liu, TD. Li, J. Wang, Mat. Sci. Eng. C 32 (2012) 627–636.

[22] B. Mahltig, H. Haufe, H. Böttcher, J. Mater. Chem. 15 (2005) 4385–4398.

[23] B. Mahlting, T. Textor, Nanosols and Textiles, World Scientific in Hackensack, NJ, 2008.

[24] M.J. Uddin, F. Cesano, F. Bonino, S. Bordiga, G. Spoto, D. Scarano, A. Zecchina, J. Photochem. Photobiol. A: Chem. 189 (2007) 286–294.

[25] Z. Shi, I. Wymana, G. Liua, H. Hua, H. Zoub, J. Hub, Polymer 54 (2013) 6406–6414.

[26] M. Jafari, A. Rahimi, P. Shokrolahi, A. Ershad Langroudi, J. Coat. Technol. Res. 11 (2014) 587–593.

[27] D.P. Chattopadhyay, B.H. Patel, Journal of Natural Fibers, 8 (2011) 39–47.

[28] A. Bozzi, T. Yuranova, I. Guasaquillo, D. Laub, J. Kiwi, J. Photochem. Photobiol. A: Chem. 174 (2005) 156–164.

[29] T. Yuranova, R. Mosteo, J. Bandara, D. Laub, J. Kiwi, J. Mol. Catal. A: Chem. 244 (2006) 160–167.

[30] M.J. Uddin, F. Cesano, D. Scarano, F. Bonino, G. Agostini, G. Spoto, S. Bordiga, A. Zecchina, J. Photochem. Photobiol. A: Chem. 199 (2008) 64–72.

[31] D. Jocić, Surface modification systems for creating stimuli responsiveness of textiles, D. Jocić Ed., University of Twente, Enschede, The Netherlands, 2010, 37–59.

[32] C.M. Pastore, P. Kiekens, Surface characteristics of fibers and textiles, Marcel Dekker Inc., New York, 2001.

[33] M. I. Tobler-Rohr, Handbook of Sustainable Textile Production, Woodhaed publishing Cambrige, UK, 2011, 150–257.

[34] S. Gowri, A.L. Almeid, T. Amorim, N. Carneiro, A.P. Souto, M.F. Esteves, Textile Research Journal, 80 (2010) 1290–1306.

[35] Ž. Senić, S. Bauk, M. Vitorović-Todorović, N. Pajić, A. Samolov, D. Rajić, Scientific Technical Review 61 (2011) 63–72.

[36] L. Lin, Method of making fabric with photo-catalyst, US 2005/0227557 A1.

[37] K. Qi, X. Wang, J.H. Xin, Textile Research Journal, 81 (2011), 101–110.

[38] W.A. Daoud, J.H. Xin, J. Sol-Gel Sci. Techn. 29 (2004) 25–29.

[39] W.A. Daoud, J.H. Xin, Y.H. Zhang, Surf Sci. 599 (2005) 69–75.

[40] D. Li, Y. Xia, Adv. Mater. 16 (2004) 1151–1170.

[41] F.Ç. Cebeci, Z. Wu, L. Zhai, R.E. Cohen, M.F. Rubner, Langmuir 22 (2006) 2856–2862.

[42] M. Bellardita, A. Di Paola, L. Palmisano, F. Parrino, G. Buscarono, R. Amadelli, Appl. Catal. B: Environ. 104 (2011) 291–299.

[43] V. Bolis, C. Busco, M. Ciarletta, C. Distasi, J. Erriquez, I. Fenoglio, S. Livraghi, S. Morel, J. Colloid. Interf. Sci. 369 (2012) 28–39.

[44] E. Vulliet, J.-M. Chovelon, C. Guillard, J.-M. Herrmann, J. Photochem. Photobiol. A: Chem. 159 (2003) 71–79.

[45] J. Gunlazuardia, W. A. Lindu, J. Photochem. Photobiol. A: Chem. 173 (2005) 51–55.

[46] W.S. Tung, W.A. Daoud, J. Mater. Chem. 21 (2011) 7858–7869.

[47] K. Qi, J. H. Xin, W. A. Daoud, Int. J. Appl. Ceram. Technol. 4 (2007) 554–563.

[48] R.H. Wang, X.W. Wang, J. H. Xin, ACS Appl. Mater. Interfaces 2 (2010) 82–85.

[49] K. Qi, W. A. Daoud, J. H. Xin, C. L. Mak, W. Tang, W. P. Cheung, J. Mater. Chem. 16 (2006) 4567–4574.

[50] X. Zhang, H. Su, Y. Zhao, T. Tan, J. Photochem. Photobiol. A: Chem. 199 (2008) 123–129.

[51] T.P. Tim Cushnie, Peter K.J. Robertson, S. Officer, Pat M. Pollard, R. Prabhu, C. McCullagh, Jeanette M.C. Robertson, J. Photochem. Photobiol. A: Chem. 216 (2010) 290–294.

[52] Y.H. Tseng, C.-S. Kuo, C.H. Huang, Y.Y. Li, P.W. Chou, C.L. Cheng, M.S. Wong, Nanotechnology 17 (2006) 2490–2497.

[53] M. Chena, Y. Liu, J. Hazard. Mat. 174 (2010) 375–379.

[54] D. Gong, C.A. Grimes, O.K. Varghese, Z. Chen and E.C. Dickey, J. Mater. Res. 16 (2001) 3331–3334.

[55] G.K. Mor, O.K. Varghese, C.A. Grimes, J. Mater. Res. 18 (2003) 2588–2593.

[56] G.K. Mor, O.K. Varghese, M. Paulose, C.A. Grimes, Adv. Funct. Mater. 15 (2005) 1291–1296.

[57] K.S. Raja, M. Misra, K. Paramguru, Electrochim. Acta 51 (2005) 154–165.

[58] R. Apetrei, C. Catrinescu, D. Mardare, C.M. Teodorescu, D. Luca, Thin Solid Films 518 (2009) 1040–1043.

[59] M. Mirshekari, R. Azimirad, A.Z. Moshfegh, Appl. Surf. Sci. 256 (2010) 2500–2506.

[60] J. Kiwi, C. Pulgarin, Catal. Today 151 (2010) 2–7.

[61] S. Ganjoo, R. Azimirad, O. Akhavan, A. Z. Moshfegh, J. Phys. D: Appl. Phys. 42 (2009) 025302.

[62] M. Luo, W. Tang, J. Zhao, C. Pu, J. Mater. Process Tech. 172 (2006) 431–436.

[63] M.C. Ferrara, L. Pilloni, S. Mazzarelli, L. Tapfer, J. Phys. D: Appl. Phys. 43 (2010) 095301.

[64] T. Yuranova, D. Laub, J. Kiwi, Catal. Today 122 (2007) 109–117.

[65] N. Abidi, L. Cabrales, E. Hequet, Appl. Mater. Interfaces 1 (2009) 2141–2146.

[66] Q. Cheng, C. Li, V. Pavlinek, P. Saha, H. Wang, Appl. Surf. Sci. 252 (2006) 4154−4160.

[67] V. Ilić, Z. Šaponjić, V. Vodnik, B. Potkonjak, P. Jovančić, J. Nedeljković, M. Radetić, Carbohyd. Polym. 78 (2009) 564–569.

[68] F. Zhang, X. Wu, Y. Chen, H. Lin, Fibers and Polymers 10 (2009) 496–501.

[69] K. Kulthong, S. Srisung, K. Boonpavanitchakul, W. Kangwansupamonkon, R. Maniratanachote, Particle and Fibre Toxicology 7 (2010) 8.

[70] M. Radetić, J. Mater. Sci. 48 (2013) 95–107.

[71] N. Vigneshwaran, A.A. Kathe, P.V. Varadarajan, R.P. Nachane, J. Nanosci. Nanotechnol. 7 (2007) 1893–1897.

[72] Y.W.H. Wong, C.W.M. Yuen, M.Y.S. Leung, S.K.A. Ku, H.L.I. Lam AUTEX Res. J. 6 (2006) 18.

[73] R. Aladpoosh, M. Montazer, N. Samadi, Cellulose 21 (2014) 3755–3766.

[74] A. Bacciarelli-Ulacha, E. Rybicki, E. Matyjas-Zgondek, A. Pawlaczyk, M.I. Szynkowska, Ind. Eng. Chem. Res. 53 (2014) 4147–4155.

[75] D. Li, Y.N. Xia, Adv. Mater. 16 (2004) 1151–1170.

[76] S. Cavaliere, S. Subianto, I. Savych, D.J. Jones, J. Rozière, Energy and Environ. Sci. 4 (2011) 4761–4785.

[77] W.E. Teo, S. Ramakrishna, Nanotechnology 17 (2006) R89–R106.

[78] A. Martins, R.L. Reis, N.M. Neves, Int. Mater. Rev. 53 (2008) 257–274.

Chapter 4: SELF-CLEANING TEXTILES

In order to produce self-cleaning textiles, starting from commercial TiO_2 nanosol, three studies were carried out, examining the main issues relative to applicability of products, technology transfer, industrial scale-up and understanding of mechanisms involved in photocatalytic processes.

Initially, an optimization study inherent to neutralization/purification treatments on commercial TiO_2 nanosol was performed. Thus commercial and modified (neutralized) TiO_2 nanosols were used and applied on textiles.

TiO_2 nanosols and relative functionalised textiles were studied and characterized. In particular, a deep investigation on relationship between TiO_2 based nanosols, nanocoatings properties and their performances in term of hydrophilicity and photocatalytic efficiency was carried out, analyzing five nanosols, differing for chemical surface, pH and relative agglomerates size. So, the correlation between physicochemical characteristics of nanosols and functional properties of coatings was studied.

Finally, with the aim to establish appropriate experimental conditions with which to measure the photocatalytic efficiency of nano-TiO_2 based materials, a deep study on measurements and experimental conditions involved in photocatalytic tests was made. The efficiency in the photodegradation of organics, in our case an organic dye, Rhodamine (RhB), was investigated in different experimental settings, inherent the self-cleaning application: TiO_2 nanoparticles in solution, TiO_2-coated textile dipped in solution and stain on TiO_2-coated textile. The different experimental set-ups let to assess interfaces where nano-TiO_2 played its photocatalytic activity and provided information about self-cleaning mechanism.

4.1 Experimental Section

4.1.1 Materials

TiO_2 nanosol (NAMA41, 6 wt %) called TAC, neutralized TiO_2-nanosol (NAMA41N) characterized by the presence of organic coating, called TN were purchased by Colorobbia (Italy). TiO_2 nanopowder P25, used as benchmark material, was purchased by Evonik. Ammonium bicarbonate (purity ≥ 99.0%), rhodamine B (dye content ~ 95%) used as target dye, anion exchange resin Dowex® 66, were purchased by Sigma Aldrich. Textile fabrics used for NPs incorporation and self-cleaning tests were polycottons, exploited for soft furnishings, with specific weight of 360 g/m^2 and composition: 62% cotton - 38% polyester. Cotton based fabrics are particularly exploited in self-cleaning applications, because their hydrophilic nature promotes the adhesion of metal oxide NPs, as TiO_2 NPs useful in this work.

4.1.2 Preparation of neutralized TiO_2 nanosuspensions

The issue of self-cleaning textile production, on an industrial scale, with commercial TiO_2 nanosols is faced. In order to increase TiO_2 commercial nanosol applicability with the aim to produce self-cleaning textiles and improve the photocatalytic final properties, three different treatments, able to purify and neutralize the TiO_2 commercial nanosol, were developed. The three different treatments applied to TiO_2 nanosol, TAC, were:

1. Washing by ultrafiltration (TACF)
2. Purification by anion exchange resin (TACR)
3. Neutralization of TAC-coated textile (TACBIC)

1. Washing by ultrafiltration (TACF)

Ultrafiltration was carried out using Solvent-resistant Stirred Cell (Merck Millipore) with polymeric membrane with a pore size of 100 kDalton (kDa), corresponding to a cutoff size of 7 nm, which enabled the retention of TiO_2 nanoparticles, by this way the pH increased while synthesis by-products were removed. The vessel refilled with water

was performed for several times until the achievement of wished characteristics. The ultrafiltered sample (TACF) was undergone vessel refilled with water until pH 4.0.

2. *Purification by anion exchange resin (TACR)*

The purification by anion exchange resin process involved the addition of weak anion exchange resin (Dowex® 66) in TiO_2 nanosol. The resin was able to sequester Cl^- ions and release OH^- ions with a consequent pH increase. Reaching the wished pH value, the resin was removed through simple separation. The obtained pH value in purified sample (TACR) was 4.5.

3. *Neutralization of TAC-coated textile (TACBIC)*

The neutralization treatment of TAC-coated textile (TACBIC) involved, first of all, the application of commercial TiO_2 nanosol (TAC) onto textile by dip-padding-curing method (described below). Afterward, an aqueous ammonium bicarbonate (NH_4HCO_3) solution (0.5M) were deposited onto TAC-coated textile by manual spray-gun technique, in order to neutralize the acidity of commercial TiO_2 nanosol.

All nano-TiO_2 samples were used with a TiO_2 content of 3 wt%.

4.1.3 Preparation of TiO_2 nanosuspensions with different pH

The commercial nanosols (TAC and TN) characterized by different pH and ultrafiltered samples (TACF), starting from TAC nanosol, were prepared. In this regards, by changing the washing degree, three nanosols samples were prepared with different pH values: 3.5, 4.0 and 4.2 (called TACF3.5, TACF4.0 and TACF4.2 respectively) through the washing by ultrafiltration method, described in detail in Section 4.1.2.

4.1.4 Characterization of TiO_2 nanosuspensions

NP hydrodynamic diameters were obtained from dynamic light scattering (DLS) data performed by Zetasizer Nanoseries (Malvern Instruments, UK), setting the measurement angle to 173° and the measurement duration on automatic. After 2 min

temperature equilibration step, 1 ml of sample volume (0.3 wt%) was subjected to three consecutive measurements performed at 25° C and particle size distributions by intensity were obtained by averaging these measurements. DLS analysis also provides a polydispersion index parameter (PDI), ranging from 0 to 1, quantifying the colloidal dispersion degree; for PDI below 0.2 a nanosol can be considered as monodispersed.

The ζ potential of nanosol samples was evaluated by means of electrophoretic light scattering (ELS) (Zetasizer Nanoseries - Malvern Instruments, UK). The instrument, equipped with an automatic titrating system, was used to determine the ζ potential of nanosols as a function of pH (experimental uncertainty: 1 mV for ζ potential and 0.2 for pH). The measurements were carried out on nanosols with 0.3 wt % concentration. The titration was performed by addition of 0.01 M KOH solution. For each sample three measurements were performed and the ζ potential average values were considered.

The phase composition was determined by X-ray diffraction (XRD). Analysis was performed by a Bragg-Brentano diffractometer (Bruker D8 Advance, Germany) operating in θ/2θ configuration, with a XCeleretor detector (20-70 ° 2θ range, 0.02 step size, 0.5 s time-per-step).

The electrical conductivity was measured with a conductimeter (AMEL 134, AMEL) on nanosols at the phase concentration of 0.3 wt %.

The specific surface area (SSA) measurements were determinate by Brunauer-Emmett-Teller (BET) method. It is a well-recognized approach to determine the SSA of nanoporous materials which is based on physical adsorption of gas molecules onto the material interface [1,2]. The specific surface area (BET) measurements were carried out using N_2 as adsorptive gas Sorpty 1750 (Carlo Erba, Italy).

4.1.5 Functionalization method on textile support

Nanosol samples based on TiO_2 were applied on textile supports by a typical functional finishing technology called dip-padding-curing method (Fig. 4.1). Initially, fabric samples were washed in ultrasound bath with distilled water for 30 min. Washed samples were dipped in TiO_2 based nanosols, with TiO_2 content of 3 wt%, soaked at the room temperature for 3 min, and pressed with horizontal two-roller laboratory padder.

Then the fabric was dried in an oven at 100°C for 15 min and cured at 130°C for 10 min.

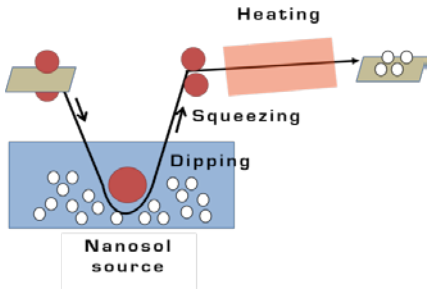

Figure 4.1 Schematic representation of dip-padding-curing method.

The TiO_2 amount absorbed on the fabric substrates was evaluated by weighting the solid residue after burning at 800°C for 30 min, with a heating rate of 100°C/h (burn-out). Moreover, on TACF3.5-coated textile sample, a further investigation inherent the presence of nano-TiO_2 on textile was performed. So, in order to test the TiO_2 NPs adhesion onto textile surface, the burn-out test was also applied to fabrics washed at 40°C for 90 min with washing machine for ten and twenty cycles, detecting TiO_2 coating stability after several washing. Finally, the presence and the morphology of nano-TiO_2 coating were investigate by a scanning electronmicroscope (SEM, Leica, Cambridge Stereoscan 360, UK).

4.1.6 Hydrophilicity

In order to increase the knowledge of structure-reactivity relationships, the hydrophilic behavior of coatings based on nano-TiO_2 supported on different substrates (fabric, glass and ceramic) was assessed.

The hydrophilic behavior of TiO_2 coatings was estimated by sessile drop method (contact angle measurements) on TiO_2 coated ceramic/glass substrates. The TiO_2 coated ceramic/glass substrates were prepared by classic dip coating method (Fig. 4.2). Before nano-TiO_2 deposition, glass supports were immersed in acetic acid solution for 7 h and then air dried for 24 h, while ceramic tiles were washed with EtOH:water solution (10:90 v/v) under ultrasound bath for 15 min and then air dried for 24 h. TiO_2 films

were deposited at room conditions (namely temperature = 21°C and humidity of air = 45%) onto glass and ceramic supports by dip coating, as follows: dipping for 5 s in the colloidal nanosuspension, withdrawal from it at constant velocity (2 mm/s).

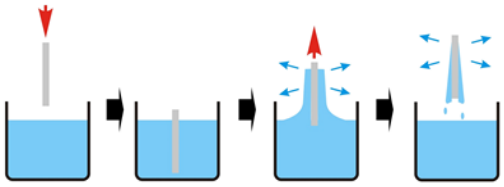

Figure 4.2 Schematic representation of dip coating method, applied on ceramic tiles and glass supports.

The coated samples were air dried and subsequently treated in oven for 10 min at 130°C to promote adhesion to the support. So, the hydrophilicity was evaluated by the sessile drop method, measuring the contact angle of a water drop on the coated glass or ceramic surface with an optical tensiometer OCA plus (Data Physics Instruments, Germany). For each sample five measurements were performed and the average value was considered. Despite that the hydrophilicity of TiO_2 modified fabrics depends both on hydrophilicity of TiO_2 coatings and on characteristics of textile support, such as structure, composition and water content, it was possible to make a sound extrapolation between contact angles-based hydrophilicity of ceramic/glass samples and that of textile samples, because the characteristics of textile support were the same for all sample investigated. Besides, the typical high hydrophilicity of textiles increases the difficulty in the use of textile support in contact angle measurements, masking the variances in behavior of different coatings.

4.1.7 Photocatalytic measurements

Different experimental conditions were imposed to assess the photocatalytic performance of the nano-TiO_2.

4.1.7.1 TiO_2 in sol (a)

Photocatalytic degradation of Rhodamine B (RhB) was conducted in a beaker at room temperature. TiO_2 based nanosols or nanopowder (P25), were added to RhB aqueous solution (0.07 g/ L), at a final volume of 50 mL and final TiO_2 concentration of 2.7 wt%. Distilled water was used as blank. The sol was stirred and UV irradiated with intensity of 9 W/m^2 and an average illumination wavelength λ = 350 nm (Osram ULTRA-Vitalux lamp 300 W). The lamp was switched on 30 min before the beginning of photocatalytic test to stabilize the power of its emission spectrum. The irradiated surface area was 19.62 cm^2. The distance between sample and lamp was kept constant at 25 cm. The progress of the degradation reaction was controlled at regular times by taking 3 mL of solution and measuring the absorbance at λ= 554 nm with a single beam spectrophotometer (UV/Vis Spectrophotometer S-22, Boeco, Germany). Analyses were performed using a quartz cuvette as sample-holder. The photocatalytic activity was quantified as the photodegradation rate constant of catalyst, k (min^{-1}). The value of k was assessed, plotting $\ln(C_0/C)$ versus time (t), where C_0 is the initial RhB concentration e C the RhB concentration after a certain time. The photonic efficiency (ξ) is defined as the ratio of initial RhB degradation rate and the incident photon flux and calculated by the formula [3]:

$$\xi = \frac{kC_0}{I_0} \qquad \text{(Eq. 4.1)}$$

where k is the rate constant in min^{-1}, C_0 the initial RhB concentration in mol L^{-1} and I_0 the incident photon flux per volumetric unit (Einstein L^{-1} min^{-1}) calculated in accordance to the equation:

$$I_0 = \frac{I\lambda A}{N_A hcV} \qquad \text{(Eq. 4.2)}$$

where I is the light intensity (W/m^2), λ the wavelength (nm), A the irradiated surface area (m^2), N_A Avogadro's number, h the plank constant (J s), *c* the light velocity (m/s) and V the volume of the suspension (L).

The photocatalytic efficiency indicates the ratio between the amount of reagent consumed and the amount of reagent initially present in the reaction environment. According to the Lambert-Beer law, the absorbance is proportional to RhB concentration, so the photocatalytic efficiency (%) was determined by formula:

$$\text{Photocatalytic efficiency (\%)} = \frac{A_0 - A_t}{A_0} \, x \, 100 \qquad \text{(Eq. 4.3)}$$

where A_0 is the initial absorbance and A_t is the absorbance after a certain irradiation time t.

Moreover, spent the time necessary for RhB photodegradation, for each solution, UV–vis spectra were collected in the 200–800 nm range with a Lambda 35 spectrophotometer (PerkinElmer, UK), working in a double beam mode. Analyses were performed using a quartz cuvette as sample-holder.

4.1.7.2 TiO_2-coated textile (b)

The photocatalytic degradation of RhB was conducted in a beaker at room temperature. 5.46 mL of RhB aqueous solution (0.07 g/L) and TiO_2 coated fabric (0.45 g) were added to 44.54 mL of water. Uncoated fabric was taken as blank. Prior to irradiation, the system was kept in the dark for 20 h to ensure the establishment of an adsorption–desorption equilibrium between TiO_2-coated fabric support and RhB dye (irradiation and measurement as in Section 4.1.7.1).

4.1.7.3 Stain on TiO_2-coated textile (c)

Both pristine fabrics and titania-coated samples were stained with four drops (~20 μL) of RhB aqueous solution (1.29 g/L). After staining, the samples were irradiated with UV radiation intensity of 9 W/cm^2 (Osram ULTRA-Vitalux lamp). The lamp was

switched on 30 min before the beginning of the photocatalytic test to stabilize the power of its emission spectrum. The distance between sample and lamp was kept constant at 25 cm. In order to assess the degree of discoloration, the samples underwent colorimetric measurements before and after UV exposure. All colorimetric measurements were performed by DRS (Miniscan MSXP4000, Hunter Lab, USA) in the 400-700 nm range (illuminant D65, observer 10°). Color is expressed as CIELab parameters: brightness (L*: 100 = white 0 = black) and chroma (a*: red +, green -; b*: yellow +, blue -). The photocatalytic performances were evaluated by assessing the discoloration, expressed as photocatalytic efficiency (%). In particular, the color difference (ΔE*) between samples before and after exposure, calculated as follows:

$$\Delta E^* = \sqrt{(\Delta L^*)^2 + (\Delta a^*)^2 + (\Delta b^*)^2} \qquad \text{(Eq. 4.4)}$$

was referred to the pristine sample by subtracting the background color of the fabric (Fig. 4.3).

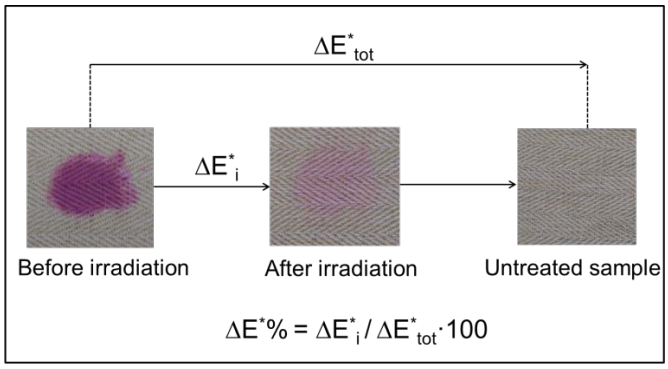

Figure 4.3 Photocatalytic efficiency (%) expressed as color difference (ΔE*%).

In order to compare the results inherent to efficiency in RhB photodegradation, RhB/TiO_2 weight ratio was kept constant in any set-up analyzed (a, b and c).

4.2 Results and discussion

4.2.1 Optimization of neutralization/purification treatments

In order to produce self-cleaning textiles, initially, the commercial TiO_2 nanosol (TAC) was used to coat the textile supports, but some problems were found. In fact, due to very low pH and very high conductivity of as purchased commercial TiO_2 nanosol (TAC) (Table 4.1) its application was not possible, in particular the purification treatments were absolutely necessary for two main reasons: 1) the textile substrate was damage by acidity lower than 3.5 pH units; 2) the presence of synthesis residual byproducts in TiO_2 commercial nanosol could decrease significantly the photocatalytic activity. So a neutralization/purification treatment was needed.

The three different treatments applied to TAC nanosol were:

1. Washing by ultrafiltration (TACF)
2. Purification by anion exchange resin (TACR)
3. Neutralization of TAC-coated textile (TACBIC)

A fundamental aspect to be considered is the change in physicochemical properties as pH, surface charge and conductivity resulting from these treatments. The consequent problems could be the agglomeration, aggregation or coagulation in nanosuspensions, so it was necessary to avoid the colloidal destabilization [4,5].

Table 4.1 Physicochemical characteristics of TiO_2 nanosol samples.

	Nominal pH	pH[a]	d_{DLS} (nm)	PDI	Electrical conductivity (mS/cm)	$pH_{i.e.p.}$[c]
TAC	1.5	2.9	36	0.25	1.18	7.09
TACF	4.0	3.3	96	0.35	0.25	6.92
TACR	4.5	4.2	94	0.40	0.05	6.91
TACBIC	-	5.0[b]	-		-	-

[a] pH measurement of nanosol (0.1 wt % TiO_2 concentration)
[b] pH measurement onto textile surface
[c] Titration measurements carried out on nanosol at low concentration (0.1 wt %) to prevent precipitation due to pH changes

4.2.1.1 Properties of purified TiO_2 nanosols

Commercial and modified TiO_2 nanosols were characterized. In Figure 4.4, the XRD diffractogram of TAC sample is shown, the broad peaks typical of nano-sized crystallites were detected. The main phase detected was anatase (JCPDS card n. 21-1272) with a small amount of brookite (JCPDS card n. 29-1360). Co-existence of anatase and brookite frequently occurs in water-based synthesis but the photocatalytic activity, which is primarily responsible for the phase anatase, is preserved [6].

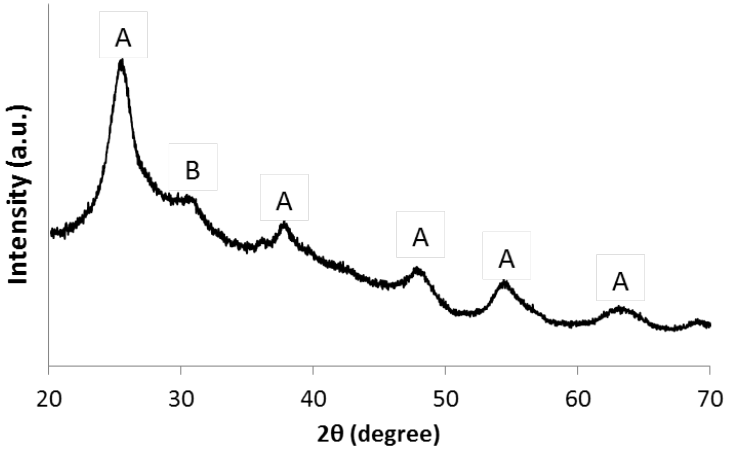

Figure 4.4 XRD diffractogram of TAC sample (A = anatase; B = brookite).

The three different treatments on commercial TiO_2 nanosol (TAC) allowed an increased in pH and size and a decrease in conductivity (Table 4.1).

The DLS data showed an increase in diameter (in TACF and TACR samples), which was caused by the increase of the degree of agglomeration, also associated with an increase of pH. An increase of PDI was observed in correspondence of the DLS data, justified by the increase of agglomeration degree that led to a greater polydispersability.

In Figure 4.5 the ζ potential vs pH results of three different purified TiO_2 nanosols are shown. The measurement of ζ potential as a function of pH, let to identify the isoelectric point, the pH at which ζ potential sets to zero ($pH_{i.e.p.}$). As evidenced in equations (Eq. 4.5-4.7), TiO_2 shows in water the typical behaviour of amphoteric hydroxylated metal oxides, being protonated and positively charged at pH lower than pH of zero charge

(pH_{pzc}), while is negatively charged at pH higher than pH_{pzc}. If no specific adsorption of solubilized species occurs, pH_{pzc} equals $pH_{i.e.p.}$ [7].

$$Ti^{IV} + H_2O \rightarrow Ti^{IV} - OH + H^+ \quad \text{(Eq. 4.5)}$$

$$Ti^{IV} - OH + H^+ \rightarrow Ti^{IV} - OH_2^+ \quad \text{(Eq. 4.6)}$$

$$Ti^{IV} - OH \rightarrow Ti^{IV} - O^- + H^+ \quad \text{(Eq. 4.7)}$$

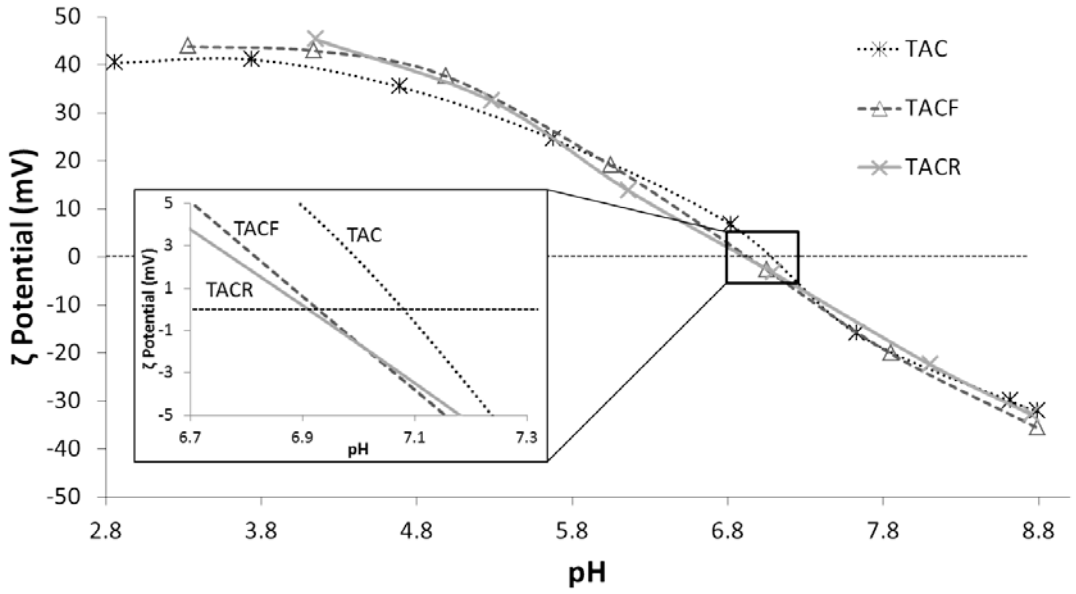

Figure 4.5 ζ Potential vs pH of samples: TAC, TACF and TACR. The measurements were carried out on nanosol at low concentration (0.1 wt %) to prevent precipitation due to pH changes.

The three curves, shown in Figure 4.5 are quite similar, but, from TAC sample to TACR sample, a slight shift of $pH_{i.e.p.}$ towards acid pH is observed and associated to the increase of agglomeration. These data seem indicate that the increasing in agglomeration degree let to an increase of surface acidity. Furthermore, visual observations on TiO_2 coated textiles, subsequently confirmed by experimental data (Section 4.2.2), showed a correspondence between agglomeration and surface hydrophilicity.

The successful purification of commercial TiO_2 nanosol (TAC) was demonstrated by increase of pH and decrease of conductivity in TACF and TACR samples (Table 4.1).
The high value of electrical conductivity in TAC sample was associated with the presence of synthesis residual by-products, in particular HCl.
The increase of pH in neutralization/purification processes was limited to a maximum value (pH< 4.5) because at pH > 4.5 the TiO_2 nanosol underwent a colloidal destabilization. An efficient removal of by-products, in particular Cl^- anions, was performed by the anion resin exchange.
The reaction exchange is as follows:

$$R\text{-}NH_3OH + Cl^- \rightarrow R\text{-}NH_3Cl + OH^- \qquad \text{(Eq. 4.8)}$$

A good correspondence between the shift of $pH_{i.e.p.}$ towards acid pH and the conductivity decrease as a function of starting pH was found as shown in Figure 4.6.
In particular, the sample TACR showed a very low conductivity value, demonstrating the greater efficiency in the by-products removal for the purification process by anion exchange resin.

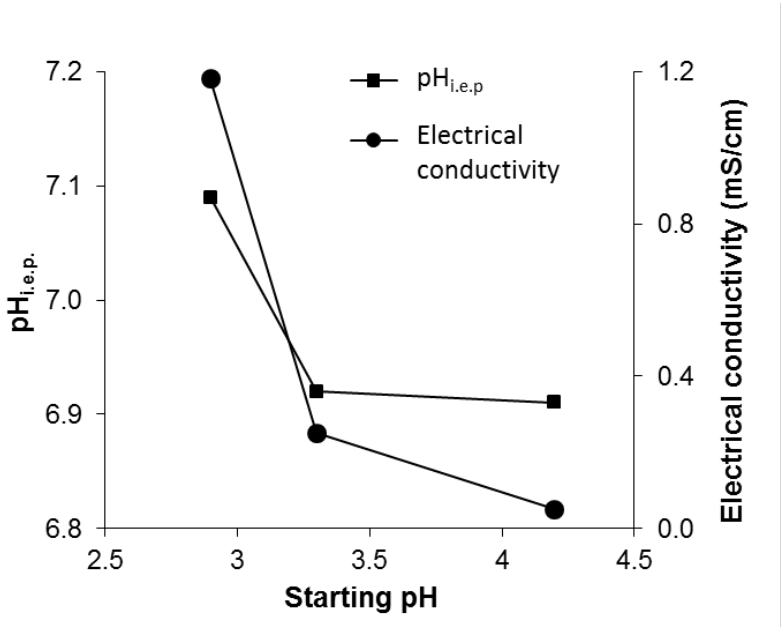

Figure 4.6 The influence of starting pH on $pH_{i.e.p.}$ and electrical conductivity.

The easily regeneration of anion exchange resin by washing with highly concentrated NaOH solution [8,9] confirms the cost-effectiveness and easily scalability of purification by exchange resin, as many papers, inherent to large-scale ion exchange process, demonstrate [10-14].

4.2.1.2 Properties of purified TiO_2 nanosols within application

A brief characterization inherent the presence of coating on textile was made. The burn-out test confirmed the formation of a homogenous coating of nano-TiO_2: a white TiO_2 powder agglomerate with an appearance perfectly mimicking the texture of fabric fibers was achieved (Fig. 4.7).

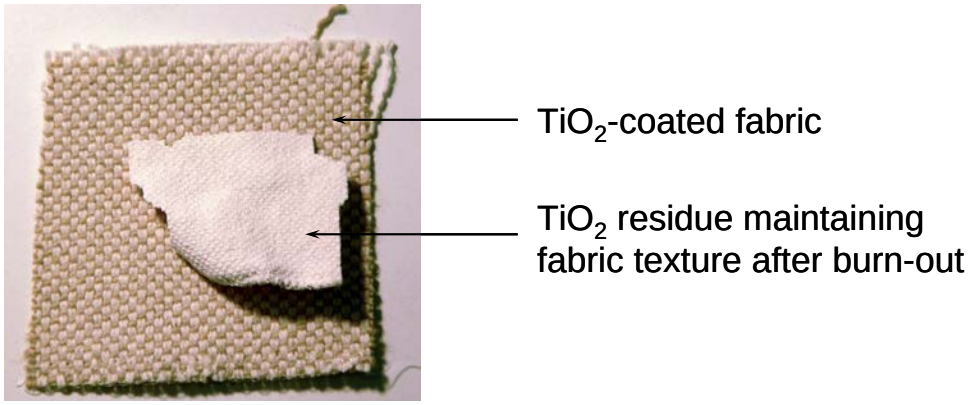

Figure 4.7 Photograph of burn-out powder.

The amount of TiO_2 (about 3 wt %) is coherent with the capacity of tested cotton based fabrics to adsorb an amount of nanosol equal to their weight. In particular, the TiO_2 residual amount after burn-out was 3.0, 3.4, 3.5 and 3.0 wt% in the TAC, TACF, TACR and TACBIC coated textile samples, respectively.

The photocatalytic activity was assessed as discoloration of RhB stains on pristine and coated fabrics with different treated TiO_2 nanosols (experimental set-up "Stain on TiO_2-coated textile" (c), Section 4.1.7.3). The results showed the following trend: TACR >TACF >TACBIC >TAC (Fig. 4.8).

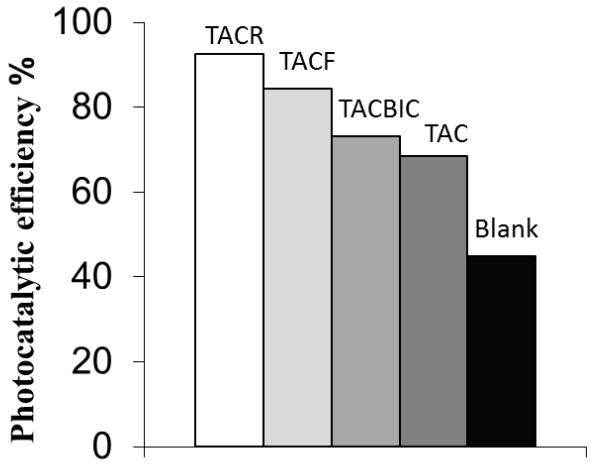

Figure 4.8 Photocatalytic efficiency (%) as a function of neutralization treatment on TiO_2 coated fabrics. The blank represents the uncoated fabric.

Expressing, the photocatalytic results as increased photochemical efficiency values, which were calculated using the photocatalytic efficiency value of uncoated fabric, as reference (Fig. 4.9), it was observed an improvement in the photoactivity in correspondence of the various treatments.

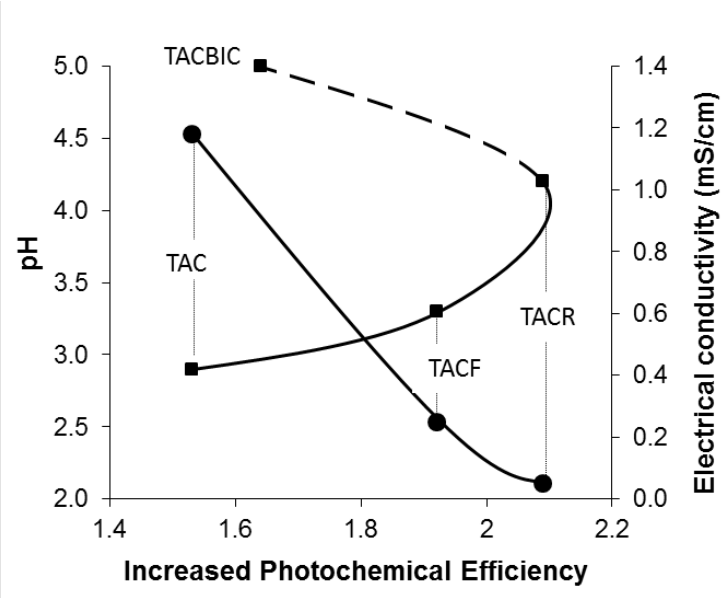

Figure 4.9 Increased photochemical efficiency as a function of pH (■) and electrical conductivity (●).

As expected, the presence of synthesis residual by-products in TiO_2 commercial nanosol (TAC) caused the achievement of low photocatalytic efficiency values. Despite the post-neutralization, namely an increase in pH onto the surface of TiO_2-coated fabric, the photocatalytic performance of sample TACBIC was slightly higher than TAC sample. Probably the presence of synthesis residual by-products in this sample hindered the photocatalytic activity. The greater results were obtained with treatments directly applied to the nanosol (TACF and TACR sample). Despite the high degree of agglomeration in TACR sample, the treatment of purification by anion exchange resin provided the best performance. So, the main parameter that contributed to the improvement of photocatalytic performance was the synthesis residual by-products removal, demonstrated by low conducibility and high pH that indicated an high surface acidity hence an high hydrophilicity. The photocatalytic results showed the importance of using a purified nanosol in order to obtain final products with high photocatalytic performance. Unfortunately, the neutralization treatment resulted less effective than the by-products removal to improving photocatalytic performance, as the low photoreactivity in TACBIC-coated fabrics demonstrates.

4.2.2 Correlation between physicochemical characteristics of nanosols and functional properties of coatings [15]

A deep investigation on relationship between TiO_2 based nanosols, nanocoatings properties and their performances in term of hydrophilicity and photocatalytic efficiency was performed. Five nanosols, differing for chemical surface, pH and relative agglomerates size were studied. So the samples exploited in these studies were TAC, TACF3.5, TACF4.0, TACF4.2 and TN.

4.2.2.1 Properties of modified TiO_2 nanosols

The XRD patterns (Fig. 4.10) confirmed that starting pH change did not affect the crystalline phases. The broad peaks typical of nanosized crystallites were detected. All

samples showed anatase (JCPDS card n. 21-1272) as was predominant phase, though the samples contain also brookite (JCPDS card n. 29-1360 – about16 wt%).
The DLS hydrodynamic diameters of TiO_2 nanosols were reported in Figure 4.11.

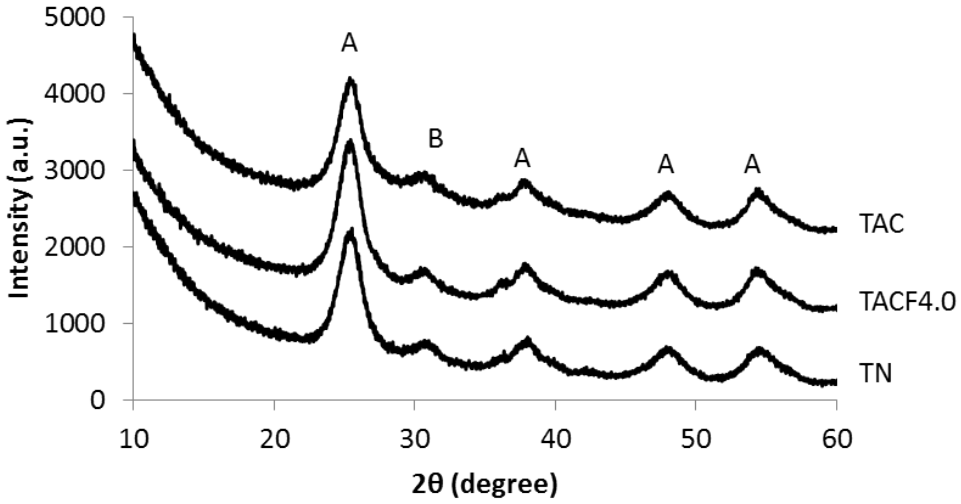

Figure 4.10 XRD diffractograms of TAC, TACF4.0 and TN samples.

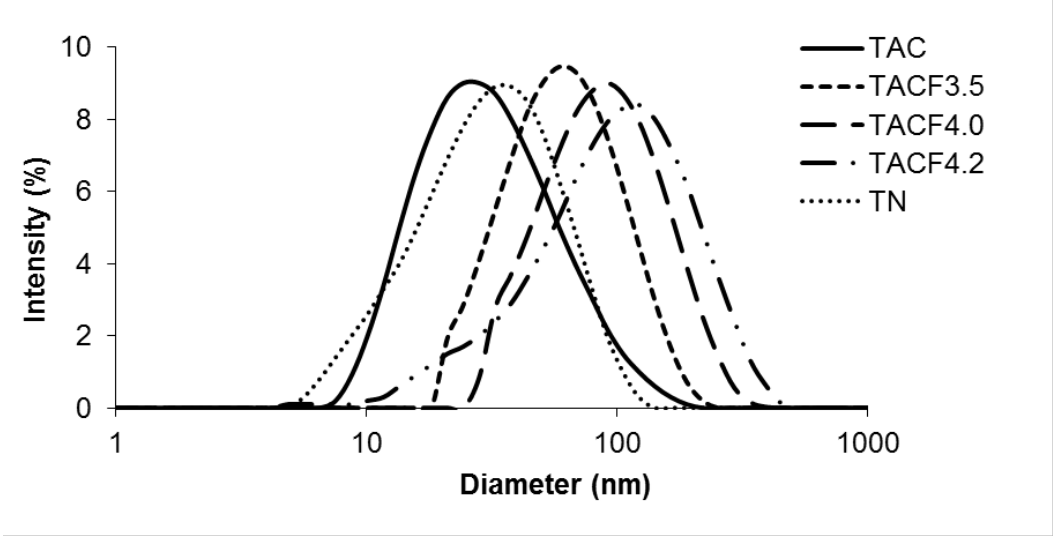

Figure 4.11 The influence of pH on the hydrodynamic diameter of nanosols.

Excepting the sample TN, the higher was the pH of nanosol (going from TAC to TACF4.2) the larger was the hydrodynamic diameter, because the degree of agglomeration progressively increased. This was confirmed also by the increase of PDI data. The sample TN resulted well dispersed, as demonstrated by the low PDI value, because agglomeration phenomena were avoided by the presence of a neutralizing agent which could act as capping agent. It worth to note that the commercial nanosols (TAC and TN) could be considered monodispersal sample (with PDI values slightly higher than 0.2), on the other hand, the ultrafiltered samples showed increased PDI values, although they can be considered good results. BET results, obtained on spray-dried samples, reported in Table 4.2 were coherent with DLS size values.

Table 4.2 Physicochemical characteristics of the TiO_2 nanosol samples: hydrodinamic diameter by DLS (d_{DLS}) with relative PDI, pH of isoelectric point ($pH_{i.e.p.}$) and specific surface area by BET (SSA_{BET}).

Sample	pH	d_{DLS} (nm)	PDI	$pH_{i.e.p}$	SSA_{BET} ($m^2 g^{-1}$)
TAC	1.5	36	0.25	7.7	237
TACF3.5	3.5	66	0.30	6.3	nd
TACF4.0	4.0	96	0.35	6.1	190
TACF4.2	4.2	119	0.31	5.9	nd
TN	6.0	44	0.27	<2.0	36

nd: not determined

The spray-drying process used to obtain the powder from nanosol was able to preserve the nanostructure in the spray-dried powders, as confirmed by the high values of SSA (Table 4.2). It was demonstrated that the spray-drying is a good method to granulate a powder from colloidal suspension [16]. So, the highest surface area of the most acid sample TAC, corresponds to the smallest particle size. In ultrafiltered samples, some agglomeration phenomena occured, as evidenced by the decreasing of specific surface area. However, the sample TN, although its very small particle size (d_{DLS} = 44 nm), showed the lowest surface area, maybe due to the presence of carbon residues after spray-drying, originated from organic molecules used as neutralizing and stabilizing

agent. The probable consequent formation of sticky aggregates let available less free surface for the interaction with N_2 gas, during BET measurements [17].
In Figure 4.12, the measurements of ζ potential as a function of pH were shown.

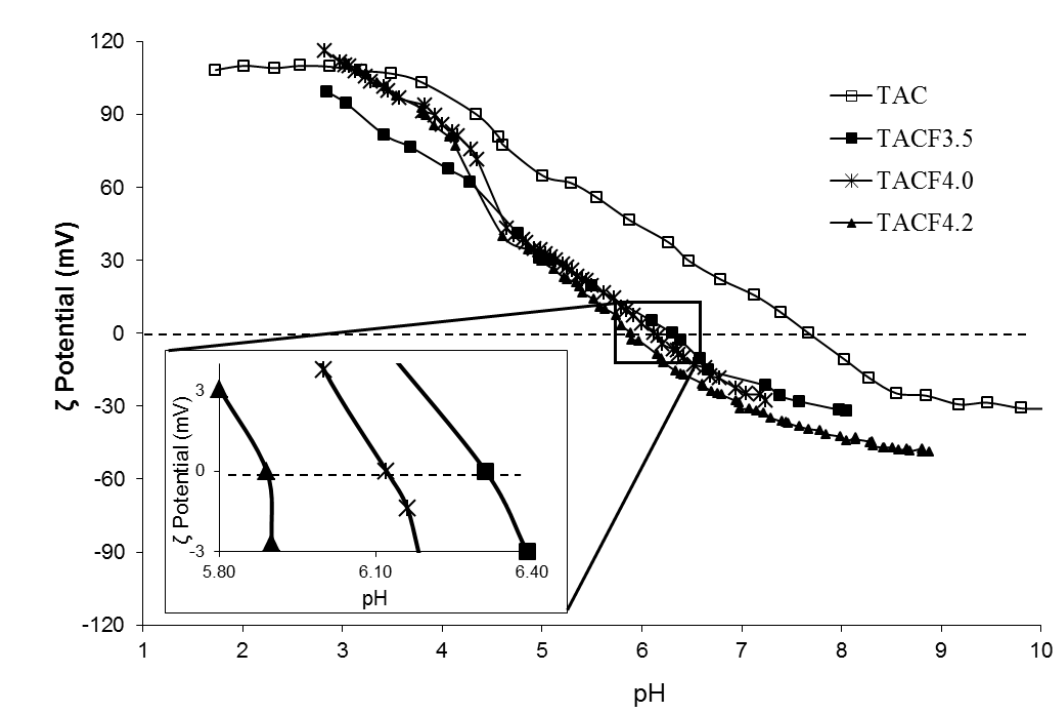

Figure 4.12 The influence of pH on ζ potential of TiO_2 nanosols.

Whereas the correlation between $pH_{i.e.p.}$ and surface acidity [18,19], a shift of $pH_{i.e.p.}$ towards acid pH could be considered as an increase in surface acidity . The strong shift of $pH_{i.e.p.}$ in TN nanosol at values <2, compared with pH range (5–7) reported in literature for colloidal titania [4] was justified by the presence of organic neutralizing agent that transfer a negative net charge on the surface. The behaviour was different for bare TiO_2 nanosol (TAC and TAFC samples); in this case a slight shift of $pH_{i.e.p.}$ towards acid pH from TAC sample to TAFC samples, increasing starting pH ($pH_{i.e.p.}$ TAFC3.5 > TAFC4 ≥ TAFC4.2) may be related only to different nanostructures (agglomeration degree). As already discussed in literature [4,20], due to the high surface reactivity of nanomaterials, small changes in surface chemistry, presence of contaminants or synthesis by-products, as well as morphological differences (due to

agglomeration phenomena) may affect the $pH_{i.e.p}$. In particular, the observed different surface acidity of TAC and TAFC sample, as well as small differences within TAFC samples set, may be justified by different agglomeration degree, as hydrodynamic diameters size reported in Table 4.2 reveal. In fact, as schematized in Figure 4.13, a complex aggregated structure has most chances to stabilize negative charges arising from surface de-protonation.

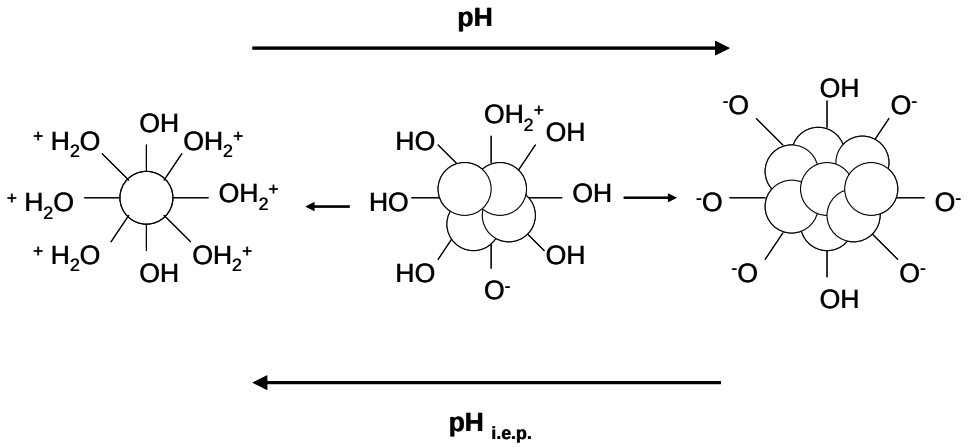

Figure 4.13 Schematic representation of surface properties of TiO_2 dispersed nanoparticles as a function of pH and agglomeration state.

4.2.2.2 Properties of modified TiO_2 nanosols within application

The formation of a homogenous coating of nano-TiO_2 on textile was proved by burn-out test, confirming an amount of 3 wt% TiO_2 on textile. Furthermore, the adhesion of coating was further assessed by burn-out test results after washing at 40 °C for ten and twenty cycles on TACF3.5 coated textile sample. All results were shown in Table 4.3.
SEM analysis (Fig. 4.14) showed the surface morphology change induced by the presence of TiO_2 coating. Differently from the smooth texture of the uncoated fiber (Fig. 4.14a), TACF3.5-coated fabric fiber (Fig. 4.14b) showed a certain surface roughness due to the TiO_2 thin layer attached to the textile substrate.

Table 4.3 Burn-out test results. Weight loss of the coated fabrics after burning: before washing, after ten and twenty washing. Experimental conditions: temperature = 800 °C, heating rate = 100 °C/h and residence time = 15 min.

Sample	% TiO_2 before washing	% TiO_2 after 10 washings	% TiO_2 after 20 washings
TAC	3.0	-	-
TACF3.5	3.2	2.8	2.7
TACF4.0	3.4	-	-
TACF4.2	3.6	-	-
TN	2.9	-	-

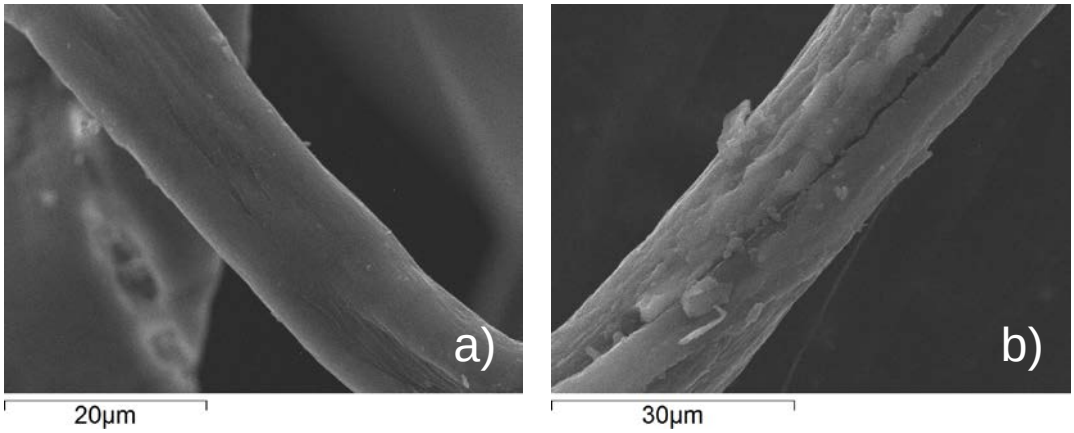

Figure 4.14 SEM micrographs of a) uncoated fabric fibre and b) fabric fibre coated with the TACF nanosol.

As evidenced by hydrophilicity data reported on Table 4.4 and Figure 4.15, the surface acidity trend affected the hydrophilicity of TiO_2 coated supports.

Both glass and ceramic tile surfaces, in fact, showed a decreasing of contact angles as increasing starting pH of TiO_2. The high concentration of $Ti\text{-}O^-$ sites, present on more acidic surfaces, promoted the formation of hydrogen bonds with water molecules, with an improved hydrophilicity.

Table 4.4 Contact angle measurements and relative standard deviation (σ) on TiO_2 thin films supported on glass substrates and ceramic tile.

Sample	pH	Contact Angle (°) ± Standard Deviation (σ)	
		Glass substrate	Ceramic tile
Pristine	-	57.3 ± 2.3	60.0 ± 2.0
TAC	1.5	44.2 ± 2.2	45.8 ± 3.9
TACF3.5	3.5	34.2 ± 3.6	40.8 ± 2.7
TACF4.0	4.0	20.7 ± 1.4	28.3 ± 3.3
TN	6.0	7.0 ± 1.5	9.2 ± 2.1

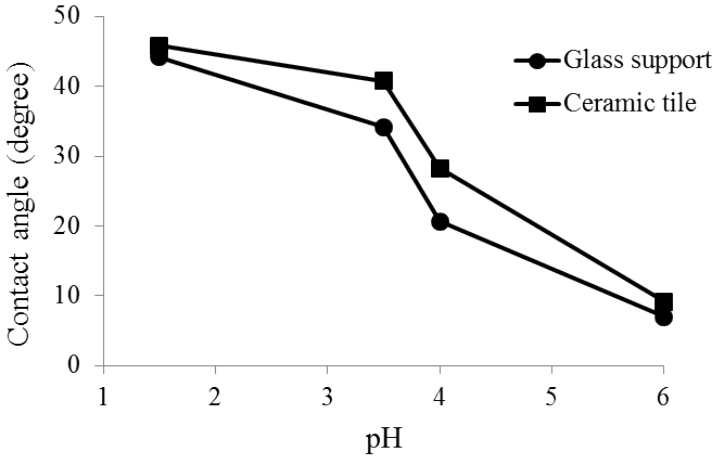

Figure 4.15 The influence of nanosol pH on the contact angle values

The photocatalytic activity was assessed as discoloration of RhB aqueous solution and red wine stains on pristine and coated fabrics. Both tests proved an increase in the photocatalytic performances by increasing the starting pH of the nanosol (Table 4.5).
The good agreement between the photocatalytic performances and the hydrophilic behavior was explained considering that the high hydrophilicity of the surfaces maximized the contact between stain and nano-TiO_2 active phase.

Table 4.5 Photocatalytic test: discoloration of (a) rhodamine B stain and (b) red wine stain. Experimental conditions: exposure time = (a) 30 min, (b) 24 hours.

Sample	pH	Photocatalytic efficiency %	
		(a) rhodamine B	(b) red wine
Pristine	-	49.2	37.5
TAC	1.5	84.6	46.8
TACF3.5	3.5	92.5	81.5
TACF4.0	4.0	94.7	95.2
TACF4.2	4.2	97.8	95.9
TN	6.0	68.7	57.2

Moreover, the presence of adsorbed water molecules, promoted by the hydrophilic feature, favoring the production of hydroxyl radicals, $^{\bullet}OH$, involved in the photocatalytic reaction mechanism.

Under UV irradiation, a total discoloration was achieved with the TACF4.0 and TACF4.2 samples, a partial discoloration was obtained with TAC, TACF3.5 and TN samples, whilst the pristine sample shows a visible stain, even if attenuated (Fig. 4.16). Similar results were obtained with the self-cleaning tests of red wine stain (Fig. 4.17). The expected efficiency increase, as starting pH increases, actually was not verified for the TN sample that showed a decreasing of efficiency percentage, with a value similar to that of TAC sample (Fig. 4.18a).

TN sample represented, also in this case, an exception. In fact, due to its different surface chemistry, despite its high starting pH value and its good acidity (low $pH_{i.e.p.}$) and hydrophilic behaviors (Fig. 4.18b), it exhibited a low photocatalytic activity, due to the detrimental effect on photocatalytic reactivity caused by the presence of the organic capping molecules [21].

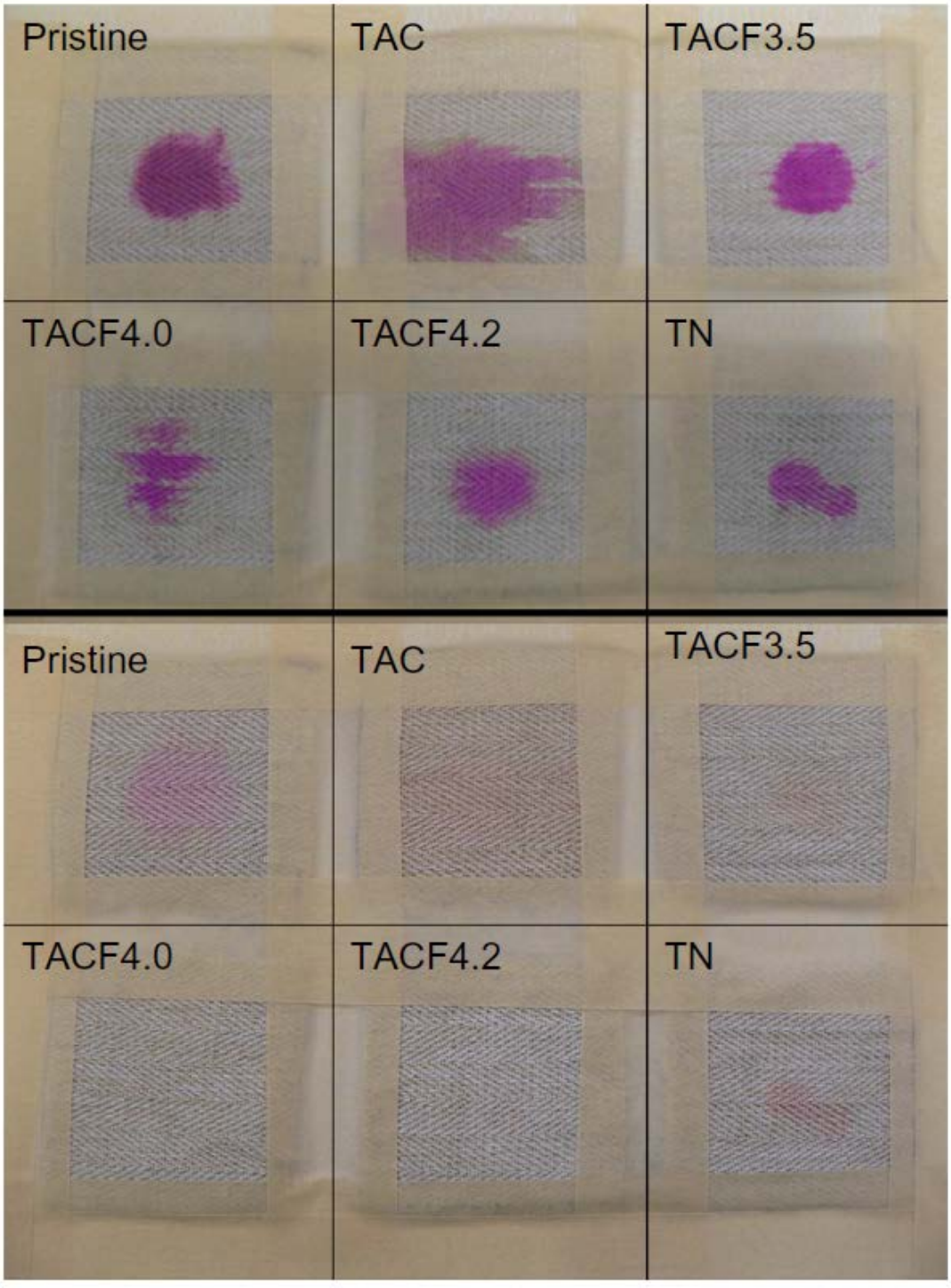

Figure 4.16 Rhodamine B stain discoloration on the fabric samples under UV irradiation. t = 0 (above) t = 30 min (below).

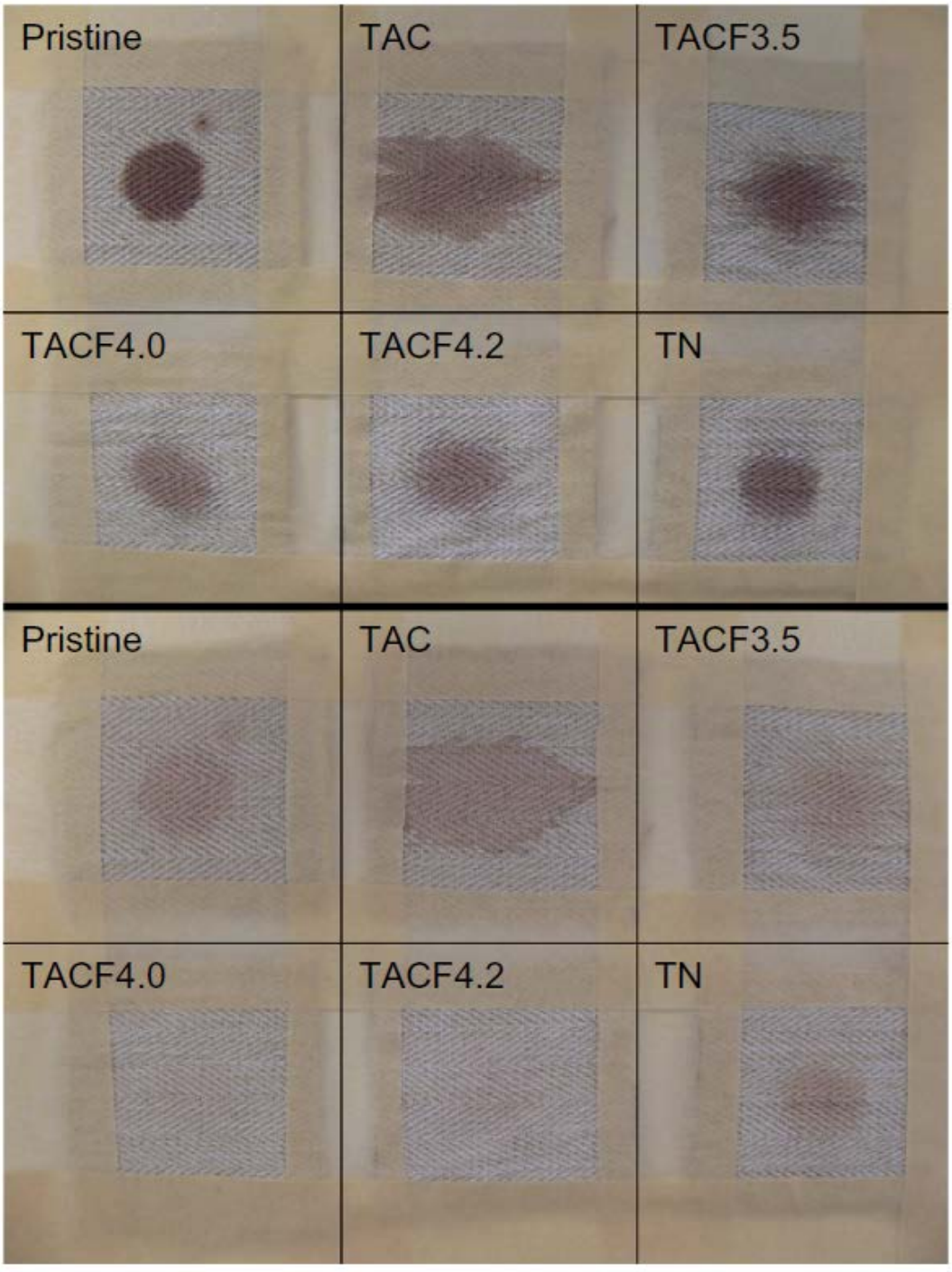

Figure 4.17 Red wine stain discoloration on the fabric samples under UV irradiation. t = 0 (above) t = 30 min (below).

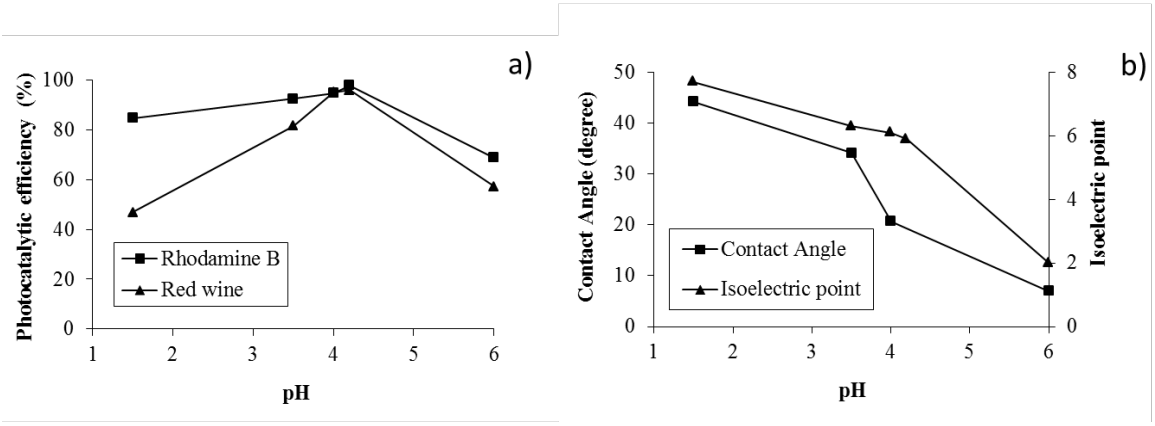

Figure 4.18 a) Photocatalytic efficiency as a function of pH and b) influence of pH on contact angle (measurements performed on glass support) and on $pH_{i.e.p.}$.

4.2.3 Photocatalytic results in different set-ups [22]

This Section mainly aims at exploiting the photocatalytic reactivity of nano-TiO_2 coatings immobilized on textiles. The efficiency in the photodegradation of organics, in our case organic dye (RhB – Fig. 4.19), was investigated in different experimental settings, inherent the self-cleaning application: TiO_2 nanoparticles in solution, TiO_2-coated textile dipped in solution and stain on TiO_2-coated textile. The different set-ups were selected in order to find suitable experimental conditions in which to perform photocatalytic tests inherent to the self-cleaning mechanism. With the aim to identify the factors affecting the photocatalytic reactivity, the photocalaytic behavior of three different TiO_2 nanosols (TAC, TACF4.0 and TN, partially already studied), in various experimental conditions, was compared with a reference material, TiO_2 P25 (Evonik).

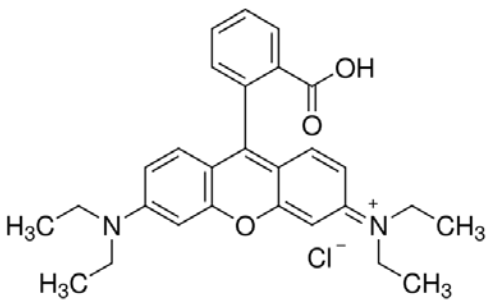

Figure 4.19 Molecular structure of Rhodamine B (RhB).

4.2.3.1 Summary of TiO_2 nanosols properties

The main characteristics (already reported in Section 4.2.2) of TiO_2 nanosol samples studied in this Section, were summarized in Table 4.6. With the exception of sample TN, the hydrodynamic diameter was influenced by starting pH, with an increasing of sizes at higher pH. Such behaviour was expected because TiO_2 NPs have a strong tendency to agglomerate once out of the very acidic region. The sample TN was an exception because it was supplied with dispersant agent in order to preserve the stability of nanosol at almost neutral pH and so to prevent agglomeration [23]. The SSA data were determined on spray-dried powder samples. The spray-drying process used to obtain the powder consisted in an instantaneous solvent evaporation of colloidal nanosol. So, this process was able to preserve the nanostructure in the spray-dried powders, as confirmed by the high values of SSA (Table 4.6).

Table 4.6 Physicochemical features of the TiO_2 nanosol samples.

	pH	d_{DLS} (nm)	PDI	SSA_{BET} ($m^2 g^{-1}$)	Contact Angle (°) ± Standard Deviation (σ)
TAC	1.5	46	0.25	237	44.2 ± 2.2
TACF4.0	4.0	96	0.35	190	20.7 ± 1.4
TN	6.0	44	0.27	36	7.0 ± 1.5

The hydrophilicity of TiO_2-coated supports was influenced by starting pH, as seen previously and as demonstrated by data reported in Table 4.6. Glass surfaces, in fact, showed a decrease in contact angles increasing starting pH of TiO_2 nanosol. Such a trend was justified by a larger amount of $Ti\text{-}O^-$ sites at higher pH, promoting the formation of hydrogen bonds with water and consequently an improved hydrophilicity.
The TiO_2 residual amount, after burn-out (evaluated by burn-out tests) was 3.0, 3.4, 2.9 and 3.4 wt% in the TAC, TACF4.0, TN and reference (P25) samples, respectively.

4.2.3.2 Photocatalytic results

The photocatalytic reactivity of nano-TiO_2 sols, tested in different experimental conditions was affected by the degree of freedom of the systems, that decreased from a)

TiO_2 in sol, to b) TiO_2-coated textile and c) Stain on TiO_2-coated textile. The different experimental set-ups were schematized in Figure 4.20. The TiO_2 reactivity depended in the case a) only on the surface chemistry, while in the cases b) and c) it was influenced by TiO_2/substrate and TiO_2/substrate/stain interactions, respectively. This implied that the photocatalytic performances of TiO_2-coated fabrics and stained TiO_2-coated textiles were not predictable just on the basis of the photocatalytic properties measured by TiO_2 in sol.

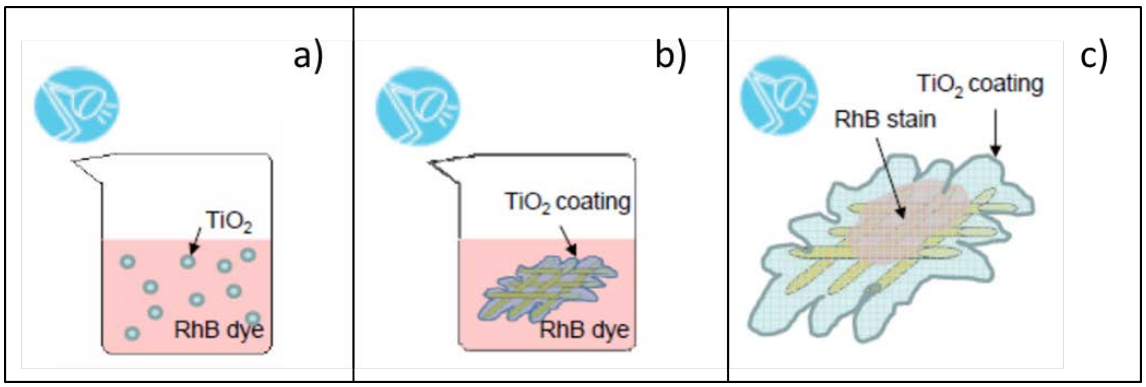

Figure 4.20 Schematic representation of a) Test in solution: TiO_2 sol, b) Test in solution: TiO_2 supported on textile and c) self-cleaning application: stain on TiO_2 coated textile.

The degradation of RhB, here used as model reaction, was promoted by radical species generated (Eqs. 4.9-4.11), as a consequence of UV irradiation [24].

$$\text{catalyst} + UV \rightarrow h^+ + e^- \qquad \text{(Eq. 4.9)}$$

$$e^- + O_2 \rightarrow {}^{\bullet}O_2^- \qquad \text{(Eq. 4.10)}$$

$$h^+ + OH^- \rightarrow {}^{\bullet}OH \qquad \text{(Eq. 4.11)}$$

The photodegradation reaction approximately obeys a pseudo-first-order kinetics and the reaction can be expressed by -dC/dt = kC, where C is the concentration of RhB and k is the apparent reaction rate constant. The degradation rate constants k, derived by

plotting ln (C_0/C) versus t and calculating the slopes of simulated straight lines, were reported in Figure 4.21 [25-27].

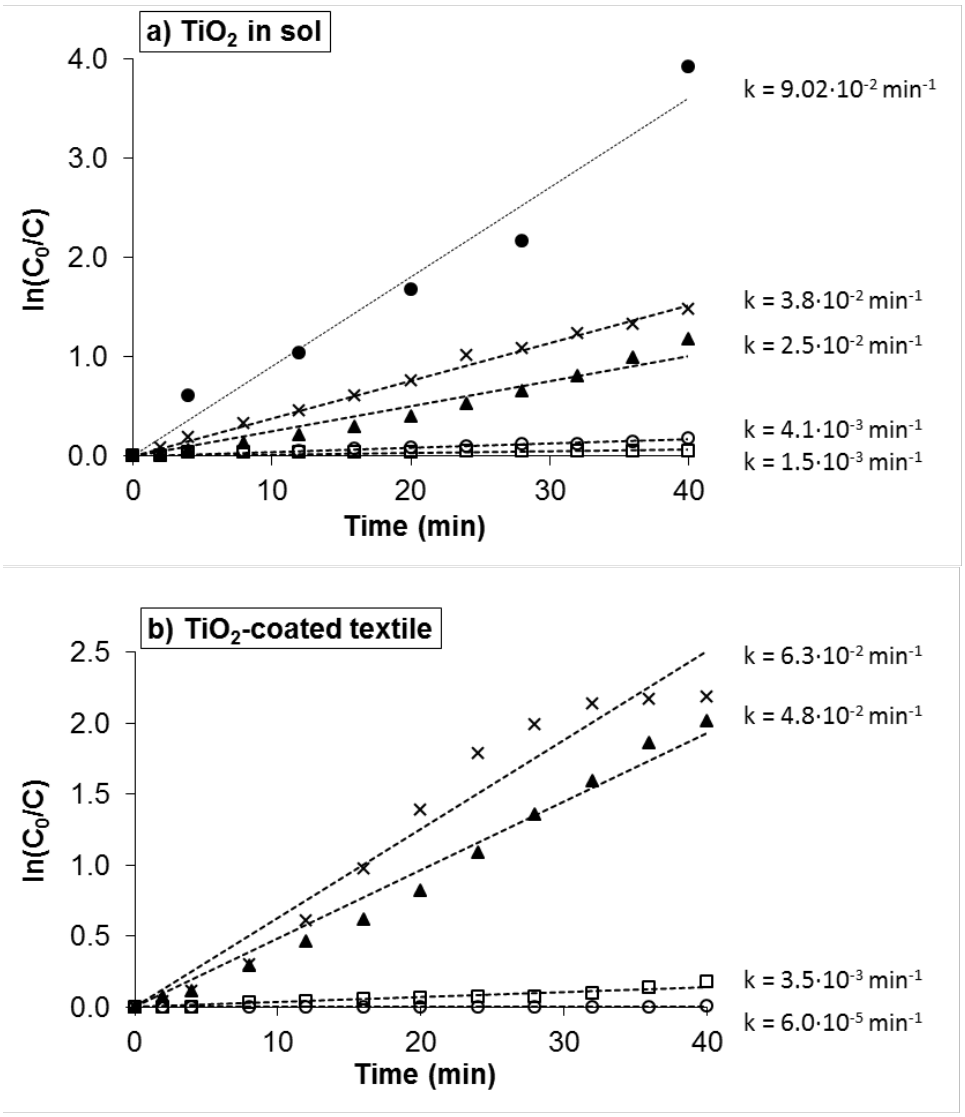

Figure 4.21 The kinetics of degradation and relative degradation rate constants k, after 40 min of UV-irradiation, in different conditions, of samples: ● P25 (reference material); x TAC; ▲ TACF4.0; □ TN and ○ Blank.

The values of degradation rate constants k calculated at 40 min showed higher efficiencies for TiO_2-coated textiles in comparison with TiO_2 nanosols. The explanation has to be searched in the two different Rhodamine B degradation mechanisms: the de-

ethylation process attributed to TiO_2-coated textiles, in fact, was reasonably more efficient at short time in comparison with the mechanism attributed to TiO_2 nanosols, that would lead to a complete RhB degradation.

The same trends were confirmed by photonic efficiency data (Table 4.7). Furthermore, the highest efficiency of reference material (TiO_2 P25) was observed. This can be explained by the absence of stabilizing agents and by-products, instead present in our TiO_2-nanosol samples and which could hinder the photocatalytic process.

Table 4.7 Photonic efficiency (ξ) for TAC, TACF4.0, TN and reference material (TiO_2 P25) samples after 40 min of UV irradiation.

	ξ (mol_{RhB} E^{-1}) TiO_2 in sol	ξ (mol_{RhB} E^{-1}) TiO_2-coated textile
TAC	8.95×10^{-3}	11.9×10^{-3}
TACF4.0	5.89×10^{-3}	15.6×10^{-3}
TN	0.97×10^{-3}	0.01×10^{-3}
TiO_2 P25	21.2×10^{-3}	-

The comparison between selected set-ups and different TiO_2 samples was highlighted in Figure 4.22.

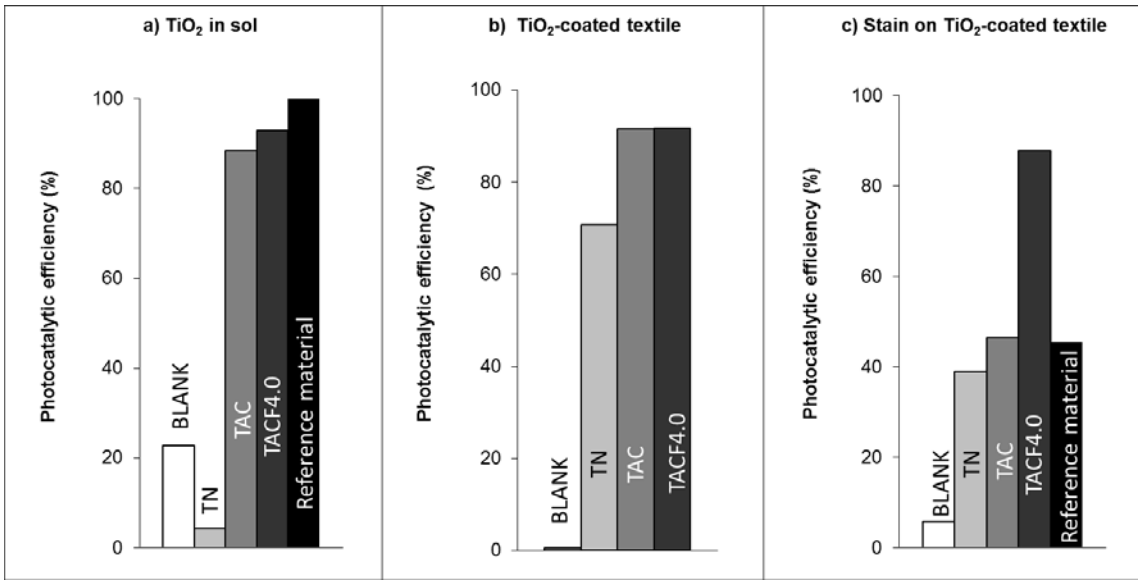

Figure 4.22 Photocatalytic efficiency (%), after 120 min of UV irradiation, in set-ups: a) TiO_2 in sol, b) TiO_2-coated textile and c) stain on TiO_2 coated textile.

According to the type of experimental set-up and TiO_2 photocatalyst, different trends of photocatalytic performance were found. In the case of TiO_2 in sol (a) (Fig. 4.22a), the low reactivity of sample TN can be explained by the presence of the organic coating that, surrounding the surface, could strongly interfere with the photocatalytic process and decrease the catalyst efficiency [28].

It was hypothesized that the sample TN was able to produce radicals but they were not available to decompose the dye because they are quenched by the organic coating which could chelate the TiO_2 NPs (Fig. 4.23).

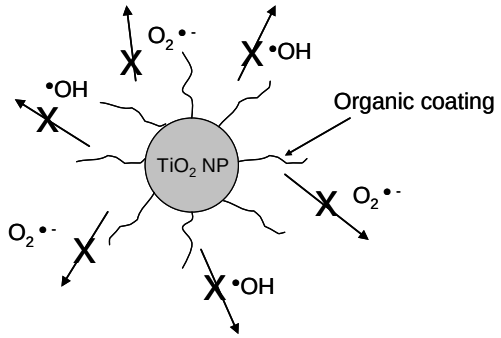

Figure 4.23 Schematic representation of radicals quenched by organic coating on TiO_2 NPs in TN sample.

On the opposite, the highest reactivity shown by the reference material can be justified considering that TiO_2 P25 powder is produced by a high temperature synthesis process, leading to a surface free from synthesis by-products.

Otherwise, TiO_2 nanosols were directly prepared via sol-gel synthesis and so different species may be adsorbed onto the NPs surfaces. Such effect was particularly evident in the case of set-up a), where the TiO_2 surface chemistry dominates the photocatalytic reactivity, as the catalyst was free to move throughout the test solution. TAC and TACF4.0 catalysts showed very similar, high photocatalytic efficiency percentages in tests in sol (a) and coated textile (b), whilst the TAC efficiency decreased in the case of stained fabrics (c). The results in tests in sol (a) and coated textile (b) were similar, apart from the sample TN. The high reactivity of sample TN in the set-up (b) (Fig. 4.22b) can be justified considering that the deposition on textile support lessens the interference

with the photocatalytic process caused by the presence of the dispersing agent that was maximized when the catalyst is free in solution (set-up (a)).

The difference between TAC and TACF4.0 reactivity, evidenced by results with set-up (c), can be justified by a different affinity for water showed by fabrics coated with the two catalysts, being the TACF4.0-coated sample much more hydrophilic than the TAC-coated one. In fact, the surface hydrophilicity/hydrophobicity of TiO_2-coated samples strongly affected the photocatalytic stain degradation, as demonstrated in Section 4.2.2. This process was improved by the presence of a high amount of water molecules adsorbed onto the surface (hydrophilic samples). This phenomenon was also confirmed by TiO_2 P25-coated samples behavior during the stain degradation. As a matter of fact, hydrophilicity seems the main parameter controlling the stain degradation efficiency (Fig. 4.22c).

In this Section, photocatalytic tests were carried out on RhB molecule for the easier interpretation of its degradation mechanism. A correlation between the photocatalytic degradation of red wine, a commonly used staining agent, and RhB on TiO_2-coated fabrics was found (Section 4.2.2.2).

However, as reported in the literature [29-32], the degradation of RhB using nano-TiO_2 as photocatalyst can occur in different pathways.

De-ethylation causes a blue-shift of the main absorption band of RhB, with consequent color variation of the solution from purple to yellow, whilst the complete degradation of the chromophore structure induces the achievement of colorless solutions [33,34].

In these studies, different degradation mechanisms of RhB, according to different photoreaction conditions, have been hypothesized by comparing the UV-vis spectra collected after 120 min of UV irradiation for the set-ups a) and b). These spectra can be interpreted as a function of different degradation mechanisms (Fig. 4.24). In the set-up TiO_2 in sol (a) the main adsorption peak of RhB (554 nm) decreased abruptly in the presence of TAC and TACF4.0 samples, due to a mechanism that led to a complete degradation of the chromophore structure (Fig. 4.24a).

A different behavior was shown by catalysts on textile (set-up b) where a RhB peak wavelength shift was detected (Fig. 4.24b). This was in agreement with the

photocatalytic reactivity trend previously commented (TACF4.0 > TAC > TN > without catalyst).

The wavelength shift was caused by de-ethylation of RhB under the attack of oxygenated radicals, produced during the photocatalytic process, towards *N*-ethyl group. De-ethylation of the fully *N,N,N',N'*-tetraethylated rhodamine molecule (i.e., RhB), in fact, caused a blue-shift of the main absorption band (from 554 to 498 nm) corresponding to fully de-ethylated rhodamine.

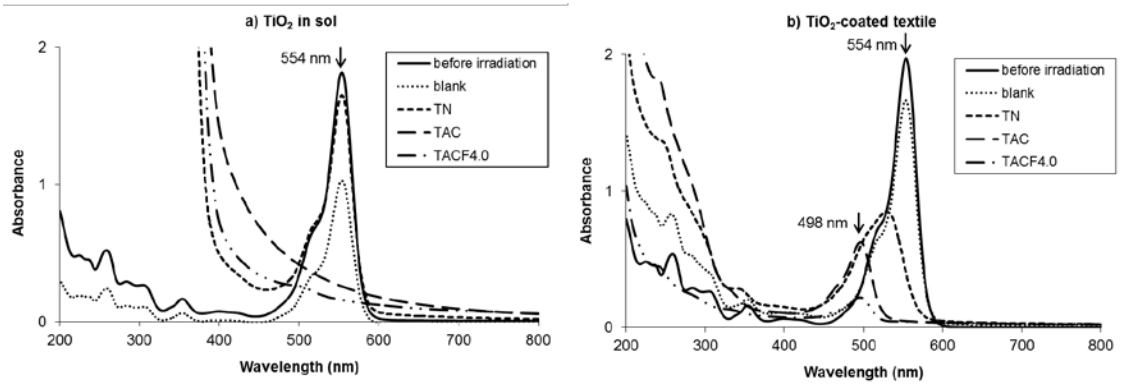

Figure 4.24 UV-vis spectra of RhB solution after 120 min of UV irradiation in set-up a) and b).

Such different photodegradation mechanisms, as detected by UV-vis analyses, were visually appreciable as Figure 4.25 clearly shows.

The occurrence of two distinct mechanisms for the degradation of RhB – outlined in Figure 4.26a (degradation of the chromophore structure) and Figure 4.26b (de-ethylation) – was justified by the different conditions of experimental set-ups.

a) TiO_2 in sol

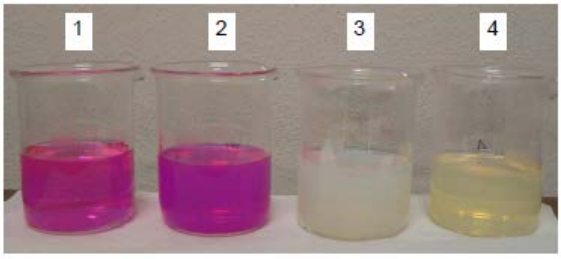

b) TiO_2-coated textile

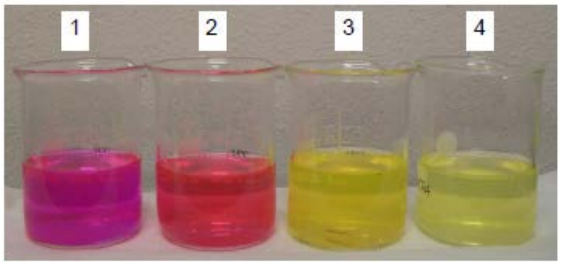

Figure 4.25 Photographs of samples: 1) blank; 2) TN; 3) TAC; 4) TACF4.0, after 120 min of UV-irradiation, in two set-ups: a) TiO_2 in sol and b) TiO_2-coated textile.

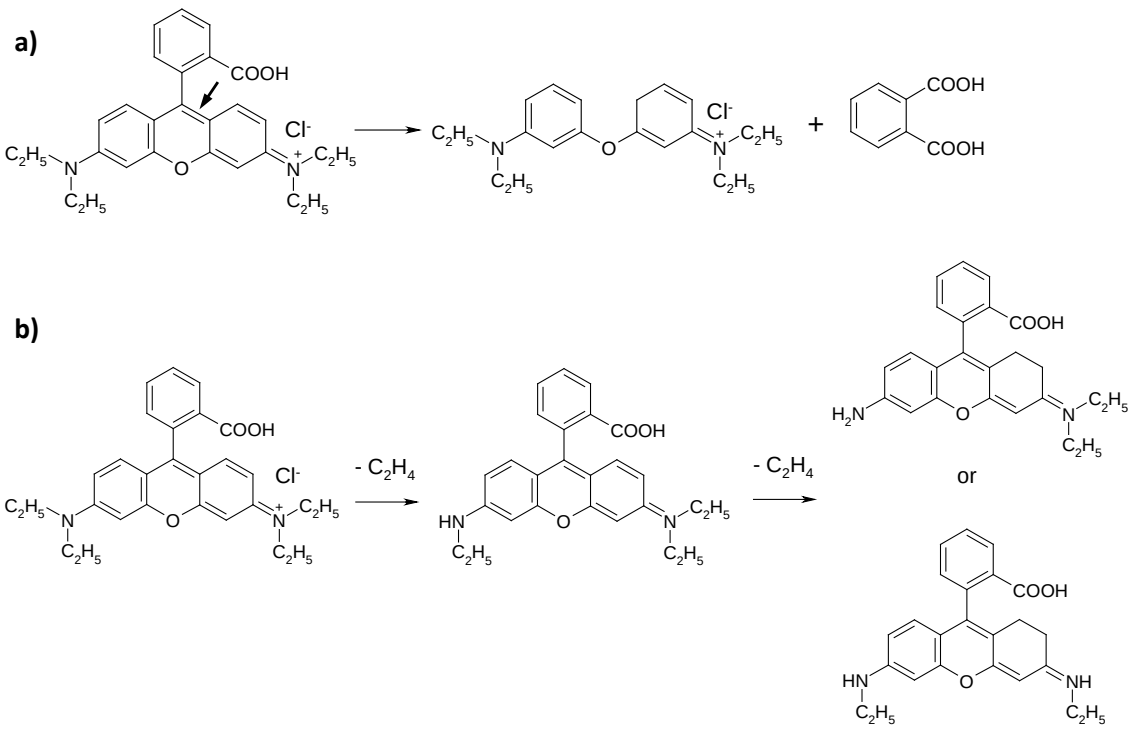

Figure 4.26 The proposed mechanisms for degradation of Rhodamine B: a) degradation of the chromophore structure and b) de-ethylation.

These tests, representative of different degrees of freedom of nano TiO_2 surfaces, were set up in order to mimic dye degradation mechanisms occurring in free catalysis (TiO_2 nanoparticles dispersed in dye solution), in heterogeneous catalysis (TiO_2-coated textile dipped in dye solution), and self-cleaning application (TiO_2-coated textile stained by dye). The results indicated that TiO_2 surface/dye interaction dominated when the catalyst is dispersed in the sol occurring a complete degradation driven by free radicals. In contrast, when the catalyst is supported on the fabrics, the TiO_2-coated substrate/dye interaction governs the process and de-ethylation, driven by radicals adsorbed onto the surface, is responsible for RhB degradation.

4.3 Conclusions

In conclusion, the physicochemical properties of different treated TiO_2 nanosols showed that a low conductivity and an high pH, corresponding to an high surface acidity allowed to obtain fabrics with high hydrophilic properties and better photocatalytic performance. On the evidence of the photocatalytic experimental results, the optimization studies showed that the purification through the by-products removal allowed a greater effect than neutralization treatment. Furthermore the purification by anion exchange resin process resulted the more effective. The easy process scalability and control of TiO_2 nanosols physicochemical properties (pH and conductivity) make the purification by anion exchange resin method very promising for the industrialization of self-cleaning textile.

Moreover, the deep investigation on relationship between TiO_2 based nanosols, nanocoatings properties and their performances in term of hydrophilicity and photocatalytic efficiency allowed to discover that the pH dependent aggregation state, was correlated to an increase of surface acidity as the shift of isoelectric point towards acid pH indicated. Such increase of acidity justified the detected increase of hydrophilicity, consequent to stronger interaction with water molecules, due to the expected higher amount of $Ti\text{-}O^-$ sites available. As well, the increase of hydrophilicity was correlated to the photocatalytic efficiency trend because of the expected improved

amount of $^{\bullet}OH$ radicals and the maximization of contact between stain and active phase.

Finally, a deep analysis of photocatalytic properties in different experimental conditions was performed. Photocatalytic tests, representative of different degrees of freedom of nano-TiO_2 surfaces, were set up in order to mimic dye degradation mechanisms occurring in free catalysis (TiO_2 nanoparticles dispersed in dye solution), in heterogeneous catalysis (TiO_2-coated textile dipped in dye solution), and self-cleaning application (TiO_2-coated textile stained by dye). A preliminary investigation let to make hypotheses on photodegradation mechanisms. In particular, TiO_2 surface/dye interaction dominating when the catalyst is dispersed in the sol caused the complete degradation of RhB, most probably driven by free $^{\bullet}OH$ radicals. In contrast, when the catalyst is supported on the fabrics, theTiO_2-coated substrate/dye interaction predominates and de-ethylation, driven by $^{\bullet}OH$ radicals adsorbed onto the surface, is responsible for step-by-step RhB degradation.

4.4 References

[1] S. Brunauer, P.H. Emmett, E. Teller, J. Am. Chem. Soc. 60 (1938) 309–319.

[2] S. Brunauer, L.S. Deming, W.E. Deming, E. Teller, J. Am. Chem. Soc. 62 (1940) 1723–1732.

[3] R. Apetrei, C. Catrinescu, D. Mardare, C.M. Teodorescu, D. Luca, Thin Solid Films 518 (2009) 1040–1043.

[4] K. Suttiponparnit, J. Jiang, M. Sahu, S. Suvachittanont, T. Charinpanitkul, P. Biswas, Nanoscale Res. Lett. 6 (2011) 27.

[5] I. Sameut Bouhaika, P. Leroya, P. Ollivier, M. Azaroual, L. Mercury, J. Colloid Interface Sci. 406 (2013) 75–85.

[6] L. Gai, X. Duan, H. Jiang, Q. Mei, G. Zhou, Y. Tiana, H. Liu, Cryst. Eng. Comm. 14 (2012) 7662–7671.

[7] A.L. Costa, C. Galassi, R. Greenwood, J. Colloid Interface Sci. 212 (1999) 350–356.

[8] B. He, Y. Ren, Y. Chen, J. Li, Energy Fuels 26 (2012) 3897−3902.

[9] P. Chularueangaksorn, S. Tanka, S. Fujii, C. Kunacheva, J. Appl. Polym. Sci. 130 (2013) 884–889.
[10] M. Di Girolamo, M. Marchionna, J. Mol. Catal. A: Chem. 177 (2001) 33–40.
[11] P. R. Levison, J. Chromatogr. B 790 (2003) 17–33.
[12] L. Dloczik, R. Koenenkamp, J. Solid State Eletrochem. 8 (2004) 142–146.
[13] O. Shinkazh, D. Kanani, M. Barth, M. Long, D. Hussain, A. L. Zydney, Biotechnol. Bioeng. 108 (2011) 582–591.
[14] A. Porat, D. Winters, L. Cai, S. Smith, F. Abroson, L.-T. Tony Tam, Z. Shen, R. Hecht, Prep. Biochem. Biotech. 42 (2012) 304–321.
[15] A.L. Costa, S. Ortelli, M. Blosi, S. Albonetti, A. Vaccari, M. Dondi, Chem. Eng. J. 225 (2013) 880–886.
[16] G.L. Messing, S.-C. Zhang, G.V. Jayanthi, J. Am. Ceram. Soc. 76 (1993) 2707–272.
[17] W.J. Walker, J.S. Reed, S.K. Verma, J. Am. Ceram. Soc. 82 (1999) 1711–1719.
[18] D. Pang, Y. Wang, X. Ma, F. Ouyang, Chem. Eng. J. 258 (2014) 43–50.
[19] X. Wang, J. C. Yu, P. Liu, X. Wang, W. Su, X. Fu, J. Photochem. Photobiol. A: Chem. 179 (2006) 339–347.
[20] V. Romito de Mendonça, C. Ribeiro, Appl. Catal. B: Environ. 105 (2011) 298–305.
[21] V. Bolis, C. Busco, M. Ciarletta, C. Distasi, J. Erriquez, I. Fenoglio, S. Livraghi, S. Morel, J. Colloid. Interface Sci. 369 (2012) 28–39.
[22] S. Ortelli, M. Blosi, S. Albonetti, A. Vaccari, M. Dondi, A.L. Costa, J. Photochem. Photobiol. A: Chem. 276 (2013) 58–64.
[23] Y. Sun, I. Zhitomirsky, Mater. Lett. 73 (2012) 190–193.
[24] X. Lin, T. Huang, F. Huang, W. Wang, J. Shi, J. Phys. Chem. B 110 (2006) 24629–24634.
[25] J.M. Herrmanna, H. Tahiri, Y. Ait-Ichou, G. Lassaletta, A.R. Gonzàlez-Elipe, A. Fernàndez, Appl. Catal. B: Environ. 13 (1997) 219–228.
[26] L. Song, S. Zhang, X. Wu, Q. Wei, Ultrason. Sonochem. 19 (2012) 1169–1173.
[27] X. Shen, J. Zhang, B. Tian, M. Anpo, J. Mater. Sci. 47 (2012) 5743–5751.

[28] S. Livraghi, I. Corazzari, M. C. Paganini, G. Ceccone, E. Giamello, B. Fubini, I. Fenoglio, Chem. Commun. 46, (2010) 8478–8480.
[29] C. Pan, J. Xu, Y. Chen, Y. Zhu, Appl. Catal. B: Environ. 115–116 (2012) 314–319.
[30] J. Zhuang, W. Dai, Q. Tian, Z. Li, L. Xie, J. Wang, P. Liu, X. Shi, D. Wang, Langmuir 26 (2010) 9686–9694.
[31] Y. Chen, R. Huang, D. Chen, Y. Wang, W. Liu, X. Li, Z. Li, ACS Appl. Mater. Interfaces 4 (2010) 2273–2279.
[32] T. Wu, G. Liu, J. Zhao, J. Phys. Chem. B 102 (1998) 5845–5851.
[33] A. Mehrdad, R. Hashemzadeh, J. Chem. Soc. Pak. 31 (2009) 738–743.
[34] E. Baldev, D. MubarakAli, A. Ilavarasi, D. Pandiaraj, K.A. Sheik Syed Ishack, N. Thajuddin, Colloid Surface B 105 (2013) 207– 214.

Chapter 5: “SAFETY BY DESIGN” APPROACH ON TiO_2 NANOPARTICLES

Within the European Project Sanowork (Safe Nano Worker Exposure Scenarios FP7-NMP4-SL-2011-280716), risk remediation strategies (RRSs), based on a “safety by molecular design” (Sbd) approach, were studied with the aim to prevent workers from exposure and/or potential hazards of nanomaterials. They were developed exploiting surface engineering processes such as:

1. particles coating with inert inorganic materials performed by heterocoagulation process or chemical synthesis;
2. particles coating with organic antioxidant molecules by a self-assembled monolayer mechanism;
3. micronization of nanoparticles keeping nanoscale reactive structures, performed by spray granulation or other processes useful to provide a controlled aggregation (for example, gelation, incorporation and impregnation on inorganic supports);
4. size control by wet milling of nanofibers in order to reduce their length and their aspect ratio;
5. purification performed in order to remove potentially toxicant agents.

In particular, commercial TiO_2 nanosol (TAC), used in manufacturing process for the production of photocatalytic nanostructured coatings on ceramic tiles, was studied. The process consists in the application of TiO_2 nanosols (TAC) on ceramic substrates through spray-coating method, which could cause nano-aereosolization and induce inhalation of NPs. A representative scheme of the processing line was shown in Figure 5.1. In the specific case of TiO_2 NPs, three risk remediation strategies were developed:

the introduction of organic and inorganic coatings and the micronization, aiming at decreasing both the potential toxicity and the emissivity of nanomaterials.

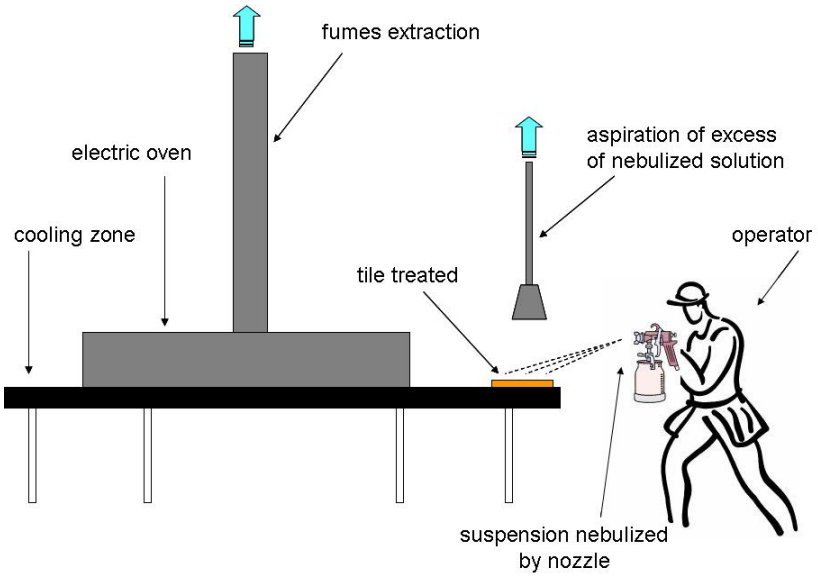

Figure 5.1 Schematization of processing line in which TiO_2 NPs-Colorobbia (TAC samples) are involved.

Silica was selected as inorganic coating thanks to its known chemical inertia [1], biocompatibility [2], low toxicity [3] and ability to create mesoporous structure [4], whilst citrate was used as organic coating due to its hydrophilicity and negative charge that lead to an increased dispersability in aqueous medium and a strong specific interaction with NPs hydroxyl groups, preventing the contact with negative charged cellular membrane [5-7]. Spray-drying was also introduced as "nano in micro" strategy (micronization) to manage the potential risk of nanomaterials.

In order to validate the introduction of RRSs, biological and photocatalytic performance evaluation were performed. The biological analysis mainly aimed to assess and compare the toxicity of pristine and modified samples, before and after the introduction of RRSs. Whilst the photocatalytic performance evaluations, which included photocatalytic tests on nanosols and NO_x/NO abatement analysis on coated ceramic tiles, were used to verify that functional properties (photoactivity) of TiO_2 were preserved after the introduction of risk remediation strategy.

Due to the interesting results shown in performance evaluation,TiO_2/SiO_2 systems were further investigated. Considering, the difficulty and the complexity in understanding the photocatalytic mechanism, a study inherent the reactive oxygen species (ROS) production, was made. In the specific, it is believed that the self-cleaning properties originate from the photocatalysis of oxygenated molecules, but the mechanisms acting on textiles, and particularly the phenomena occurring at the interface, in which free radicals are involved, are not yet fully understood. Thus, a study about the comparison of three analytical methods to assess the production of reactive oxygen species (ROS), free radicals driving the photoreactivity of TiO_2 incorporated in textiles, was made. In the specific, TiO_2 samples were modified by silica in varying amounts to get TiO_2/SiO_2 systems, that were applied onto textiles, as self-cleaning textiles.

5.1 Experimental Section

5.1.1 Materials

TiO_2 nanosol (NAMA41, 6 wt%) called TAC, was purchased by Colorobbia (Italy). SiO_2 nanosol (Ludox HS-40® 40 wt%), called SiO_2SOL was purchased by Grace Davison (USA). TiO_2 nanopowder P25, used as benchmark material, was purchased by Evonik. Rhodamine B (dye content ~ 95%) used as target dye, cationic exchange resin Dowex® 55X8, trisodium citrate dehydrate, hexaaminoruthenium (III) chloride, 2,3-di-hydroxybenzoic acid, salicylic acid (ReagentPlus) were purchased by Sigma Aldrich. Potassium di-hydrogen phosphate and 2,5-di-hydroxybenzoic acid were obtained from Fluka. Sodium acetate was purchased from Carlo Erba. Acetic acid, NaOH, H_2SO_4 and sodium azide were purchased from Baker. Textile fabrics used for NPs incorporation and photocatalytic tests were polycottons, exploited for soft furnishings, with specific weight of 360 g/m^2 and composition: 62% cotton - 38% polyester.

5.1.2 Preparation of modified TiO_2 nanoparticles

Inorganic and organic coatings were applied on TiO_2 NPs (TAC) by heterocoagulation method [8-10] and self-assembled monolayer (SAM) formation [11], respectively.

The TiO_2/SiO_2 sample was obtained through an electrostatic interaction between negatively charged silica nanoparticles (SiO_2SOL) and positively charged titania nanoparticles (TAC). The commercial nanosols were diluted with water and in the case of SiO_2SOL, it was acidified by cationic exchange on resin till pH 4. After such treatments, the titania and silica nanosols were mixed in well-defined ratio (TiO_2:SiO_2 weight ratios 1:3) and ball milled for 24 hours with zirconia spheres as milling media. The sample was prepared with a TiO_2 content equal to 3 wt %. Citrate coated TiO_2 NPs were prepared adding trisodium citrate dihydrate (powder) to TAC sample with TiO_2:Cit weight ratio 1:0.83, with a TiO_2 concentration of 3 wt%. The mechanical stirring process for 15 h was applied, to favor the redispersion of TiO_2 NPs. The resulting inorganic- and organic-coated samples were called TiO_2:SiO_2 and TiO_2CIT, respectively.

In the end, the TAC sample was spray-dried in counterflow with a stream of hot air (at 220 °C) through a nozzle of 500 μm of diameter using Spray-dryer SD-05, Lab-Plant Ltd., Huddersfield, (England), schematized in Figure 5.2, producing nanostructured micropower (TiO_2SD).

The TiO_2 nanopowder P25 (Evonik) was used as reference material.

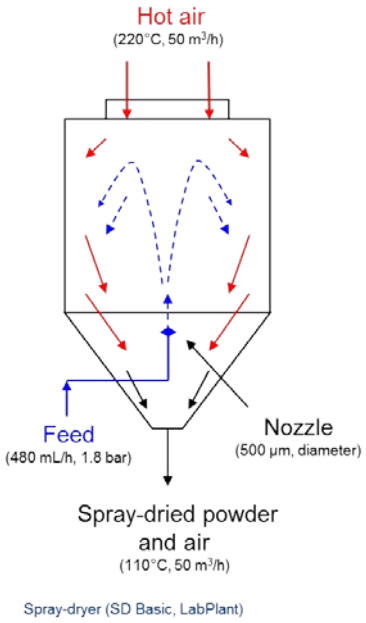

Figure 5.2 Schematic representation of spray-dryer.

5.1.3 Characterization of modified TiO_2 nanoparticles

Pristine (TAC) and modified (TiO_2:SiO_2 and TiO_2CIT) nanosol samples were characterized by dynamic light scattering (DLS) and electrophoretic light scattering (ELS) techniques, through Zetasizer Nanoseries (Malvern Instruments, UK), to determine NPs hydrodynamic diameter and ζ potential, respectively. The details of two techniques were reported in Section 4.1.4. A morphological characterization was performed by two sophisticated techniques: TEM (Transmission Electron Microscopy) and FE-SEM (Field Emission-Scanning Electron Microscopy). The TEM analyses on TAC and TiO_2:SiO_2 nanosol samples were performed at Advanced Microscopy Laboratory (AML), CRANN, Trinity College Dublin (TCD) by a FEI Titan TEM operating at an acceleration voltage of 300kV, whilst FE-SEM analyses on TiO_2SD sample were carried out by FE-SEM (Carl Zeiss Sigma NTS Gmbh Öberkochen, Germany). The specific surface area (SSA) measurement on TiO_2SD sample was determined by Brunauer-Emmett-Teller (BET) method (seen Section 4.1.4).

5.1.4 Biological tests

Biological *in vitro* tests were carried out in to determine cellular responses to the pristine and surface modified TiO_2 NPs.

Cellular toxicity tests were performed to assess alteration in cell viability induced by the TiO_2 NP samples using A549 alveolar epithelial cells.

Treatment of cells and subsequent analysis was carried out at three different time points for at least two times, so as to obtain reproducible values.

The ability of nanomaterials to interfere with the assay was tested using a cellular preparation as well as spiking and recovery of the analyte as nanomaterials could adsorb and/or inhibit the enzyme activity and as such, bias the results obtained. In particular, cytostasis (CBPI and RI) and cytotoxicity (apoptotic and necrotic indices) were evaluated by CBMN cyt assay and the haemolytic activity was measured incubating TiO_2 NPs in red blood cells.

5.1.5 Performance evaluation

In order to evaluate the functional properties of TiO_2 NPs, before and after the introduction of RRSs, photocatalytic tests in sol and NO_x/NO abatement tests on coated ceramic tiles were performed.

5.1.5.1 Photocatalytic tests

The photocatalytic reactivity of pristine sample (TAC) and modified samples (TiO_2:SiO_2, TiO_2CIT and TiO_2SD) was evaluated using as a model reaction the degradation of the RhB. The aim of performance test was to assess if the introduction of RRSs: SiO_2 and citrate coating (inorganic and organic coating, respectively) and spray-drying process involved a negligible change of the functional properties of NMs, so validating the introduction of the modifications.

Photocatalytic degradation of RhB was conducted in a beaker at room temperature, with the same experimental set-up described in Section 4.1.7.1 (TiO_2 in sol (a)). In particular, 2.5 ml of RhB aqueous solution (0.07 g/L) were added to 22.5 mL of TiO_2 nanosol (TAC, TiO_2:SiO_2 or TiO_2CIT) or 22.5 mL of water containing 0.75 g TiO_2SD or 22.5 mL of only water (blank). In order to compare the results, in all the tests, the active phase, TiO_2, content was 3 wt%.

The TiO_2 based sol was stirred and irradiated with UV radiation (Osram ULTRA-Vitalux lamp). The photocatalytic efficiency was determined by formula (Eq. 4.3). The details of photocatalytic tests were reported in Section 4.1.7.1.

5.1.5.2 NO_x/NO abatement tests

The test inherent to the determination of reduction degree of NO_x/NO was carried out on pristine (TAC) and modified (TiO_2:SiO_2 and TiO_2CIT) samples. In particular, the analyses were performed in actual conditions of use of our TiO_2 target NMs, so pristine (TAC) and modified (TiO_2:SiO_2 and TiO_2CIT) nanosols with TiO_2 content of 1 wt% (5 g) were applied on ceramic tiles (20x20 cm) by spry-gun. The coated ceramic tiles were obtained after thermal treatment at 700°C for 1h, with a heating rate of 350°C/h. The analyses were made in controlled conditions: Temperature = 23 ± 2°C and relative humidity = 40 ± 2% and under UV irradiation with intensity of 50 W/m^2 and an

illumination wavelength range of 300-400 nm (Osram ULTRA-Vitalux lamp 300 W). The analyses were performed, injecting in the measuring system pollutant gas consisting of dry air, moist air and NO, in presence of ceramic tiles. The gases concentration (NO, NO_x and NO_2) was monitored by chemiluminescent detector (Thermo, model 42i), evaluating the NO_x/NO abatement given by the TiO_2 based coating on ceramic tiles.

5.1.6 Study on TiO_2:SiO_2 samples

5.1.6.1 Preparation and characterization of TiO_2:SiO_2 samples

TiO_2:SiO_2 samples were prepared by heterocoagulation method, exploiting electrostatic interaction between negatively charged silica nanoparticles and positively charged titania NPs. The procedure used was the same for modified TiO_2 NPs samples, described in detail in Section 5.1.2. The following TiO_2:SiO_2 weight ratios 1:0.3, 1:3 and 1:5 were investigated, obtaining the TiO_2:SiO_2 1:0.3, TiO_2:SiO_2 1:3 and TiO_2:SiO_2 1:5 samples, respectively. All TiO_2/SiO_2 systems were prepared with a TiO_2 content equal to 3 wt%.

The nanosol samples were characterized by dynamic light scattering (DLS) to determine NPs hydrodynamic diameters and electrophoretic light scattering (ELS) techniques, for ζ potential determination and titration measurements. The details of two techniques were reported in Section 4.1.4. The determination of chemical composition of TiO_2:SiO_2 samples was performed by XRF (WDS - wavelength dispersive X-ray spectrometer) using a Panalytical Axios Advanced (Netherlands). The measurements were carried out on TiO_2 nanosol and samples with TiO_2:SiO_2 weight ratios 1:3 and 1:5. The morphological characterization on TiO_2:SiO_2 1:3 and TiO_2:SiO_2 1:5 nanosol samples was performed by TEM analyses (seen Section 5.1.3).

5.1.6.2 Hydrophilicity measurements by adsorption microcalorimetry

In order to evaluate the effect of SiO_2 on hydrophilicity TiO_2, a sophisticated technique, the adsorption microcalorimetry was used. It was carried out on pure SiO_2, pure TiO_2 and TiO_2/SiO_2 systems (with TiO_2:SiO_2 ratios 1:3 and 1:5) in the form of powder, obtained by spray-drying technique (Fig. 5.2).

Hydrophilic properties (amount and enthalpy changes associated with the adsorption of H_2O vapour) of the investigated samples were measured at T = 303 K by means of a heat-flow microcalorimeter (Calvet C80, Setaram, France) connected to a high vacuum gas volumetric glass apparatus. A well-established stepwise procedure [12] was followed to simultaneous determination of both the adsorbed amount and the integral heat of adsorption, which evolved as a function of the increasing equilibrium water vapor pressure. The equilibrium pressure ($p_{eq}(H_2O)$) was monitored by a transducer gauge (Ceramicell0–100 Torr, Varian). Volumetric isotherms reported H_2O adsorbed amounts, normalized to the unit surface area (n_{ads}, μmol/m^2), as a function of increasing H_2O equilibrium pressure. Calorimetric outputs, were processed as differential heats of adsorption, $Q^{diff} = -\Delta_{ads}H$ (kJ/mol) as a function of the increasing water uptake (n_{ads}, μmol/m^2) [12]. Before the adsorption experiments, all samples were out gassed for 2 h at T = 423 K (residual pressure p ~ 10^{-5} Torr) in order to remove the physisorbed contaminants. After the thermal treatment, avoiding the exposure to atmosphere, samples were inserted in the calorimeter at 303 K and outgassed overnight at 303 K to reach the equilibrium. The reversibility/irreversibility of H_2O adsorption was investigated through adsorption–desorption–adsorption measurements; after the first run of adsorption (ads. I), each sample was out gassed overnight (residual pressure p ~ 10^{-5} Torr) at the adsorption temperature, and a subsequent second run of adsorption (ads. II) was performed. The experimental uncertainly in quantitative data was lower than 5% [13].

The results of adsorption microcalorimetry were obtained, normalizing to SSA values of spray-dried samples, measured by Brunauer-Emmett-Teller (BET) method (seen Section 4.1.4).

5.1.6.3 Determination of free radicals

The study about the production of free radicals in samples based on nano-TiO_2, TiO_2:SiO_2 samples, was faced. In particular three different experimental protocols were employed: a recently developed electrochemical technique to determine hydroxyl radicals (•OH) and two well-known methods, namely trapping of •OH radicals by

salicylic acid and degradation of Rhodamine B. A comparative analysis between the results obtained by three methods was made in order to improve the knowledge of the photocatalytic mechanism in which free radicals are involved.

Trapping method with salicylic acid

The traditional scavenging or trapping method for an indirect quantification of free radicals was described. It uses salicylic acid (SA) as a trapping agent for free •OH radicals. Salicylic acid reacts with hydroxyl radicals to produce stable products, namely 2,3-DHBA (2,3-dihydroxybenzoicacid), 2,5-DHBA (2,5-dihydroxybenzoic acid) which can be easily determined by high performance liquid chromatography (HPLC) [14-17]. In our case, a suspension of NPs containing 5×10^{-5} M SA was UV irradiated with intensity of 9 W/cm^2 (Osram ULTRA-Vitalux lamp) in quartz cuvette for 10 min, in the same condition as reported in Section 4.1.7.1. The reaction between SA and •OH radicals was followed by HPLC (Merck Hitachi L-6200 A Intelligent Pump equipped with a Phenomenex Lichosphere 5 RP-18e column) via fluorimetric detection (Waters 474 Scanning Fluorescence Detector; λ_{exc}= 320 nm; λ_{em}= 440 nm) analyzing a small aliquot (1 mL) of the suspensions after 0, 1, 3, 5 and 10 min of UV irradiation.

The samples were diluted 1:3 with 0.1 M phosphate buffer solution (pH 7.0) to induce the TiO_2 nanoparticles coagulation and filtered through a nylon filter (pore size 0.45 μm). Then the solutions were injected into the liquid chromatograph equipped with a 200 μL loop. The mobile phase was methanol/water solution (10:90, V/V) buffered at pH 3.5. The composition of the aqueous solution was: 50 mM acetate and 10 mM citrate buffers and 0.02% (w/V) sodium azide. The chromatogram showed a good separation among the peaks of SA, 2,3-DBHA and 2,5-DBHA which were formed by the reaction between the •OH radicals and SA. The sum of the concentrations of 2,5-DBHA and 2,3-DBHA reflects the total •OH amount generated. Catechol, that is another possible product of SA aromatic hydroxylation, although detectable by the analytical system, is not usually observed when the •OH radicals produced by TiO_2 catalyst [18]. The trends of the concentrations of the di-hydroxy benzoic acid isomers versus time showed a typical behavior of the reaction scheme involving consecutive reactions.

Therefore, the data relevant to 1 min irradiation were used because longer times led to a consume of 2,5-DBHA and 2,3-DBHA following their reaction with the •OH radicals. Consequently, if the •OH production rates were calculated from the concentrations measured at times longer than 1 min, they would be underestimated. The yields of 2,5-DBHA and 2,3-DBHA production ($y_{2,xDBHA}$) were calculated from the amount of converted SA according to the formula:

$$y_{2,x\,DBHA}(\%) = \frac{\dot{n}_{2,x\,DBHA}}{\dot{n}_{SA}} \qquad \text{(Eq. 5.1)}$$

where $\dot{n}_{2,x\,DBHA}$ and $\dot{n}_{SA}$ stand for moles of produced 2,x DBHA and of consumed SA, respectively. The SA concentration decreased during all experiments that used photocatalysts based on TiO_2 and reached a value of about10 μM at the end of the irradiation.

Electrochemical method

The electrochemical method exploits a glassy carbon (GC) electrode modified with an insulating film of polyphenol which has been recently proposed as an electrochemical sensor for •OH determination [19].The basic principle is the evaluation of the amount of modifier destroyed by the •OH radicals, by means of the signal generated by a redox couple. Furthermore, by using this •OH sensor the problems related to the formation of complexes between TiO_2 nanoparticles and salicylic acid are overcome [20]. All the electrochemical experiments were carried out in a single compartment three-electrode cell. All potentials were measured with respect to an aqueous saturated calomel electrode (SCE). A Pt wire was used as the counter electrode. A 3 mm glassy carbon, purchased from Metrohm, was used as the working electrode.

The experiments were carried out using a CHInstruments Mod. 660C potentiostat controlled by a personal computer via CHInstruments software. Prior to each experiment, the GC electrode was cleaned first with sand-paper and then with aqueous alumina (0.05 m) slurry on a wet polishing cloth to remove all residues of old films and

to regenerate the mirror-like surface. Then the $Ru(NH_3)_6^{3+}$ signal was recorded by chronoamperometry (CA) or cyclic voltammetry (CV). The electropolymerization of phenol was carried out by applying a potential of +1.0 V to the GC electrode soaked in a solution containing 0.05 M phenol in 1 M sulfuric acid, for 60 s. Then the film was stabilized by five cycles of potential between 0 and + 0.8 V. Owing to their high reactivity, the •OH radicals coming in contact with the polyphenol film can attack the polymer causing its degradation.

As a result, the GC surface becomes partially uncovered. The modified GC electrode was soaked in a suspension of NPs which was irradiated for 15 min. After the exposition to the •OH radical generated by the NPs, the electrode was taken out of the solution, washed and the uncovered area was evaluated by CA using the charge exchanged by the $Ru(NH_3)_6^{3+}/Ru(NH_3)_6^{2+}$ couple [19]. The uncovered area is directly proportional to the •OH radicals which reach the electrode surface and the recorded current signals were used to evaluate the photocatalyst activity. The relative scale of •OH production rates was built using the values of the polyphenol degradation percentage obtained from CA responses for all the experiments.

Photdegradion of RhB in self-cleaning application

The third experimental protocol for evaluating the free radicals production measures the photocatalytic reactivity exploited for textile self-cleaning application.

In this case the photoactivity of samples was assessed as coating onto textile supports. TiO_2:SiO_2 nanosol samples were applied on textile support by dip-padding-curing method, described in detail in Section 4.1.5 and shown in Figure 4.1.

The free radicals production, involved in self-cleaning application, was determined by photocatalytic tests on TiO_2:SiO_2-coated textiles, following the procedure described in Section 4.1.7.3, related to set-up c): "Stain on TiO_2-coated textile".

5.2 Results and discussion

5.2.1 Characteristics of modified TiO_2 nanoparticles

A physicochemical characterization of modified samples was performed, in particular, with the purpose of making a comparison with pristine nanosol, TAC. The results were reported in Table 5.1. The increase of hydrodynamic diameter in TiO_2:SiO_2 sample was caused by both the steric hindrance of SiO_2 heterocoagulated on the TiO_2 surface [21,22] and the consequent electrostatic destabilization due to the neutralization of TiO_2 surface, adding SiO_2SOL. The likely destabilization was confirmed by the PDI data (0.35) that indicated the presence of not completely monodispersed NPs.

Table 5.1 Physicochemical characteristics of TiO_2 pristine (TAC) and modified materials.

Sample	pH	d_{DLS} (nm)	PDI	ζ potential (mV)
TAC	1.5	36	0.25	+38
TiO_2:SiO_2	2.2	396	0.35	+31
TiO_2CIT	6.0	64	0.27	-38
TiO_2SD	-	~9400[a]	-	-

[a] determined by FE-SEM analysis

Visual observations on TiO_2CIT sample, made during its preparation, pointed out the formation of some agglomerates, but after 15 h stirring the suspension turned whitish, switching back transparent.

The DLS results confirmed the well and complete redispersion of TiO_2 NPs in which the presence of citrate contributed, behaving as dispersant agent. In fact the size and relative PDI of TiO_2CIT sample were comparable with TAC nanosol.

The size of TiO_2SD was not determined by DLS due to the presence of micrometric particles, but was estimated by FE-SEM analysis. The mean diameter resulted about 9μm. The high value of SSA, about 230 m^2 g^{-1}, measured by BET, confirmed the nanostructure preservation, despite the micrometric size of powder.

The ζ potential results showed that the SiO_2SOL addition slightly decreased the ζ potential value in TiO_2:SiO_2 sample, whilst the negative ζ potential (-38 mV) in TiO_2CIT sample was in agree with the presence of negative citrate coating.

A morphological characterization, on TiO_2:SiO_2 and TiO_2CIT samples, was performed. The TEM analysis showed that the sample TiO_2:SiO_2 was constituted by a SiO_2 matrix where the very small TiO_2 NPs (d_{TEM} = 5 nm – Fig. 5.3a) were encapsulated. So a well definite and compact SiO_2 coating around TiO_2 NPs was not formed. However, it was observed a reciprocal interaction between the two phases (Fig. 5.3b).

Furthermore, it was confirmed by EDX analysis (Fig. 5.4) that TiO_2 and SiO_2 did not appear as separate phases.

At last, the FE-SEM analysis, performed on TiO_2SD sample, showed the presence of spherical and micrometric particles, as expected carrying out the spray-drying process, and so confirmed the preservation of primary nanostructure, as demonstrated in Figure 5.5.

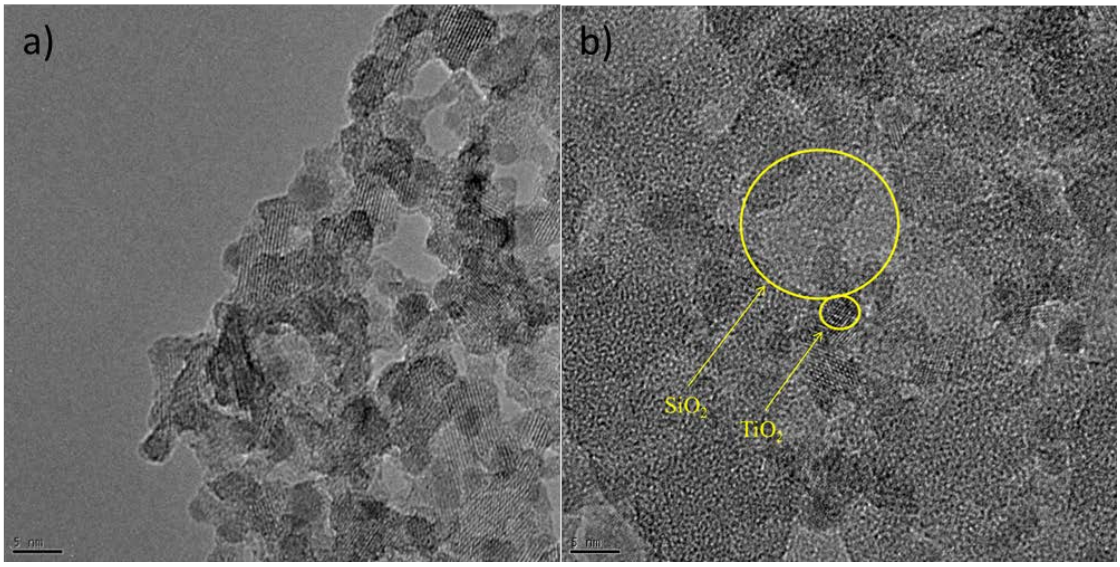

Figure 5.3 TEM imagine of a) TiO_2 NPs (TAC sample) and b) mixed TiO_2 and SiO_2 nanophases in TiO_2:SiO_2 sample.

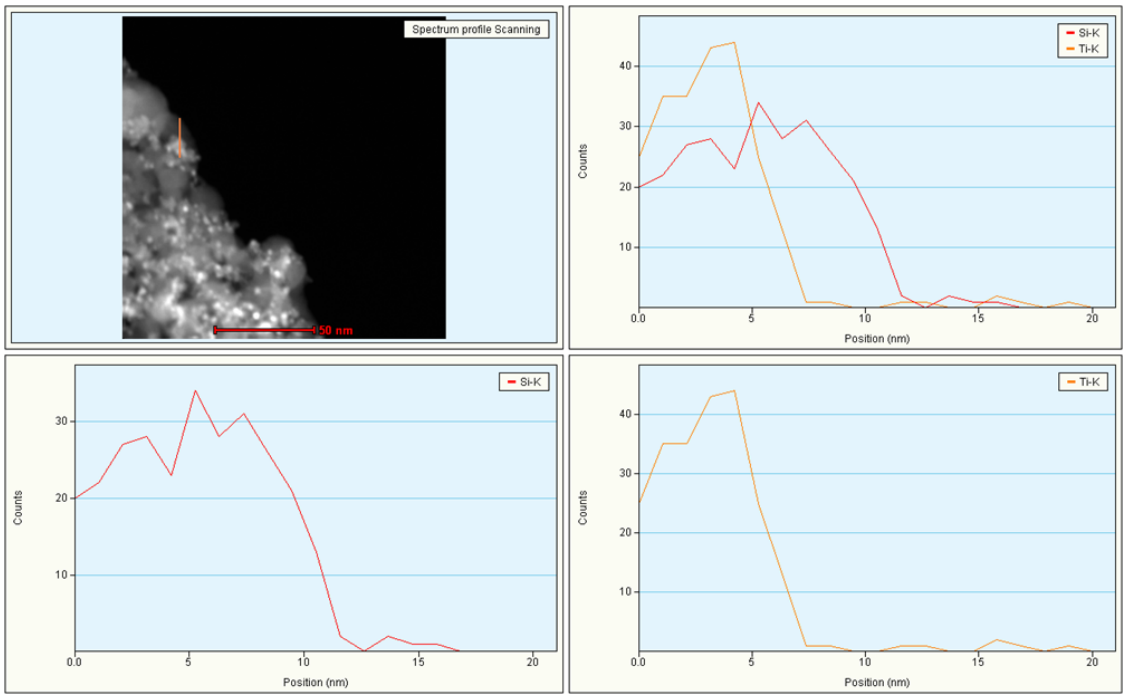

Figure 5.4 EDX-STEM analysis on TiO_2:SiO_2 sample.

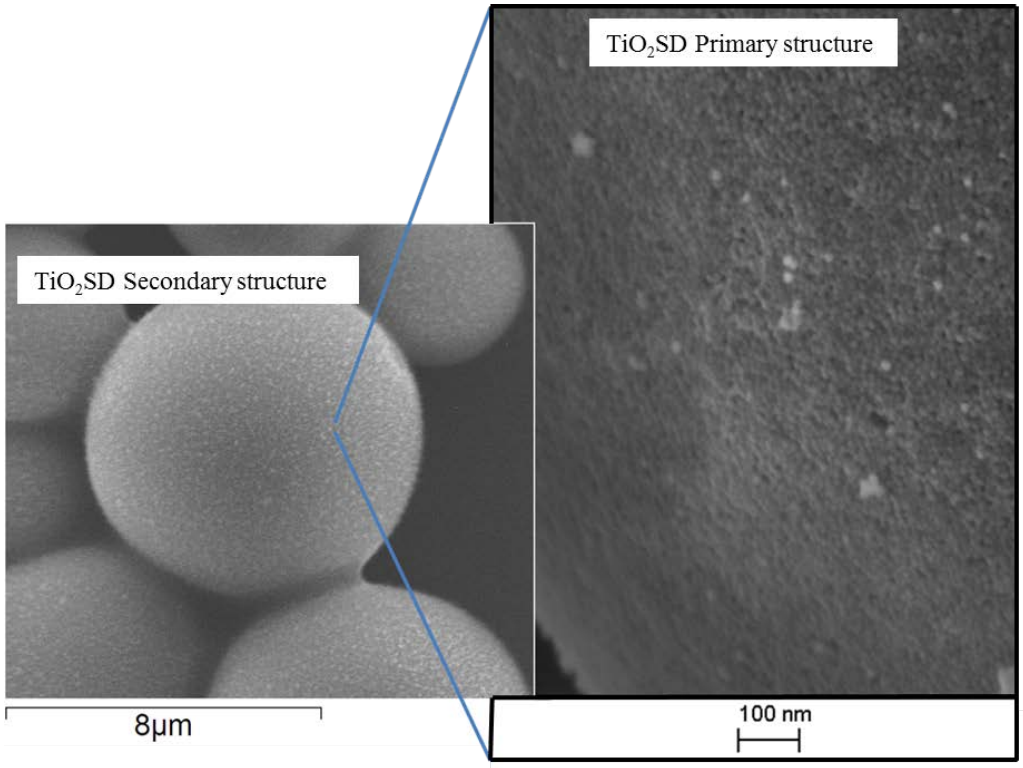

Figure 5.5 FE-SEM imagines of micrometric secondary structure and nanometric primary structure of spray-dried sample (TiO_2SD).

5.2.2 Biological results

In order to assess the performance and the validity of proposed risk remediation strategies the toxicological hazard assessment was carried out with the aim to:

1. identify the hazardous properties of nanomaterial, in our case TiO_2 NPs;
2. evaluate the impact of pristine and surface modified TiO_2 NPs by using *in vitro* models representative of exposure pathways;
3. determine how the cellular bio-reactivity of TiO_2 NPs relates to their physicochemical properties and give indications for the development of a safe and sustainable manufacturing of nanoproducts.

The biological tests were carried out using as reference material, TiO_2 P25 (Evonik). So, cellular toxicity was determined on P25 and TiO_2 samples (pristine, TAC and modified TiO_2:SiO_2, TiO_2CIT and TiO_2SD) by CBMN cyt assay in A549 cells. CBMN cyt assay indicated a reduction in CBPI and RI in A549 exposed to TiO_2 P25 (Evonik) and the cytostasis was highly statistically significant ($p<0.001$), as shown in Figure 5.6.

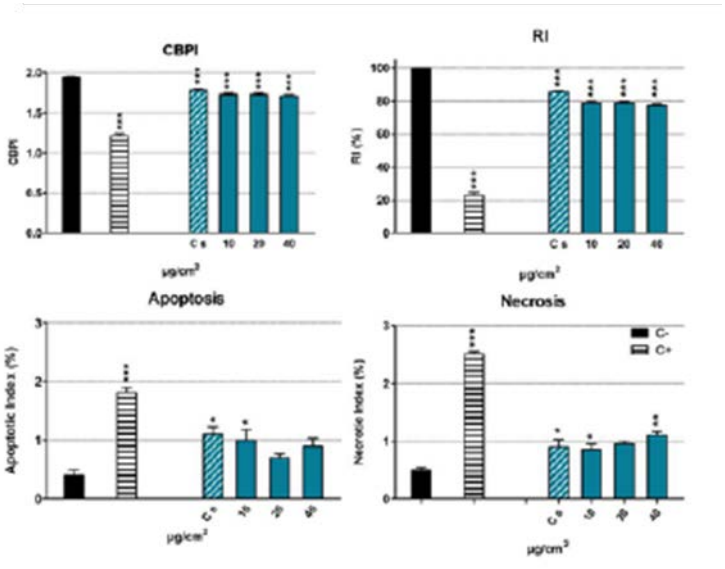

Figure 5.6 Cytostasis (CBPI and RI) and cytotoxicity (apoptosis and necrosis) evaluated by CBMN cyt assay in A549 cells. Cells were exposed exposed for 48h to the benchmark material TiO_2 P25 (Evonik). Data are plotted as mean values normalized to the untreated control (C-; black bar) ± standard error mean (SEM); n = 4. * $p< 0.05$, ** $p< 0.01$, *** $p< 0.001$. C+: 0.10 µg/ml mitomycin-C.

Besides, the results inherent to cytostasis (CBPI and RI) and cytotoxicity (apoptotic and necrotic indices) showed the potential toxic of TAC (pristine material) in A549. In particular, in A549 cells (Fig. 5.7) a significant reduction in CBPI and RI and a significantly increased apoptosis and necrosis were observed; Control solvent (Cs) resulted cytostatic and cytotoxic as well. By CBMN cyt assay TiO_2CIT significantly ($p<0.001$) increased cytostasis, apoptosis and necrosis; similarly, Cs was cytostatic and cytotoxic but the apoptotic index scored up to 10 fold increase compared to C- and 4 times higher than the pristine TAC sample. Similarly, TiO_2:SiO_2 and its Cs impaired CBPI and RI and increased apoptosis and necrosis in A549 cells, but the effects were slightly less severe than those observed in the presence of citrate coated TiO_2 NPs (TiO_2CIT).

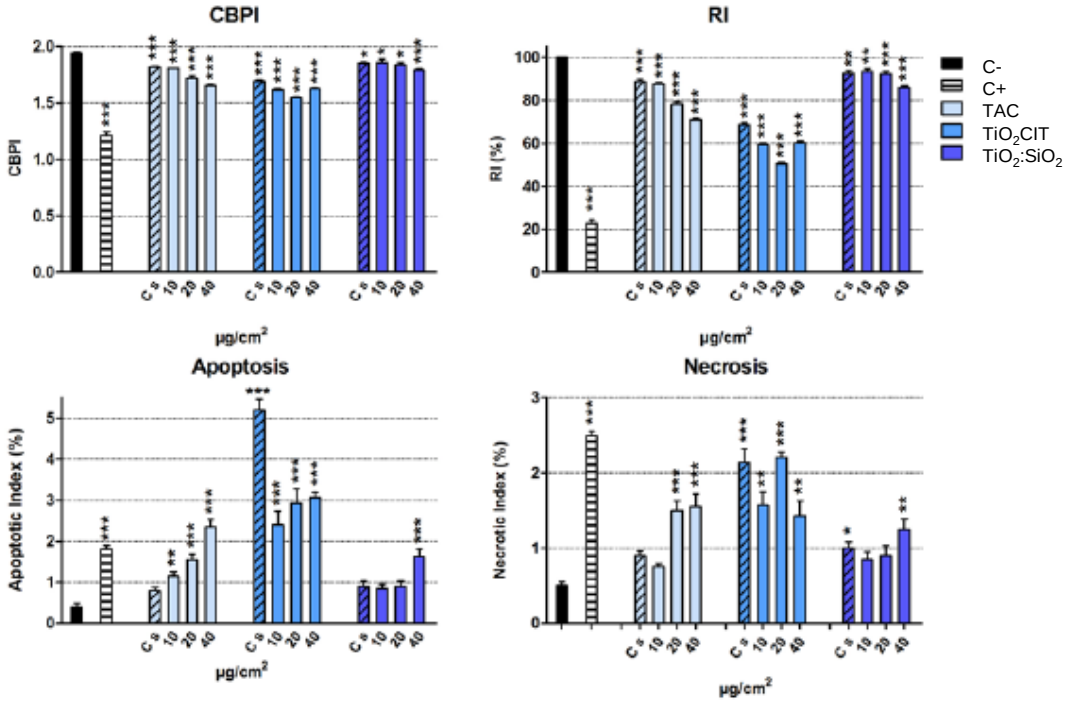

Figure 5.7 Cytostasis (CBPI and RI) and cytotoxicity (apoptosis and necrosis) evaluated by CBMN cyt assay in A549 cells. Cells were exposed for 48h to increasing concentrations (10-20-40 µg/cm2) of pristine and modified TiO_2 NP samples. Data are plotted as mean values normalized to the untreated control (C-; black bar) ± standard error mean (SEM); n = 4. * $p< 0.05$, ** $p< 0.01$, *** $p< 0.001$. C+: 0.10 µg/ml mitomycin-C.

Analogous behaviours were observed in haemolytic activity of the TiO_2 NPs when incubated in red blood cells. As shown in Figure 5.8 and detailed in Table 5.2.

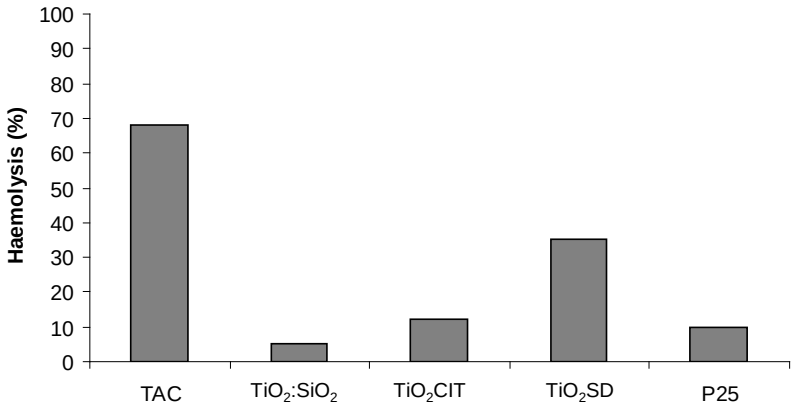

Figure 5.8 Haemolytic activity of TiO_2 NP samples at 4 mg/mL dose. Results were expressed as mean percentage haemolysis +/- (SEM; n=3) with control being set to 0% and TritonX100 being 100% red blood cell lysis.

Table 5.2 Haemolytic activity of TiO_2 based nanomaterials.

Sample	Dose (mg/mL)	MEAN	SEM
TAC	4	68.4	13.1
	2	52.5	2.7
	1	45.1	1.0
	0.5	41.2	2.1
TiO_2:SiO_2	4	3.7	0.2
	2	7.7	1.2
	1	44.7	2.1
	0.5	49.9	9.3
TiO_2CIT	4	14.1	2.6
	2	9.7	0.2
	1	8.1	0.6
	0.5	15.1	0.3
TiO_2SD	4	37.4	1.7
	2	34.7	2.4
	1	44.8	7.6
	0.5	54.4	1.3
P25	4	10.4	2.4
	2	2.3	0.8
	1	0.4	1.2
	0.5	10.0	1.1

It was observed that the pristine TiO_2 NPs (TAC) induced high levels of cell lysis (68%) which was significantly reduced in the case of the remediated forms, TiO_2:SiO_2 and TiO_2CIT, at values comparable to those observed for TiO_2 P25, suggesting effective remediation.

Overall, what can be concluded is that coating with SiO_2 and also citrate coating reduces the haemolytic potential of the pristine NPs (TAC).

5.2.3 Photocatalytic results

The photocatalytic reactivity of pristine sample and modified samples was assessed using as a model reaction the degradation of the RhB, in "TiO_2 in sol" set-up (seen Section 4.1.7.1). The graph and data inherent the degradation rate constants k (min^{-1}) were reported in Figure 5.9 and in Table 5.3, respectively.

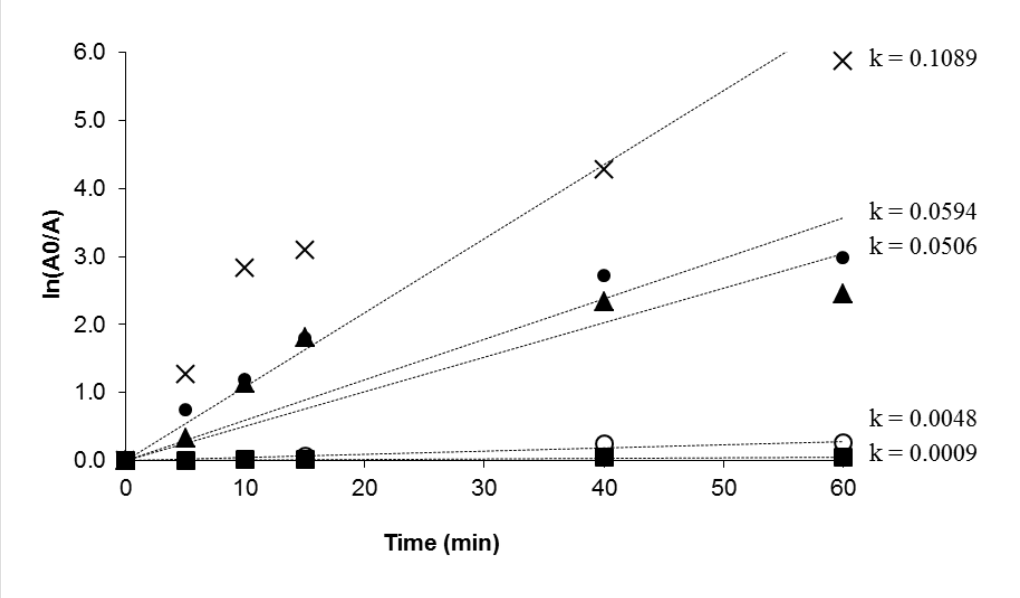

Figure 5.9 The RhB degradation kinetics and relative degradation rate constant, k (mni-1) of pristine and modified samples: × TAC; ● TiO_2SD; ▲ TiO_2:SiO_2; ○ Blank; ■ TiO_2CIT after 60 min of UV-irradiation.

It was observed that the best photocatalytic activity was shown by the pristine TiO_2 NPs, whilst the introduction of risk remediation strategies caused the decrease in photocatalytic performance. In detail, the introduction of SiO_2 coating and spray-drying

process decreased the photoactivity, but a good reactivity was preserved. Otherwise the introduction of organic coating: citrate, in TiO_2CIT sample, induced a dramatic decrease in photocatalytic performance. The reactivity of this sample was even lower than the blank. The very low reactivity of TiO_2CIT sample can be justified by the presence of citrate that, surrounding the surface, could strongly interfere with the photocatalytic process, decreasing the photocatalyst efficiency.

Table 5.3 Degradation rate constant, k (mni^{-1}) and photocatalytic efficiency % values of TiO_2 based samples.

Sample	k (min^{-1}) x 10^{-2}	Photocatalytic efficiency (%)
TAC	10.89	99.7
TiO_2:SiO_2	5.06	91.4
TiO_2CIT	0.09	4.7
TiO_2SD	5.94	94.9
Blank	0.48	22.6

As reported in the literature [23] and in Sections 4.2.2 and 4.2.3, the presence of an organic coating depresses the TiO_2 photoactivity, in particular, when the surface reactivity controls the reaction mechanism, as in this case. As regards the TiO_2:SiO_2 sample, the slight decrease in photocatalytic performance recorded could be induced by the diameter increase, corresponding to an increase of agglomeration degree, as confirmed by DLS analysis (Table 5.1) and the shielding effect that SiO_2 layer has on TiO_2 nanoparticles [24].

The SiO_2 ability to create mesoporous coatings [25] was confirmed by a faint decrease in photoreactivity shown by TiO_2:SiO_2 sample in comparison with the dramatic decrease observed in TiO_2CIT sample. Otherwise, literature data demonstrate an improvement of photocatalytic performance in the presence of mixed metal oxide TiO_2/SiO_2 [26,27].

Probably, the mechanism involved in photodegradation plays a fundamental role, as seen in previous studies inherent the photoactivity in different experimental set-ups (Section 4.2.3), that strongly influenced the performance trends.

Despite the micrometric size (Table 5.1), the sample TiO_2SD showed a good photocatalytic activity, this could further confirm that the nanostructure was preserved. The comparison between different TiO_2 samples was better highlighted in the histograms (Fig. 5.10), where the results of photocatalytic efficiency were plotted. Furthermore, the photocatalytic results were summarized in Table 5.3, obtaining the following trend, in term of photocatalytic reactivity: TAC > TiO_2SD ≥ TiO_2:SiO_2 >> TiO_2CIT.

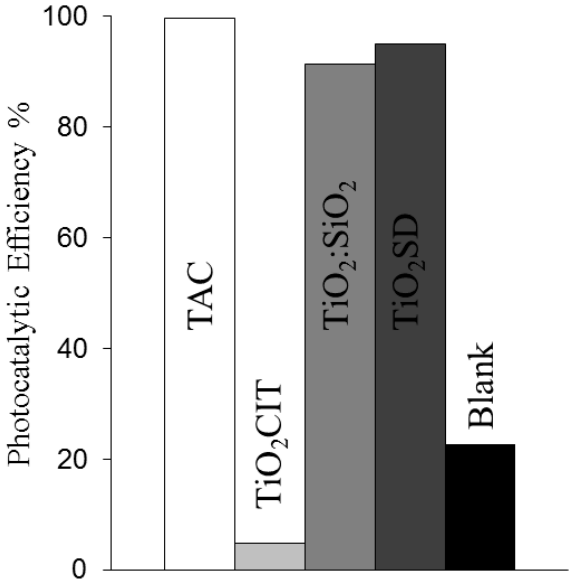

Figure 5.10 Photocatalytic efficiency (%) of pristine and modified TiO_2 NPs.

5.2.4 NO_x/NO abatement results

Functional properties of modified samples, TiO_2:SiO_2 and TiO_2CIT, were further investigated in real conditions.

TAC, TiO_2:SiO_2 and TiO_2CIT nanosols were applied, by spray-gun, on ceramic tiles and the NO_x/NO abatement analyses, under UV irradiation, were carried out.

Initially, analysis on untreated ceramic tile was performed in order to demonstrate the inactivity of support (Fig. 5.11a).

The results shown in Figure 5.11 highlighted that TAC and TiO_2CIT behaved similarly, with discrete performance whilst TiO_2:SiO_2 sample showed excellent results.

After 100 min, NO abatement was more than 90% with high conversion to NO_2, as shown in Figure 5.11c. It worth to note that, in this case, the performance of modified TiO_2:SiO_2 sample was better than pristine TiO_2 NPs (TAC) one.

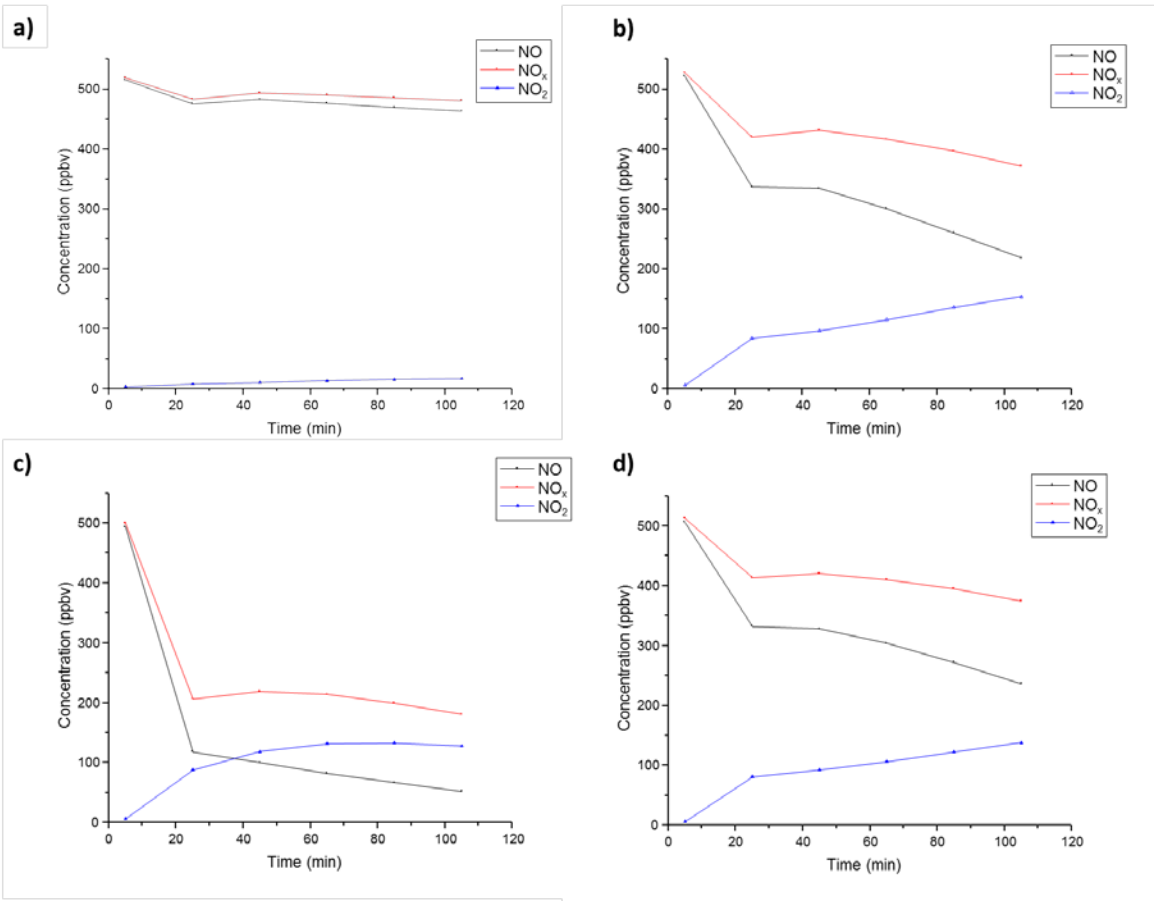

Figure 5.11 NO_x/NO abatement tests on a) untreated, b) TAC-coated, c) TiO_2:SiO_2-coated and d) TiO_2CIT-coated ceramic tile.

5.2.5 Characterization of TiO_2:SiO_2 samples [28]

TiO_2/SiO_2 systems were further investigated in term of physicochemical properties, hydrophilicity and free radicals production, due to the interesting results shown in performance evaluation (Sections 5.2.3 and 5.2.4). A study about the comparison of three analytical methods to assess the production of reactive oxygen species (ROS), hence free radicals driving the photoreactivity of TiO_2 based NPs incorporated in

textiles, was made. Besides, this study was performed with the aim to better underderstand the photocatalytic mechanism. Regarding the analytical methods, the first is the traditional scavenging or trapping method for an indirect quantification of free radicals. It uses salicylic acid (SA) as a trapping agent for free $^{\bullet}OH$ radicals. Salicylic acid reacts with hydroxyl radicals to produce stable products, namely 2,3-DHBA (2,3-dihydroxybenzoic acid), 2,5-DHBA (2,5-dihydroxybenzoic acid) which can be easily determined by High Performance Liquid Chromatography (HPLC) [14-17]. The second method exploits a glassy carbon (GC) electrode modified with an insulating film of polyphenol which has been recently proposed as an electrochemical sensor for $^{\bullet}OH$ determination [19]. The basic principle is the evaluation of the amount of modifier destroyed by the $^{\bullet}OH$ radicals, by means of the signal generated by a redox couple. Furthermore, by using this $^{\bullet}OH$ sensor the problems related to the formation of complexes between TiO_2 nanoparticles and salicylic acid are overcome [20]. At last, the third method consists in the observation of the degradation of the Rhodamine B dye, previously exploited, due to the photocatalytic action of TiO_2 and TiO_2/SiO_2 nanostructured coatings. This test allows a more direct assessment of the TiO_2 efficiency to degrade the organic matter adsorbed onto the surface (self-cleaning effect).

5.2.5.1 Physicochemical properties of target nanosols

Physicochemical characteristics of target nanosols were listed in Table 5.4.

The increase of hydrodynamic diameter as a function of TiO_2/SiO_2 ratio was caused by both the steric hindrance of SiO_2 heterocoagulated on the TiO_2 surface [21,22] and the consequent electrostatic destabilization due to the progressive neutralization of TiO_2 surface charge with the increase of SiO_2 content. Moreover, the increase of SiO_2 content in TiO_2/SiO_2 samples was associated by an increase in PDI values, demonstrating the occurrence of destabilization and agglomeration phenomena.

Elemental analyses performed by XRF (Table 5.4) confirmed the expected amounts of TiO_2 and SiO_2 and that the actual TiO_2:SiO_2 ratios were close to the nominal values (1:3.02 and 1:5.99, for TiO_2:SiO_2 1:3 and TiO_2:SiO_2 1:5 samples, respectively).

Table 5.4 Physicochemical characteristics of nanosol samples compared.

Sample	pH of nanosol	d_{DLS} (nm)	PDI	$TiO_{2\ XRF}$ (wt%)	$SiO_{2\ XRF}$ (wt%)	ζ potential (mV)	$pH_{i.e.p.}$
TiO_2 (TAC)	1.7	36	0.25	3.39	-	+108	7.7
TiO_2:SiO_2 1:0.3	1.7	59	0.27	nd	nd	nd	nd
TiO_2:SiO_2 1:3	2.2	396	0.35	3.56	10.76	+31	5.3
TiO_2:SiO_2 1:5	2.3	460	0.45	4.08	20.76	+20	4.6
SiO_2	9.7	20	0.26	-	nd	-55	<2

nd: not determined

The best conditions driving the self-assembled heterocoaugulation process between different colloidal phases occur when such species exhibit, at the working pH, ζ potentials opposite in sign and high enough to preserve colloidal stabilization. From data reported in Table 5.4 and Figure 5.12, such conditions were fulfilled at pH lower than the isoelectric point of TiO_2 ($pH_{i.e.p.}$ 7.7), where TiO_2 and SiO_2 presented positive and negative ζ potentials, respectively. The SiO_2 pH 4.0 and the original TiO_2 pH 1.7 were selected to promote the heterocoagulation between positive TiO_2 and negative SiO_2 nanosurfaces.

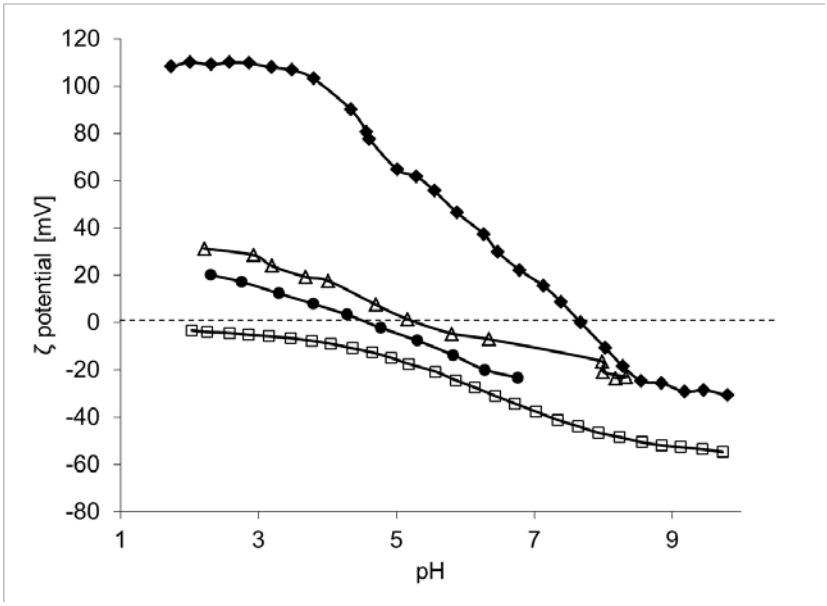

Figure 5.12 ζ potential as a function of pH for(♦) TiO_2 (TAC), (Δ) TiO_2:SiO_2 1:3, (●) TiO_2:SiO_2 1:5 and (□) SiO_2 nanosol. The dashed line for ζ potential=0 is used for the $pH_{i.e.p.}$ determination.

The attraction between oppositely charged surfaces led to the formation of TiO_2/SiO_2 systems, where TiO_2 nanoparticles were incapsulated in SiO_2 matrix, consists of NPs, as confirmed by TEM observations. TiO_2:SiO_2 heterocoagulated samples showed a mixed structure, as shown in Figure 5.3b and 5.13, for TiO_2:SiO_2 1:3 and TiO_2:SiO_2 1:5 samples, respectively. Despite the lack of a well definite and compact SiO_2 coating around TiO_2 NPs, it was observed that, due to the SiO_2 excess conditions, each TiO_2 NP was surrounded by SiO_2 NPs, and so dispersed within SiO_2 matrix. This is particularly evident in TiO_2:SiO_2 1:5, as confirmed by EDX analysis, shown in Figure 5.14.

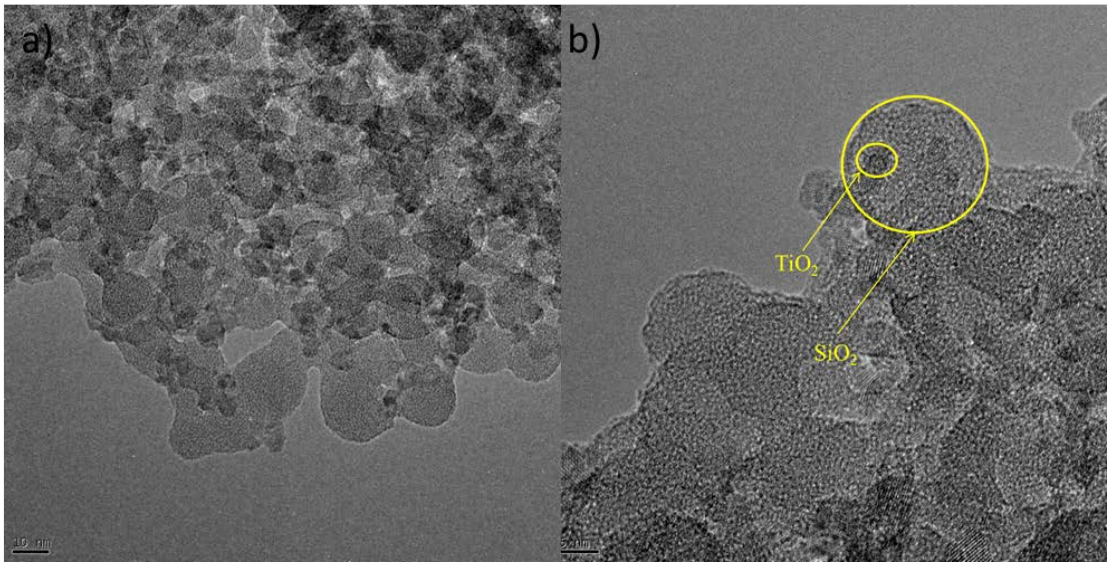

Figure 5.13 TEM imagines of mixed TiO_2 and SiO_2 nanophases in TiO_2:SiO_2 1:5 sample.

The TiO_2/SiO_2 surfaces attraction was also demonstrated by the $pH_{i.e.p}$ shift of TiO_2/SiO_2 sols towards acidic pH, increasing SiO_2 concentration, as already observed in the literature [29,30]. Such a shift of $pH_{i.e.p.}$ indicated an enhanced surface acidity by increasing the SiO_2 content. This was expected since the silica surface had different populations of hydroxyl groups which are weakly acidic (Eq. 5.2) [31].

$$\equiv SiOH \leftrightarrows SIO^- + H^+ \qquad \text{(Eq. 5.2)}$$

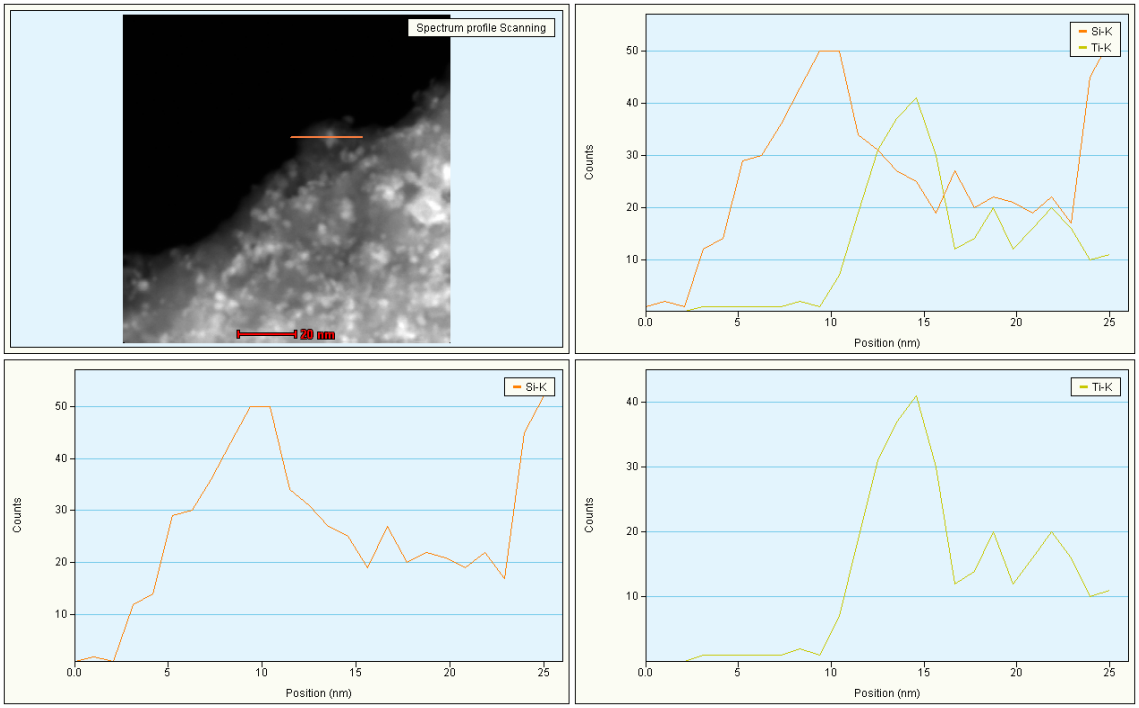

Figure 5.14 EDX-STEM analysis on TiO_2:SiO_2 1:5 sample.

5.2.5.2 Hydrophilic behavior

Microcalorimetric measurements were carried out on spray-dried samples, so the microcalorimetric data were calculated through SSA values of powder samples, reported in Table 5.5.

Table 5.5 Specific surface area by BET (SSA_{BET}) of spray-dried powder samples.

Sample	SSA_{BET} ($m^2 g^{-1}$)
TiO_2 (TAC)	237
TiO_2:SiO_2 1:3	255
TiO_2:SiO_2 1:5	177
SiO_2	201

Microcalorimetric data on the investigated samples reveal the affinity towards water molecules.

Adsorption data obtained for pure SiO_2, pure TiO_2 and TiO_2/SiO_2 samples (with TiO_2:SiO_2 ratios1:3 and 1:5) were shown in Figure 5.15 along with the volumetric isotherms (panel a) and calorimetric data (panel b). In the case of pure silica sol the interaction of the sample with water was, as expected, fully reversible (i.e. adsorption run curves I and II are coincident – Fig. 5.15a). This indicates that water interacted with the surface through hydrogen bonds and that no dissociative adsorption occurred, as further confirmed by the relatively low enthalpy of adsorption (Fig. 5.15b) observed in particular at low coverage (~90 kJ/mol at ~1 μmol/m^2).

On pure titania sample the amount of adsorbed water was higher with respect to pure SiO_2 (Fig. 5.15a) and not fully reversible (~15% irreversibility) while the adsorption enthalpy at low coverage (~110 kJ/mol) is that expected for an ionic metal oxide. These data are in agreement with what previously reported [13,32] and indicate a different level of hydrophilicity for TiO_2 and SiO_2 nanosols.

The water molecules at the surface of pure titania were strongly coordinated to *cus* Ti^{4+} cations or strongly H-bonded to surface Ti-OH species. These strongly bound water cannot be removed by a simple outgassing at 303K (irreversibility~15%). On the contrary, the adsorption of water occured on the silica particles through less energetic hydrogen bonds with silanols (-Si-OH) exposed at the surface.

The amount of water taken up by the two TiO_2/SiO_2 samples (TiO_2:SiO_2 1:3 and TiO_2:SiO_2 1:5) was even slightly higher with respect to that of pure TiO_2, whereas the irreversibility was similar to that of the TiO_2 sample (~15%). As to adsorption enthalpy, the TiO_2/SiO_2 samples exhibited values very similar to the titania specimen thus confirming the accessibility of water vapour to the titania surface.

From these observations, it appeared that the behaviour/reactivity of TiO_2/SiO_2 samples towards water was not intermediate between silica and titania, as would occured for a simple mixing of silica and titania powders.

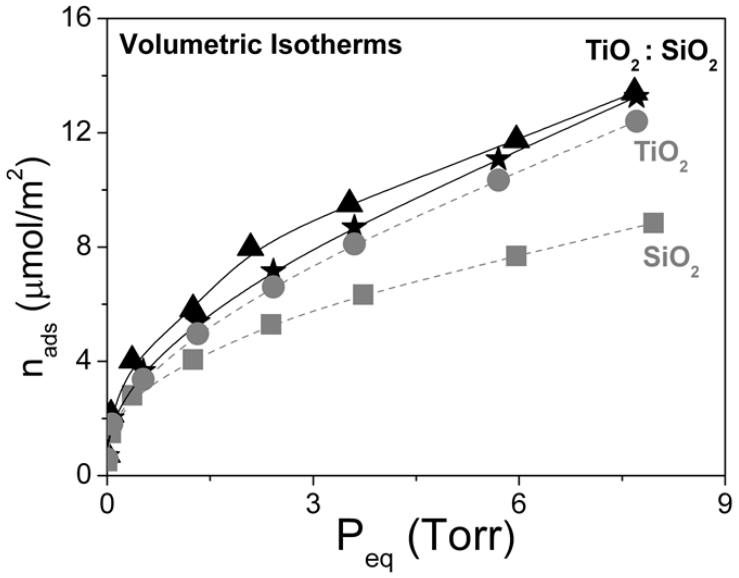

a)

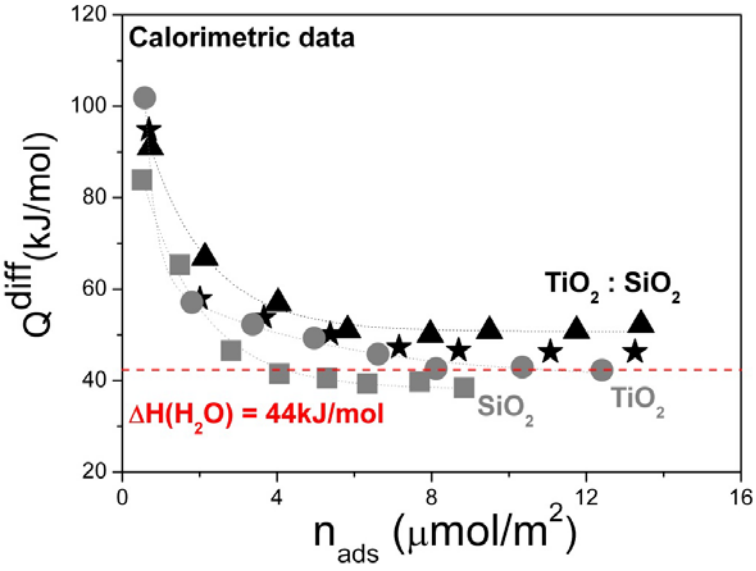

b)

Figure 5.15 a) Volumetric isotherms (T = 303K): uptake for H_2O vapor adsorption(n_{ads}) vs. $P_{eq(H2O)}$ on the samples TAC (●), SiO_2 (■), TiO_2:SiO_2 1:3 (▲) and TiO_2:SiO_2 1:5 (★). b) Calorimetric data (T = 303 K): adsorption enthalpy (Q^{diff}) vs. uptake of H_2O vapor (n_{ads}). Data related to I run of adsorption are reported. Latent enthalpy of liquefaction of water: $-\Delta_L H(H_2O)$ = 44kJ/mol (red dotted line).

The presence of TiO_2 in the SiO_2 matrix increased the amount of adsorbed water molecules without modifying the adsorption energy, which appeared to be similar to that of the pure titania sample. This suggested the presence of patches of TiO_2/SiO_2 mixed phases among the TiO_2 and SiO_2 particles that could generate defect sites that were able to bind further water molecules with energy similar to that of the defect sites present on titania. Overall, the addition of SiO_2 has caused an increase in the surface hydrophilicity of titania.

5.2.5.3 Reactive oxygen species (ROS) production

As regards, the first method, it was noted that, the peaks relevant to 2,5 DBHA and 2,3 DBHA were well evident in the chromatograms recorded for all the experiments that used the nanosystems containing TiO_2. On the other hand, the concentrations of these compounds were very low for SiO_2 nanoparticles. Moreover, a control experiment was carried out irradiating a SA solution. The 2,3 DBHA and 2,5 DBHA concentrations resulted lower than the limit of detection suggesting that the SA self-degradation under UV irradiation is negligible. When 2,5 DBHA and 2,3 DBHA were obtained at high concentrations, their time trends displayed a maximum at about 3 min (Fig. 5.16).

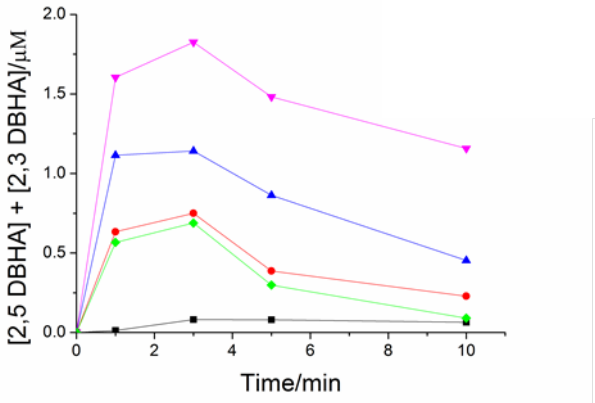

Figure 5.16 Trends in the sum of concentrations of 2,5-DBHA and 2,3-DBHA during photocatalysis of TAC (♦), SiO_2 (■), TiO_2:SiO_2 1:0.3 (●),TiO_2:SiO_2 1:3 (▲) and TiO_2:SiO_2 1:5 (▼) nanosols as measured by SA trapping method.

This behavior is usually observed for reaction products that, in turn, can react and consequently disappear from the reaction environment. Indeed, the kinetic constants of

the $^{\bullet}OH$ reactions with isomers of di-hydroxy benzoic acid were slightly higher than that of SA. A relative scale of the $^{\bullet}OH$ production rates was built using the sum of 2,5 DBHA and 2,3 DBHA concentrations determined at 1 min in order to avoid any underestimation. The relative rates of $^{\bullet}OH$ radical production were reported in Table 5.6.

Table 5.6 Relative scale of $^{\bullet}OH$ production rates evaluated with the SA trapping (sum of 2,3-DBHA and 2,5-DBHA concentrations) for the different photocatalysts. The yields of 2,3-DBHA and 2,5-DBHA are also reported.

Photocatalyst	Rate of 2,3-DBHA production (M min^{-1})	Rate of 2,5-DBHA production (M min^{-1})	Rate of $^{\bullet}OH$ production (M min^{-1})	Yield of [2,3-DBHA] %	Yield of [2,5-DBHA] %
TAC	$4.93 \cdot 10^{-7}$	$0.74 \cdot 10^{-7}$	$5.7 \cdot 10^{-7}$	4.0	0.6
TiO_2:SiO_2 1:0.3	$5.05 \cdot 10^{-7}$	$1.29 \cdot 10^{-7}$	$6.3 \cdot 10^{-7}$	2.2	0.6
TiO_2:SiO_2 1:3	$2.60 \cdot 10^{-7}$	$8.56 \cdot 10^{-7}$	$11.1 \cdot 10^{-7}$	0.3	1.1
TiO_2:SiO_2 1:5	$4.44 \cdot 10^{-7}$	$11.6 \cdot 10^{-7}$	$16.0 \cdot 10^{-7}$	0.8	2.1
SiO_2	< LOD	$3.0\ 10^{-8}$	$3.0\ 10^{-8}$	nd	0.2

nd: not determined

An evident increase of photoreactivity as a function of SiO_2 weight percentage was appreciable from the results of $^{\bullet}OH$ radicals formation by the trapping method with salicylic acid.

Both the 2,5 DBHA and 2,3 DBHA yields were examined in order to get an insight into the SA hydroxylation reaction. These values were strongly dependent on the kind of photocatalyst, suggesting that the NPs play a role in the reaction between SA and $^{\bullet}OH$ radicals. Indeed, SA was adsorbed on TiO_2 surface [20] as highlighted by the change of suspension color from white to yellow when SA was added to nanosols. The SA adsorption was critical for the observed interaction between SA and $^{\bullet}OH$ radicals [33,34]. In the present study, it was the adsorbed SA that reacted with $^{\bullet}OH$ radicals, which also could themselves be adsorbed on the photocatalyst. This promoteed a different reaction pathway that led to a different distribution of reaction products. The phenomenon was also observed by Ai et al., who investigated electro-oxidation of SA

mediated by $^{\bullet}OH$ radicals at a PbO_2 electrode [35]. These data suggest that the surface chemistry of NPs plays a key role in SA oxidation and, consequently, in the determination of the amount of $^{\bullet}OH$ radicals produced by photocatalysts.

In the second method, the free radicals produced by photocatalysts were detected using a polyphenol modified electrode. The analytical signal used for this determination was the amount of insulating polyphenol film that was removed from the electrode surface as a consequence of the $^{\bullet}OH$ radicals attack. The relative scale of $^{\bullet}OH$ production rates was built using the values of the uncovered areas obtained from CA responses for all the experiments (Fig. 5.17).

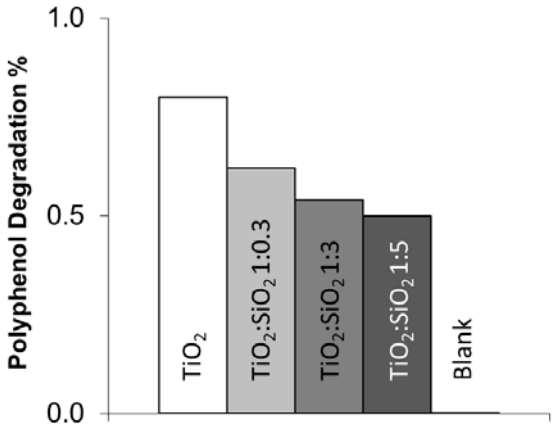

Figure 5.17 Determination of $^{\bullet}OH$ radicals by the electrochemical method. The blank represents the test without photocatalyst.

The highest $^{\bullet}OH$ production was measured when TiO_2 nanoparticles were irradiated. The amount of detected $^{\bullet}OH$ radicals decreased as SiO_2 content increased and SiO_2 nanoparticles displayed the lowest radical production. Therefore, the present technique revealed a negative effect of SiO_2 presence in the redox reactivity of the target catalysts, in disagreement with the results of SA trapping method. Such a trend can be explained considering that $^{\bullet}OH$ radicals can diffuse for only few nanometers and that the OH probe is confined on the electrode surface [36].

Therefore, the transport phenomena between the OH production sites and the sensitive film play a key role on the detection of $^{\bullet}OH$ radical. SiO_2 nanoparticles that were absorbed on TiO_2 were a physical obstruction that keeps the active surface of the

catalyst away from the electrode surface. Therefore, the $^{\bullet}OH$ radicals were produced by the photocatalyst but unlikely they reach the electrode when the SiO_2 nanoparticles are adsorbed on the photocatalyst. Therefore, the electrochemical method evaluated the $^{\bullet}OH$ radicals production combined with the ability of the radicals to escape from the environment where they were generated. We can conclude saying that the SiO_2 presence reduced the $^{\bullet}OH$ radicals availability far away from the production site making the contact with the target molecule more difficult.

Lastly, the RhB photodegradation results were indicative of the self-cleaning performance of photocatalyst-treated textiles (Fig. 5.18).

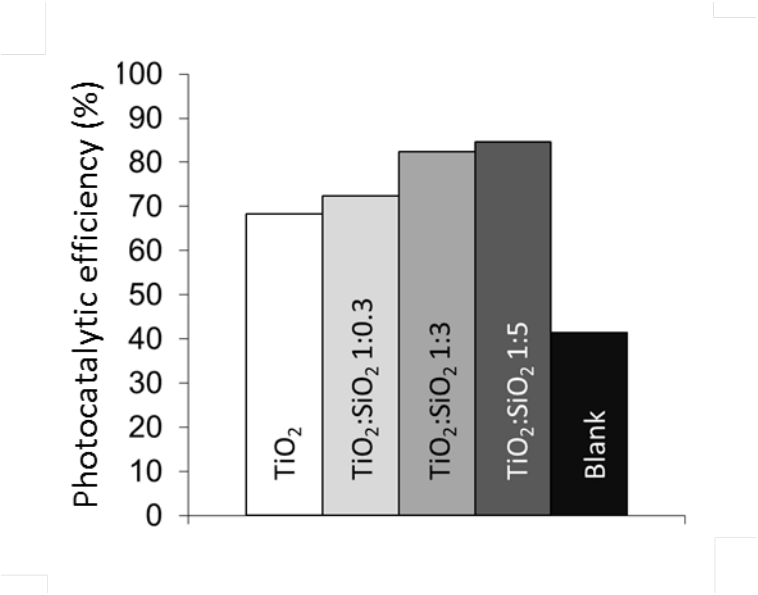

Figure 5.18 Photocatalytic test (RhB photodegradation) results in self-cleaning application, after 120 min of UV irradiation. The blank represents untreated textile.

The experimental set-up in self-cleaning application was designed to mimic a mechanism closer to gas phase reactions, where pollutants can be oxidized directly at the surface, once adsorbed, rather than by photo-generated soluble species.

All functionalized textiles, as expected, exhibited a self-cleaning activity higher than the untreated textile (blank).

In particular, textiles treated with TAC showed an activity about 75% higher than that of the untreated textiles. Interestingly, the addition of SiO_2 to TiO_2, giving rise to a matrix encapsulation structure, improved the photocatalytic performance, despite the

pure SiO_2 NPs are much less photocatalytic than TiO_2. This may be connected with the higher hydrophilicity of the mixed TiO_2/SiO_2 system, as discussed in the Section 5.2.5.2. In fact, the hydrophilicity of TiO_2 coated substrate was found to be one of the key parameters to control the photocatalytic performance in self-cleaning applications, as seen in Sections 4.2.2 and 4.2.3.

Furthermore, similar studies reported comparable results [37]. In the present case, the TiO_2/SiO_2 nanosystems appeared to be more hydrophilic than TiO_2 (TAC sample), as demonstrated by the high adsorption enthalpy towards water (Fig. 5.15) thus justifying the higher reactivity of these samples [26,38,39].

Summarizing, the trapping method with salicylic acid revealed an improvement of photocatalytic efficiency when the content of SiO_2 increased in the TiO_2/SiO_2 samples. A similar trend was found in the RhB test when applied to the TiO_2-coated textile. As a matter of fact, photodegradation mediated by the direct interaction of target molecules with surface oxidizing carriers dominated both SA trapping and RhB tests, but the former was able to better predict, in quantitative terms, the self-cleaning capacity of photocatayst nanomaterials incorporated in a textile.

On the other hand, the electrochemical method showed a decrease in the ROS (free radicals) production as the silica content increased, thus implying an apparent decrease in the photocatalytic performance. In such a case, the degradation of the target molecules was likely to be mediated by hydroxyl radicals released in solution. Therefore, it largely depended on the fate of such radicals diffusing into the surrounding medium. Thus, the electrochemical method was less predictive of photocatalyst efficiency if applied to self-cleaning textiles.

5.3 Conclusion

In conclusion, "safety by molecular design" strategies were applied to control the potential risk of TiO_2 nanosols and the obtained samples characterized. Biological and performance evaluation tests revealed that the most promising sample was TiO_2/SiO_2 system. In fact, it showed a decrease in toxicological behavior in comparison with pristine sample (TAC) and very interesting results in performance evaluation. In

particular, in NO_x/NO abatement tests TiO_2:SiO_2 demonstrated an increase in NO abatement linked to an high conversion to NO_2 in comparison with TiO_2 pristine NPs (TAC).

Furthermore, regarding the depth study inherent on TiO_2/SiO_2 system, the addition of SiO_2 to commercial TiO_2 nanosols gives rise to an improvement in the photocatalytic performances of self-cleaning textiles. The role of SiO_2 can be explained by the increase of the photocatalyst surface acidity, with consequent increase of hydrophilicity in TiO_2/SiO_2-coated textiles. This enhanced photocatalytic efficiency by increasing the content of SiO_2 was confirmed detecting $^{\bullet}OH$ radicals by the trapping method with salicylic acid. Nevertheless, when hydrophilicity does not strongly affect the photocatalytic process, the addition of SiO_2 is unable to increase the TiO_2 photoreactivity. This trend was verified determining $^{\bullet}OH$ radicals by the electrochemical method: the decrease of ROS production, as silica content increases, can be well predicted by the percentage of radicals formed and diffused to the electrode. The results suggest that the photoactivity of TiO_2 incorporated in textiles is mainly related to a direct reactivity of the surface oxidizing carriers toward the organic target molecule. The salicylic acid and RhB tests provided mutually consistent data with similar trends in the photocatalytic performance of self-cleaning textiles.

On the other hand, the electrochemical method is a valid alternative when photocatalytic reactivity is driven by $^{\bullet}OH$ radicals diffused in a liquid medium. For self-cleaning textile applications, the salicylic acid test is able to predict on a more reliable quantitative basis the photocatalytic activity, while the Rhodamine B test represents a robust qualitative indicator.

5.4 References

[1] P. Verlooy, A. Aerts, O.I. Lebedev, G. Van Tendeloo, C. Kirschhock, J.A. Martens, Chem. Commun. (2009) 4287–4289.

[2] S.P. Hudson, R.F. Padera, R. Langer, D.S. Kohane, Biomaterials 29 (2008) 4045–4055.

[3] J.H. Park, L. Gu, G. von Maltzahn, E. Ruoslahti, S.N. Bhatia, M.J. Sailor, Nat. Mater. 8 (2009) 331–336.

[4] C.T. Kresge, M.E. Leonowicz, W.J. Roth, J.C. Vartuli, J.S. Beck, Nature 359 (1992) 710–712.

[5] A. A. Torrano, Â. S. Pereira, O. N. Oliveira, A. Barros-Timmons, Colloids and Surfaces B: Biointerfaces 108 (2013) 120–126.

[6] J. I. Kwak, W.-M. Lee, S. W. Kim, Y.-J. An, J. Appl. Toxicol. 34 (2014) 1145–1154.

[7] V. Mangini, M. Dell'Aglio, A. De Stradis, A. De Giacomo, O. De Pascale, G. Natile, F. Arnesano, Chem. Eur. J. 20 (2014) 10745–10751.

[8] G. Li, X. Yang, J. Wang, Colloids and Surfaces A: Physicochem. Eng. Aspects 322 (2008) 192–198.

[9] K. Yamaguchi, M. Ito, T. Taniguchi, S. Kawaguchi, K. Nagai, Colloid. Polym. Sci. 282 (2004) 366–372.

[10] M. Okubo, Y. He, K. Ichikawa, Colloid. Polym. Sci. 269 (1991)125–130.

[11] D.K. Schwartz, Annu. Rev. Phys. Chem. 52 (2001) 107–137.

[12] V. Bolis, C. Busco, P. Ugliengo, J. Phys. Chem. B 110 (2006) 14849–14859.

[13] V. Aina, F. Bonino, C. Morterra, M. Miola, C.L. Bianchi, G. Malavasi, M. Marchetti, V. Bolis, J. Phys. Chem. C 115 (2011) 2196–2210.

[14] S.M. Ould-Mame, O. Zahraa, M. Bouchy, Int. J. Photoenergy 2 (2000) 59–66.

[15] J.-F. Jen, M.-F. Leu, T.C. Yang, J. Chromatogr. A 796 (1998) 283–288.

[16] T.-C. Cheng, K.-S. Yao, Y.-H. Hsieh, L.-L. Hsieh, C.-Y. Chang, Mater. Des. 31 (2010)1749–1751.

[17] C. von Sonntag, Free-Radical-Induced DNA Damage and its Repair, Springer, Heidelberg, 2006.

[18] N. Shimizu, C. Ogino, M.F. Dadjour, K. Nihomiya, A. Fuijhira, K. Sakiyama, Ultrason. Sonochem. 15 (2008) 988–994.

[19] I. Gualandi, D. tonelli, Talanta 115 (2013) 779–786.

[20] A.E. Regazzoni, P. Mandelbaum, M. Matsuyoshi, S. Schiller, S.A. Bilmes, M.A. Blesa, Langmuir 14 (1998) 868–874.

[21] Q. Wu, Z. Wang, X. Kong, X. Gu, G. Xue, Langmuir 24 (2008) 7778–7784.

[22] J. Sun, L. Gao, Carbon 41 (2003) 1063–1068.

[23] S. Livraghi, I. Corazzari, M.C. Paganini, G. Ceccone, E. Giamello, B. Fubini, I. Fenoglio, Chem. Commun. 46 (2010) 8478–8480.

[24] M. H. Lee, U. M. Patil, S. T. Kochuveedu, C. S. Lee, D. H. Kim, Bull. Korean Chem. Soc. 33 (2012) 3767–3771.

[25] C. Wu, Z. Zhao, Y. Zhao, Y. Hao, Y. Liu, C. Liu, Int. J. Pharm. 475 (2014) 298–305.

[26] T. Yuranova, R. Mosteo, J. Bandara, D. Laub, J. Kiwi, J. Mol. Catal. A: Chem. 244 (2006) 160–167.

[27] R. Fateh, R. Dillert, D. Bahneman, Langmuir 29 (2013) 3730−3739.

[28] S. Ortelli, M. Blosi, C. Delpivo, D. Gardini, M. Dondi, I. Gualandi, D. Tonelli, V. Aina, I. Fenoglio, A. Gandhi, S. Tofail, A. Costa, J. Photochem. Photobiol. A: Chem. 292 (2014) 26–33.

[29] M. Zhang, L. Shi, S. Yuan, Y. Zhao, J. Fang, J. Colloid Interface Sci. 330 (2009) 113-118.

[30] M. Kari, M. Montazeri-Pour, M. Rajabi, V. Tizjang, S. Moghadas, J. Mater. Sci: Mater. Electron. 25 (2014) 5560–5569.

[31] A. Rimola, D. Costa, M. Sodupe, J.-F. Lambert, P. Ugliengo, Chem. Rev. 113 (2013) 4216–4313.

[32] V. Bolis, C. Busco, M. Ciarletta, C. Distasi, J. Erriquez, I. Fenoglio, S. Livraghi, S. Morel, J. Colloid Interface Sci. 369 (2012) 28–39.

[33] D.S. Bhatkhande, V.G Pangarkar, A. ACM Beenackers, J. Chem Technol. Biotechnol. 77 (2002) 102–116.

[34] S. Tunesi, M. Anderson, J. Phys. Chem. 95 (1991) 3399–3405.

[35] S. Ai, Q. Wang, H. Lui, L. Jin, J. Electroanal. Chem. 578 (2005) 223–229.

[36] Q. Guo, Q. Yue, J. Zhao, L. Wang, H. Wang, X. Wei, J. Liu, J. Jia, Chem. Commun. 47 (2011) 11906–11908.

[37] E. Pakdel, W.A. Daoud, J. Colloid Interface Sci. 401 (2013) 1–7.

[38] K.Y. Jung, S.B. Park, J. Photochem. Photobiol. A: Chem. 127 (1999) 117–122.

[39] C. Anderson, A.J. Bard, J. Phys. Chem. B 101 (1997) 2611–2616.

Chapter 6: ANTIBACTERIAL TEXTILES

In order to obtain Ag based nanostructured materials suitable to biotechnological application, Ag nanophases were engineered and integrated onto adequate inert supports: textiles. Ag nanosized particles were prepared by developing eco-friendly, easily scalable and sustainable syntheses, allowing a right control on particle size and composition. The so-synthesized NPs, in form of stable colloidal nanosuspensions, were integrated onto cotton and polyamide based textiles by dip-padding-curing method. The antibacterial properties of nano-Ag functionalized antibacterial textiles were tested and exploited with the final purpose to be applied during the pre and post bacteria treatments in the polyhydroxyalcanoates (PHAs) biopolymers production process [1-3].

6.1 Experimental Section

6.1.1 Materials

The following analytic grade reagents were used: silver nitrate and sodium hydroxide (Sigma Aldrich). SoftCAT^{TM} SL-30 (hydroxyetylcellulose) was purchased by Amerchol. Standard cotton and polyamide textiles, provided by ISMAC-CNR of Biella, were used in these studies.

6.1.2 Preparation of Ag nanosuspension

The Ag nanosol sample, called AgHEC, was synthetized starting from $AgNO_3$, at room temperature, with hydroxyetylcellulose as reducing and dispersant agent, in basic conditions (adding NaOH). The final Ag concentration in nanosol was 0.05M.

6.1.3 Characterization of Ag nanosuspension

Ag nanosol was characterized by dynamic light scattering (DLS), electrophoretic light scattering (ELS), field emission – scanning electron microscopy (FE-SEM), optical spectroscopy (UV-Vis) and X-ray diffraction (XRD).

Dynamic light scattering (DLS) was used to monitor the hydrodynamic diameter and the particle size distribution of the suspensions. The hydrodynamic diameter includes

the coordination sphere and the species adsorbed on the particle surface such as stabilizers, surfactants and so forth. Electrophoretic light scattering (ELS) was used to measure the ζ potential of the suspensions. DLS and ELS techniques were performed by (Zetasizer Nanoseries - Malvern Instruments, UK) on suspensions with 0.3 wt% concentration. FE-SEM analysis was used to monitor the morphology and the agglomeration state of Ag nanosuspension. FE-SEM analyses were carried out by FE-SEM (Carl Zeiss Sigma NTS Gmbh Öberkochen, Germany). UV-Vis extinction spectra were measured with a Lambda 35 spectrophotometer (Perkin Elmer, UK), using a quartz cuvette as sample-holder. Samples for UV-Vis spectroscopy were prepared by diluting the as prepared colloidal suspension with water (dilution ratio 1:200). Diffraction patterns were collected for the synthesized samples dripped on a glass slide and dried at 100 °C for 15 minutes. Analyses were performed by the Bruker D8 Advance diffractometer (Germany) operating in θ/2θ configuration, with a XCeleretor detector (25-80 ° 2θ range, 0.02 step size, 0.5 s time-per-step).

6.1.4 Functionalization method on textile support

In order to produce Ag coated fabrics, standard cotton and polyamide textiles were used. In particular, polyamide textiles initially were pre-washed to improve the affinity for the nanosols and increase the hydrophilic properties. So, standard polyamide textiles were dipped in flasks containing ethanol (80% v/v) and demineralised water at 70 °C for 30 min. The liquor ratio was 80:1 mL/g (volume of solution : weight of fabric). The samples were dried at room temperature.

The Ag nanosols were applied onto textiles through dip-dapping-curing method (Fig. 4.1). A brief study inherent to dip-padding-curing process conditions was necessary to optimize Ag NPs adhesion onto textile.

Different Ag concentrations (0.01 and 0.05 wt%) and curing temperatures (60°, 80° and 100°C) were tested, maintaining constant the other parameters: 50°C as drying temperature and 10 min as curing residence time. At last, the coated fabrics were post-washed in water (known volume) in ultrasound bath for 15 min. ICP-AES (Inductively coupled plasma atomic emission spectroscopy) analysis was exploited to evaluate the

adhesion efficiency of Ag nanoparticles on textile support, estimating the Ag concentration in washing water (obtained after the post-washing process).
The analyses were performed by inductively coupled plasma atomic emission spectrometer (Liberty 200; Varian, Clayton South, Australia).
Then the Ag weight loss (%) was evaluated and calculated by the formula:

$$\text{Weight loss } (\%) = \frac{w_L}{w_0} \times 100 \qquad \text{(Eq. 6.1)}$$

where w_0 and w_L represent the initial Ag weight (on textile) and the Ag weight in washing water (amount lost), respectively.

6.1.5 Antibacterial tests

Functional properties of Ag coated cotton textiles were tested in antibacterial tests.
Antibacterial tests against mixed microbial cultures on Ag coated cotton textiles were based on AATCC 100 Test Method. The same analyses were carried out against Klebsiella pneumoniae (ATCC 4352, Gram negative) in order to compare the antibacterial performances of the treated fabrics. The procedures was the following:

- 1 ml of bacteria inoculum containing 1.5-3 × 105 CFU/ml was put on the samples with silver and on the corresponding reference untreated fabric. Then the samples were incubated at 37 °C for 1 h. After this time 100 ml of sterile buffer were added to each sample, the buffer was then dilute ten times and pleated on Petri dishes with suitable agar. The Petri dishes were incubated at least 24 h at 37 °C, then the colonies were counted.

Bacterial reduction is calculated using the following equation:

$$\text{Bacterial reduction } (\%) = \frac{B - A}{B} \times 100 \qquad \text{(Eq. 6.2)}$$

where A is the number of colonies of the Ag treated fabrics and B is the number of colonies of the untreated samples (references).

6.2 Results and discussion

6.2.1 Characteristics of Ag nanosuspension

The Ag nanosol (AgHEC), synthetized starting from $AgNO_3$, was produced exploiting an amine functionalized hydroxyethylcellulose (Fig. 6.1) as reducing and dispersant agent.

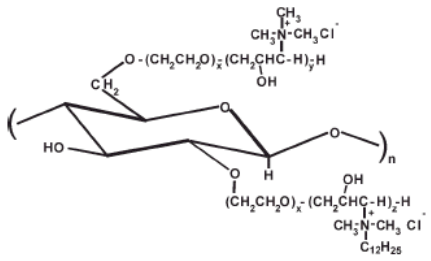

Figure 6.1 Molecular structure of hydroxyethylcellulose used in synthesis of AgHEC nanosol.

The high hydrodynamic diameters (about 340 nm), determined by DLS, indicating that aggregation phenomena occurred. In fact, FE-SEM analysis showed very small primary particle size (about 10 nm) and, concurrently, the presence of aggregate with higher size (diameter about 150 nm), as Figure 6.2 highlights.

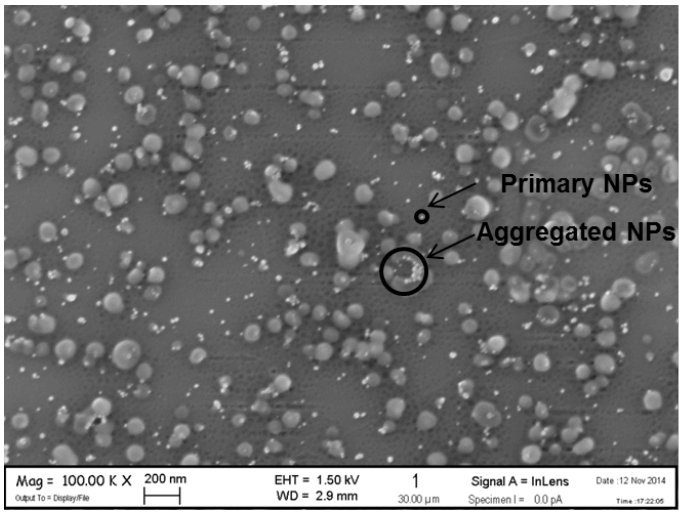

Figure 6.2 FE-SEM imagine of AgHEC nanosol sample.

The ζ potential measurements showed the presence of positive charged NPs, as expected, due the presence of amine groups in hydroxyethylcellulose molecules.
The results of physicochemical characterization were summarized in Table 6.1.

Table 6.1 Characteristics of Ag HEC nanosol.

d_{DLS} (nm)	342
Primary particle size (nm)	10
Secondary particle size (nm)	150
ζ potential (mV)	+10

The efficiency in $AgNO_3$ conversion to Ag metallic phase was demonstrated by the XRD and UV-vis results.
XRD spectra proved the presence of the metallic phase with the peak broadening typical of nanometric crystallites (Fig. 6.3).

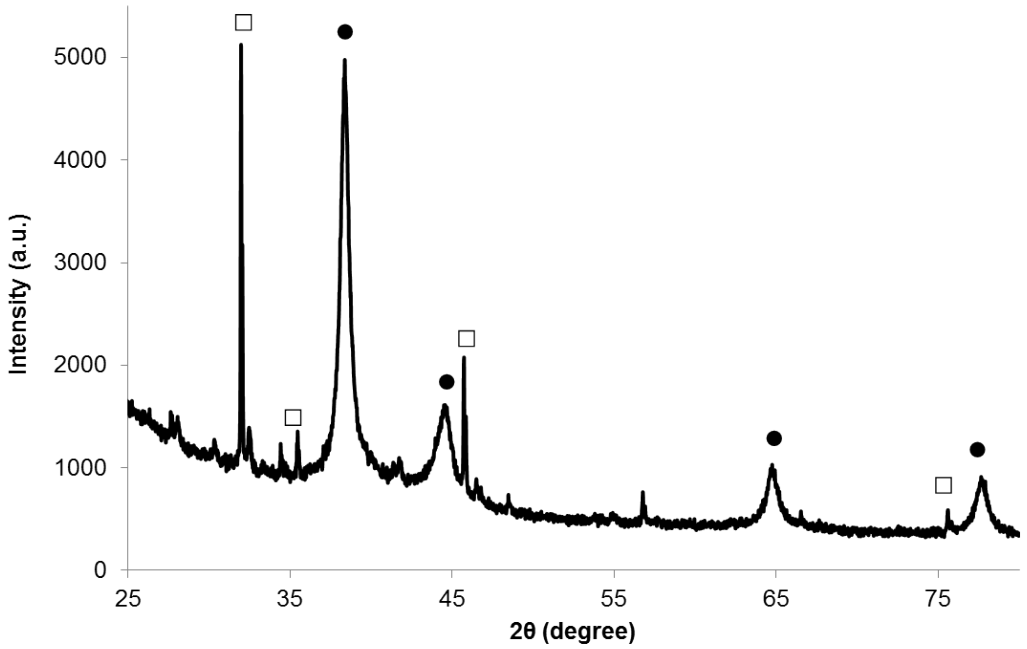

Figure 6.3 XRD diffractogram of Ag nanosuspension, AgHEC sample (● = metallic silver; □ = sodium nitrite).

The main phase detected was Ag^0 (JCPDS card n. 65-2871), together with other small peaks, corresponding to synthesis by-products. Among them, the majority phase was sodium nitrite (JCPDS card n. 39-0527).
UV-Vis spectra (Fig. 6.4) showed the typical surface plasmon resonance peak of silver NPs, that is at around 400 nm [4,5].

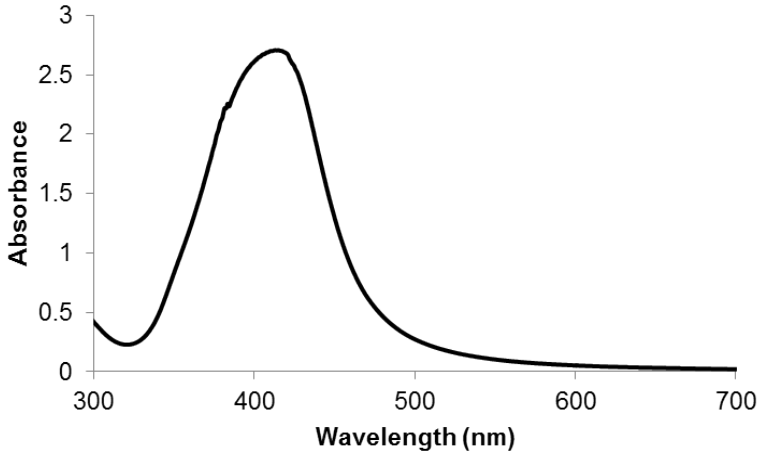

Figure 6.4 UV-vis spectra of AgHEC sample.

6.2.2 Optimization of dip-padding curing parameters

In order to produce Ag coated textile, AgHEC was selected as Ag based nanosol, due its affinity for organic and polymeric fibers, as cotton and polyamide textiles, used in this study. The textiles were functionalized through dip-dapping-curing method (Fig. 4.1). Despite the high aspectatives, preliminary studied did not show good results. In particular, the main problem found in functionalization of textile with typical nanophase content (1-0.5wt%) was the formation of burns onto the textile surface, which appeared during curing treatment, due to the large amount of organic matter contained in Ag nanosol. So, an optimization study inherent to dip-padding-curing process conditions was necessary. In particular, Ag content was decreased and the curing temperature was optimized.
Optimization study was carried out on cotton textiles, using AgHEC as Ag nanosol and testing two different Ag content: 0.05 and 0.01 wt%, and three different curing

temperature: 60, 80 and 100°C. The curing time was kept constant at 10 min. The samples produced were showed in Figure 6.5, it was observed the absence of burns on all samples.

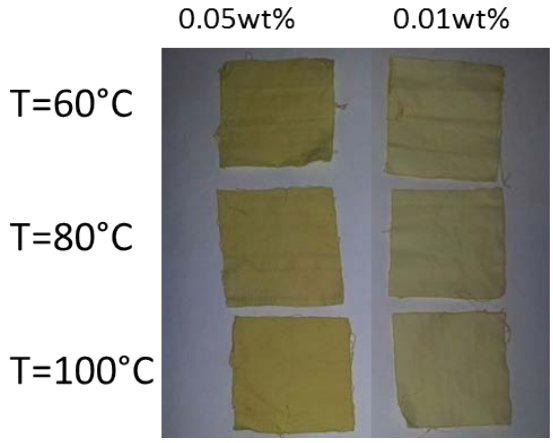

Figure 6.5 Ag-coated cotton textiles produced for dip-padding-curing of diluted samples.

The elemental analysis, performed on washing water by ICP-AES, showed good results in Ag NPs adhesion onto textile (Table 6.2).

Table 6.2 Elemental analysis of washing water for AgHEC- coated cotton textiles samples .

Curing T (° C)	Ag weight loss (%)	Curing T (° C)	Ag weight loss (%)
Ag content (%) = 0.1		Ag content (%) = 0.25	
1° washing			
60	24.08	60	11.84
80	4.86	80	2.96
100	16.63	100	7.26
2° washing			
60	12.32	60	3.86
80	6.02	80	1.55
100	6.45	100	3.86

In the specific, the worse results were obtained by the sample cured at lowest T° (60° C), as expected, whilst the best results were obtained by the sample cured at 80° C.

At the highest curing temperature (100° C), intermediate results were collected, probably the Ag coating was altered by oxidation process [6,7]. So, on the basis of these results, the best condition for the preparation of Ag-coated textiles were:

- Ag content = 0.05 wt%
- Curing temperature = 80°C
- Curing time = 10 min

Analogous tests were performed on standard polyamide textiles, given its widespread in biotechological application and textile market [8-12]. Pre-treated polyamide textiles were coated with AgHEC at two different Ag content: 0.25 and 0.1 wt%. Then, they were dried in oven at 60°C and cured at 80°C for 10 min. The absence of burns in all samples was observed. The elemental analysis results (Table 6.3) showed a poor Ag NPs adhesion onto polyamide textile, in fact the total Ag weight loss was 75.0% and 99.0% for the sample with Ag content 0.25 wt% and 0.1 wt%, respectively.

Table 6.3 Elemental analysis of washing water for AgHEC-coated polyamide textiles samples.

Sample	Ag weight loss (%)
1° washing	
0.1%	95.2
0.25%	71.6
2° washing	
0.1%	89.6
0.25%	12.0
Total	
0.1%	99
0.25%	75

These results clearly demonstrated the unsatisfactory ability of Ag NPs to remain anchored to polyamide supports. Further attempts to coat polyamide textiles with Ag nanophase were made. In order to promote the adhesion of Ag nanosol, a TiO_2 underlying structure was applied on polyamide textile, which should act as a cross

linking media. Specifically, pre-treated polyamide textiles were coated with TiO_2 nanosol: TACR (TiO_2 nanosol, TAC, after purification by anion exchange resin, the process was described in detail in Section 4.1.2) with 1.5 wt% of TiO_2 concentration, dried in oven at 100°C and cured at 130°C for 10 min. Then, they were coated with AgHEC at two different Ag content: 0.25 and 0.1 wt%, dried in oven at 60°C and cured at 80°C for 10 min. Similarly, after post-washing, the ICP analysis on post-washing water was performed. The results (Table 6.4) showed the good adhesion of TiO_2 coating, as expected (seen the burn-out tests results, in previously studies about the self-cleaning textiles production – Chapter 4), with about 1.4 wt% residual TiO_2 content on polyamide textile.

Table 6.4 Elemental analysis results in post-washing water in TiO_2-coated polyamide textile, subsequently coated with AgHEC.

Weight loss (%)		Weight loss (%)	
Ag content (%) = 0.1		Ag content (%) = 0.25	
1° washing			
Ag	81.4	Ag	88.3
TiO_2	5.6	TiO_2	5.7
2° washing			
Ag	25.8	Ag	31.2
TiO_2	3.9	TiO_2	3.0

On the other hand, a substantial Ag weight loss was found. Nevertheless, further experiments needed to optimize such layer by layer strategy. Unfortunately at the time of the present thesis, it was not possible to produce Ag-coated polyamide textiles with good features.

6.2.3 Antibacterial textiles in biotechnological application

The functional properties of optimized Ag-coated textile were assessed by antibacterial tests. They were carried out on AgHEC-coated cotton textiles sample, with 0. 0048 wt% as resulted by ICP-AES analysis.

The antibacterial results (Table 6.5) showed the deficiency of antibacterial activity against mixed microbial cultures, while a good bacterial reduction was recorded in the

test against Klebsiella pneumonia bacteria.

Table 6.5 Bacterial reduction % on Ag-coated cotton fabrics.

Bacterial reduction %	Untreated	Ag-coated textile
Klebsiella pneumoniae (Gram negative)	20	100
Mixed microbial cultures	50	50

Probably, the not excellent antibacterial activity of Ag-coated textile was not sufficient to degrade the mixed microbial cultures that were much more resistant than single microbial cultures, as Klebsiella pneumonia bacteria.

On the other hand, the use of mixed microbial cultures, which do not require sterility, allows lower investments and operating costs than pure microbial cultures, for the global process developed in our specific case, referred to polyhydroxyalcanoates (PHAs) biopolymers production process [13-15].

6.3 Conclusions

Ag-coated cotton textiles were produced and their antibacterial properties tested. A good bacterial reduction was recorded in the test against pure microbial cultures. On the other hand, the bacteria membranes degradation against bacteria in mixed microbial cultures resulted very difficult.

Moreover, the functionalization of polyamide textiles proved much more problematic that cotton textiles, in fact it was not possible to produce Ag-coated polyamide textiles. Next actions involve further experiments inherent to layer by layer strategy and the used of crosslinking agent [16-18] or other Ag nanosols (different from AgHEC sample), in order to improve the affinity and compatibility between Ag NPs and textile support.

6.4 References

[1] K. Sudesh, H. Abe, Y. Doi, Prog. Polym. Sci. 25 (2000) 1503−1555.

[2] J. Yu, L. X. L. Chen, Biotechnol. Prog. 22 (2006) 547−553.

[3] C. Torri, H. Cordiani, C. Samorì, L. Favaro, D.e Fabbri, Journal of Chromatography A, 1359 (2014) 230–236.

[4] M. Blosi, S. Albonetti, F. Gatti, G. Baldi, M. Dondi, Dyes and Pigments 94 (2012) 355–362.

[5] M. Blosi, S. Albonetti, S. Ortelli, A. L. Costa, L. Ortolani, M. Dondi, New J. Chem. 38 (2014) 1401–1409.

[6] P. Pinkhasova, H. Chen, M. W. G. M. Verhoeven, S. Sukhishvilic, H. Du, RSC Adv. 3 (2013) 17954–17961.

[7] A. Ott, S. Ring, G. Yin, W. Calvet, B. Stannowski, Y. Lu, R. Schlatmann, M. Ballauff, Nanotechnology 25 (2014) 455706.

[8] G. N. Yakushenok, A. V. Genis, N. N. Machalaba, A. A. Fetisova, Fibre Chemistry 43 (2011) 10–17.

[9] D. H. Lee, B. G. Min, Fibers and Polymers 15 (2014) 1921–1926.

[10] C. Labaya, J.M. Canal, A. Navarro, C. Canal, Appl. Surf. Sci. 316 (2014) 251–258.

[11] E. M. Aizenshtein, Fibre Chemistry, 45 (2014) 329–335.

[12] M. El Bouchti, H. Hannache, S. Gmouh, N. Hanafi, O. Cherkaoui, Autex Research Journal, 14 (2014) 73–75.

[13] R. Moita, P.C. Lemos, Biopolymers production from mixed cultures and pyrolysis by-products, J. Biotechnol. 157 (2012) 578–583.

[14] T. Shalin, R. Sindhu, P. Binod, C. R. Soccol, A. Pandey, Braz. Arch. Biol. Technol. 57 (2013) 644–652.

[15] R. Moita, A. Freches, P.C. Lemos, Water Research 58 (2014) 9–20.

[16] A. Martin, N. Tabary, L. Leclercq, J. Junthip, S. Degoutin, F. Aubert-Viard, F. Cazaux, J. Lyskawa, L. Janus, M. Bria, B. Martel, Carbohydrate Polymers 93 (2013) 718–730.

[17] X. Cheng, K. Ma, R. Li, X. Ren, T.S. Huang, Antimicrobial coating of modified chitosan onto cotton fabrics, Appl. Surf. Sci. 309 (2014) 138–143.

[18] C. Ammar, Y. El Ghoul, A. El Achar, Textile Research Journal 85 (2015) 171–179.

Chapter 7: ELECTROSPUN NANOFIBERS DOPED WITH NANO-TIO_2 AND NANO-Ag

The second method, used in this work, for the functionalization of textile supports was the spinning technology with the nano-active phase embedded in the textile matrix. This is a more innovative technique than the classical dip-padding-curing method, widely exploited within functional finishing technologies.

Merging biopolymer processing and sol-gel techniques through electrospinning technology, composite nanofibers were developed. In Figure 7.1, the schematic representation of electrospinning process, studied in this work, was shown.

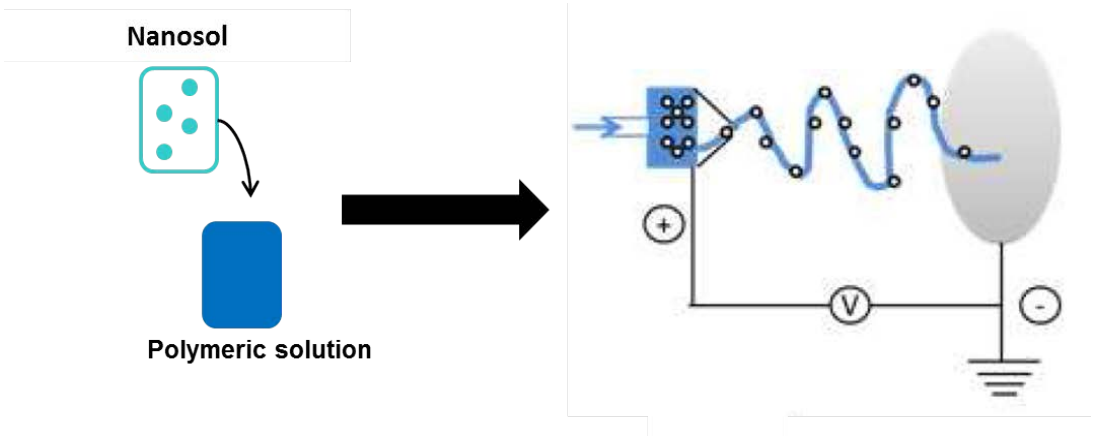

Figure 7.1 Schematic representation of electrospinning process of colloidal nanoparticles into polymeric solution.

In particular, this work aimed to investigate the electrospinning of TiO_2 and Ag colloidal NPs dispersed into keratin solution as powerful tool to obtain multifunctional nanostructured media, coupling keratin and NPs properties. In fact, the electrospinning process allows to obtain fibers with nanometric diameters, starting from polymeric solutions and in this case the addition of NPs in electrospinnable formulations was able to improve the functional properties of electrospun nanofibers.

Keratin was selected as polymeric matrix because it has the capacity of both removal suspended small particles by filtration (due to the controlled porosity and small pore

size) and adsorption of heavy-metals, dyes and VOCs, such as formaldehyde (due to the presence of many functional groups able to bind toxic substances).

Furthermore, nanometals and/or nanometal oxides improve membrane functionalities towards removal of bacteria (antimicrobial, bio-fouling resistant) and photocatalytic properties (removal of drugs, antibiotics, pesticides, and fertilizers).

Thus, Ag and TiO_2 NPs were chosen in order to provide these specific functional properties. Therefore, by embedding inorganic nanoparticles onto keratin nanofibers, it was possible to prepare nanoreactive membranes active for selective removal of different classes of pollutants in water and air treatment.

For the production of nanoreactive membranes it was necessary to prepare stable and electrospinnable keratin solutions in which inorganic NPs showed a good colloidal stability (dispersability), subsequently processed to electrospinning. A deep study relative to the compatibility between two phases (keratin and NPs) was made.

7.1 Experimental Section

7.1.1 Materials

TiO_2 nanosol (NAMA41, 6 wt %) called TAC and Ag nanosol (NAMA39, 4 wt%) called AgSOL were purchased by Colorobbia (Italy). Rhodamine B (dye content ~ 95%) used as target dye, formic acid (reagent grade >95%), poly(ethylene oxide) (PEO, average Mv 400.000), $Na_2S_2O_5$, NaOH, dicycloexhylsulphosuccinate, sodium dodecyl sulphate and TWEEN® 20 were purchased by Sigma Aldrich.

7.1.2 Preparation of electrospinnable formulations

The aim of this activity was to prepare electrospinnable formulations based on dispersions of silver or TiO_2 NPs, into keratin solutions. In this work, keratin extracted from wool and commercial nanosols TAC and AgSOL, as TiO_2 and Ag NPs, respectively, were used, as raw materials to produce electrospinnable formulations.

Keratin was extracted from wool by sulphitolysis with sodium metabisulphite [1]. A wool sample was cleaned by Soxhlet with petroleum ether to remove fatty matter, washed with distilled water and conditioned at 20 °C and 65 % relative humidity for 24 h. Successively, 5 g of cleaned and conditioned fibers were cut in snippets of some

millimeters and treated with 100 ml of a solution containing urea (8 M), $Na_2S_2O_5$ (0.5 M) adjusted to pH 6.5 with NaOH (5 N), under shaking for 2 h at 65° C. The mixture was filtered through 5 μm pore-size filter and dialyzed against distilled water in a cellulose tube (molecular cut off 12–14 kDa) for 3 days, changing the distilled water four times a day. The keratin aqueous solution obtained after dialysis was freeze-dried into keratin powder.

7.1.2.1 Dispersability tests

In the first step, the solubility and colloidal stability of keratin in the selected solvent: formic acid and water were studied by dispersability tests, in order to identify parameters (pH, concentration, additives, conductivity, viscosity) suitable for obtaining stable and electrospinnable solutions. Keratin powder was dissolved in formic acid and in water, with a concentration equal to 15 wt%, at room temperature under magnetic stirring overnight (about 15 h). Using water, as solvent, the addition of different chemical compounds was needed in order to increase solution viscosity and/or keratin solubility. The complete list of the solutions prepared was shown in Table 7.1.

Table 7.1 List of the water based solutions.

Sample Code	Keratin concentration (% w/w)	Additional compound	Additional compound concentration (% w/w)
Test 1	10	-	-
Test 2	12	-	-
Test 3	10	NaCl	1%[a]
Test 4	10	NaCl	3%[a]
Test 5	10	Na_2HPO_4	1%[a]
Test 6	10	Na_2HPO_4	3%[a]
Test 7	10	Buffer pH 10	90%[b]
Test 8	10	Buffer pH 10	50%[b]
Test 9	6	Buffer pH 10	50%[b]
Test 10	10	Formic acid	1%[b]
Test 11	10	SDS	1%[b]
Test 12	12	SDS	1%[b]
Test 13	5	PEO	2%[b]

[a] Percentage on keratin content
[b] Percentage on solution content

On the basis of results, obtained in previous tests, in order to improve electrospinnability, poly(ethylene oxide) was added to water based keratin solutions. So, a brief study to optimize the electrospinnable water based keratin formulations was carried out through viscosity measurements, performed by rheometer Anton Paar Physica MCR 301 (Anton Paar GmbH, Austria) equipped with a temperature controller Peltier PTD 200 and Rheoplus v2.66 software, used for data processing. The analyses were made at 20 °C with a plate-cone system (diameter: 75 mm, cones angle: 1°, truncation: 45 mm) and varying the shear rate in the range: 0.01 – 10 000 s^{-1}.

Then, the analogous dispersability tests were carried out in presence of TiO_2 and Ag NPs studying the compatibility of nanoparticles with keratin solutions. So, nanosols were added to both formic acid and water-based keratin solutions, with 3 wt% concentration on keratin content. In order to increase stability, in water based keratin solutions containing Ag NPs, the addition of surfactant was needed. In particular, different commercial surfactants (namely, TWEEN® 20, dicycloexhylsulphosuccinate and sodium dodecyl sulfate (SDS)) were added with 1 wt% concentration on keratin content, and tested.

The optimization studies showed that the best electrospinnable formulation contained mix PEO/keratin. Finally, the stability of nanosol in poly(ethylene oxide) (PEO) was evaluated by some dispersability tests without keratin. Particularly 2.1 g of PEO was dissolved in water under magnetic stirring for 30 minutes at a concentration of 7 wt%, then Ag or TiO_2 nanosols were added reaching solid loadings of 1, 3 and 6 wt%, and keeping the solution stirred for 15 hours at room temperature. For comparison “blank” sample, a water solution containing PEO (7 wt%) was kept under stirring for 15 hours. Dynamic light scattering technique (DLS - already described in detail in Section 4.1.4) was used to evaluate the nanoparticles stability on the PEO solutions by monitoring the hydrodynamic diameter of particles and assessing the particle size distribution.

7.1.3 Electrospinning process optimization

On the basis of results obtained in dispersabiliy tests, optimized electrosponnable formulation were prepared. Consequently suspensions containing nanoparticles, PEO and keratin were produced as follows for electrospinning. Freeze-dried keratin powder

was added to 5 g of de-ionized water till a concentration of 7 wt% and stirred at room temperature for 18 h. Similarly PEO was dissolved in 5 g of de-ionized water till a concentration of 7 wt%. After 6 hours of stirring, the nanosols were added to the PEO solution and kept under stirring for 18 h at room temperature. The solutions of PEO with nanosols and keratin were mixed following a weight ratio of 30:70 respectively and stirred for at least 2 h before electrospinning. The nanosols were added to the PEO solutions reaching a nanoparticle concentration of 3 wt% with respect to the final keratin content.

The formulations were electrospun using an electrospinning set-up composed of a plastic syringe filled with about 4 mL of solution, a high-precision syringe pump (KDS200, KD Scientific Inc.), and a stainless steel tip with an internal diameter of 0.2 mm connected to the syringe. The tip was electrically connected to a high-voltage generator (SL50 by Spellman). A stainless steel plate (20x20 cm area) was placed in front of the tip as nanofiber collector. The collector was electrically grounded. Processing conditions were deeply investigated changing the main parameters: flow-rate from 0.001 to 0.05 mL min^{-1}, voltage from 20 to 35 kV and distance from 15 to 30 cm. In electrospinning, environmental conditions can affect the nanofiber morphology and process stability [2-4] therefore temperature and relative humidity of the electrospinning room were recorded (by Escort RH iLog datalogger) and controlled. Temperature was maintained in the range of 25-30° C and relative humidity was maintained between 40 and 50 %. Optimal experimental process parameters, reported in Table 7.2, were used to electrospin the formulations.

Table 7.2 Optimal experimental electrospinning parameters

Parameter	Value
Applied voltage	25 kV
Flow rate	0.01 mL min^{-1}
Tip-to-collector distance	20 cm

7.1.4 Characterization of electrospun nanofibers

A deep morphological characterization by FE-SEM analysis, using Carl Zeiss Sigma NTS Gmbh Öberkochen (Germany), on electrospun keratin/PEO nanofibers produced, was carried out and structural features of samples were correlated to electrospinning process. In particular, the collection of about 50 images was made, on 4x4 cm area of electrospun keratin/PEO nanofibers samples, with the aim to carry out an image analysis and so statically characterize and quantify the defects produced during electrospinning process. The results of such analysis were reported as output of "Nanotwice" project and contributed to the definition of design of experiment (DOE).

7.1.5 Functional properties evaluation

The functional properties of electrospun nanofibers with silver and titanium dioxide NPs were verified by antibacterial and photocatalytic tests.

Antibacterial tests against Escherichia coli (ATCC 11229) were based on AATCC 100 Test Method. The procedures were the following.

a. The samples with titanium dioxide (as well as the corresponding reference sample composed of electrospun keratin/PEO samples without nanoparticles) were subjected to UV irradiation 24 h before the contact with bacteria inoculum (activation). 1 mL of bacteria inoculum containing 1.5-3 × 105 CFU/mL was put on each sample. Then the samples were exposed to UV light for 1 h at about 20 °C and 65 % RH. After this time 100 ml of sterile buffer were added to each sample, the buffer was then dilute ten times and pleated on Petri dishes with suitable agar. The Petri dishes were incubated at least 24 h at 37° C, then the colonies were counted.
b. 1 ml of bacteria inoculum containing 1.5-3 × 105 CFU/mL was put on the samples with silver and on the corresponding reference sample without nanoparticles. Then the samples were incubated at 37 °C for 1 h. After this time 100 mL of sterile buffer were added to each sample, the buffer was then dilute

ten times and pleated on Petri dishes with suitable agar. The Petri dishes were incubated at least 24 h at 37° C, then the colonies were counted.

Bacterial reduction was calculated using the Eq. 6.2.

Photocatalytic tests were performed using as a model reaction the degradation of the Rhodamine B dye (RhB). The photocatalytic degradation of RhB was carried out in a beaker at room temperature, following the procedure described in Section 4.1.7.2 "TiO_2-coated textile (b)". In the specific, 0.03 g of electrospun nanofibers containing 3 wt% of TiO_2 NPs were soaked in 25 mL of RhB aqueous solution (3.5 mg/L) and UV-irradiated. Prior to irradiation, the system was kept in the dark for 1 h to ensure the establishment of an adsorption/desorption equilibrium between nanofibers and RhB dye. The sol containing the electrospun sample was stirred and UV irradiated. A sample without addition of TiO_2 was considered as reference. Photocatalytic efficiency was calculated, after 120 min of irradiation, by the Eq. 4.3. The details inherent to UV irradiation and spectrophotometric measurements (used to determine photocatalytic efficiency) were described in Section 4.1.7.1.

7.2 Results and discussion

7.2.1 Optimization of electrospinnable formulation in selected solvents

The solubility and stability of keratin in the selected solvent: formic acid and water were studied by dispersability tests, in order to identify parameters (pH, concentration, additives, conductivity, viscosity) suitable for obtaining stable and electrospinnable solution.

Dissolving keratin powder (15 wt%) in formic acid, a stable solution was obtained, as expected [5]. On the other hand, the dissolution in water gave rise to some problems. In fact, the addition of different chemical compounds was necessary to dissolve keratin powder in water in order to increase solution viscosity and/or keratin solubility. Different tests were carried out, varying the composition (Table 7.1). The results showed different final states (i.e. liquid, gel, solid). In the specific Test 1, 3, 5, 8, 11, 12 and 13 formed liquid, Test 2, 4, 6 and 8 formed gels and Test 7 and 10 formed solid. In

fact, keratin, for its nature, tends to form gels at high concentration in water [6] , as observed in Figure 7.2, but for electrospinning a high concentration was required to reach a sufficient viscosity for producing nanofibers.

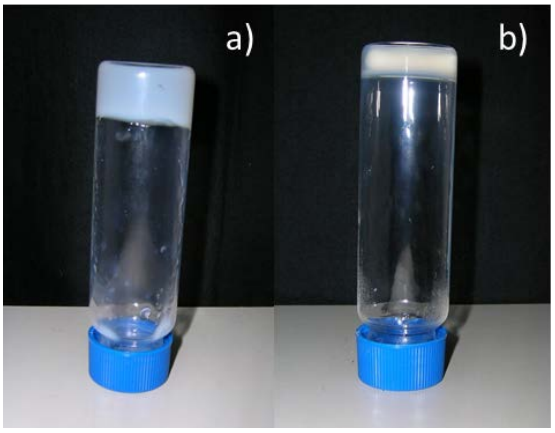

Figure 7.2 Gels of keratin from water based solutions with the addition of a) 3% NaCl (Test 4) and b) 3% Na_2HPO_4 (Test 6).

Formulations, producing liquid solutions (keratin in acid formic and Test 1, 3, 5, 8, 11, and 13 in water), were electrospun using the electrospinning set-up (Table 7.2). These preliminary electrospinning tests aimed to optimize the electrospinnable formulations. Keratin solutions in formic acid produced thin nanofibers with few defects (Fig. 7.3).

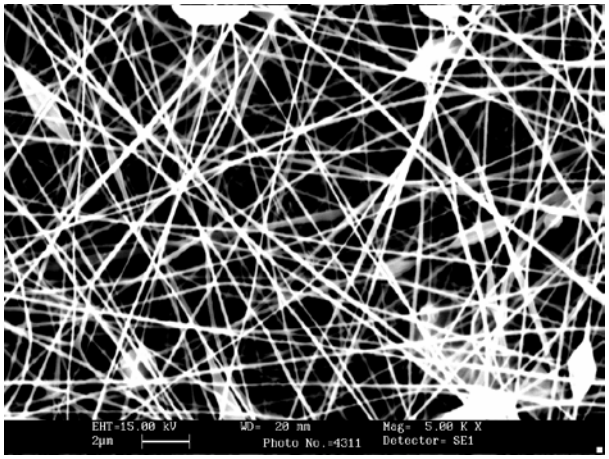

Figure 7.3 Electrospun keratin nanofibers from 15% keratin in formic acid.

On the contrary, water based keratin solutions did not produce nanofibers, excepting for the keratin/PEO blend solutions (Fig. 7.4). However, it worth to note that in some cases signs of fibrous structures were visible, as shown in Figure 7.4b, c and d. Therefore, proving the best results, mix keratin/PEO was further investigated.

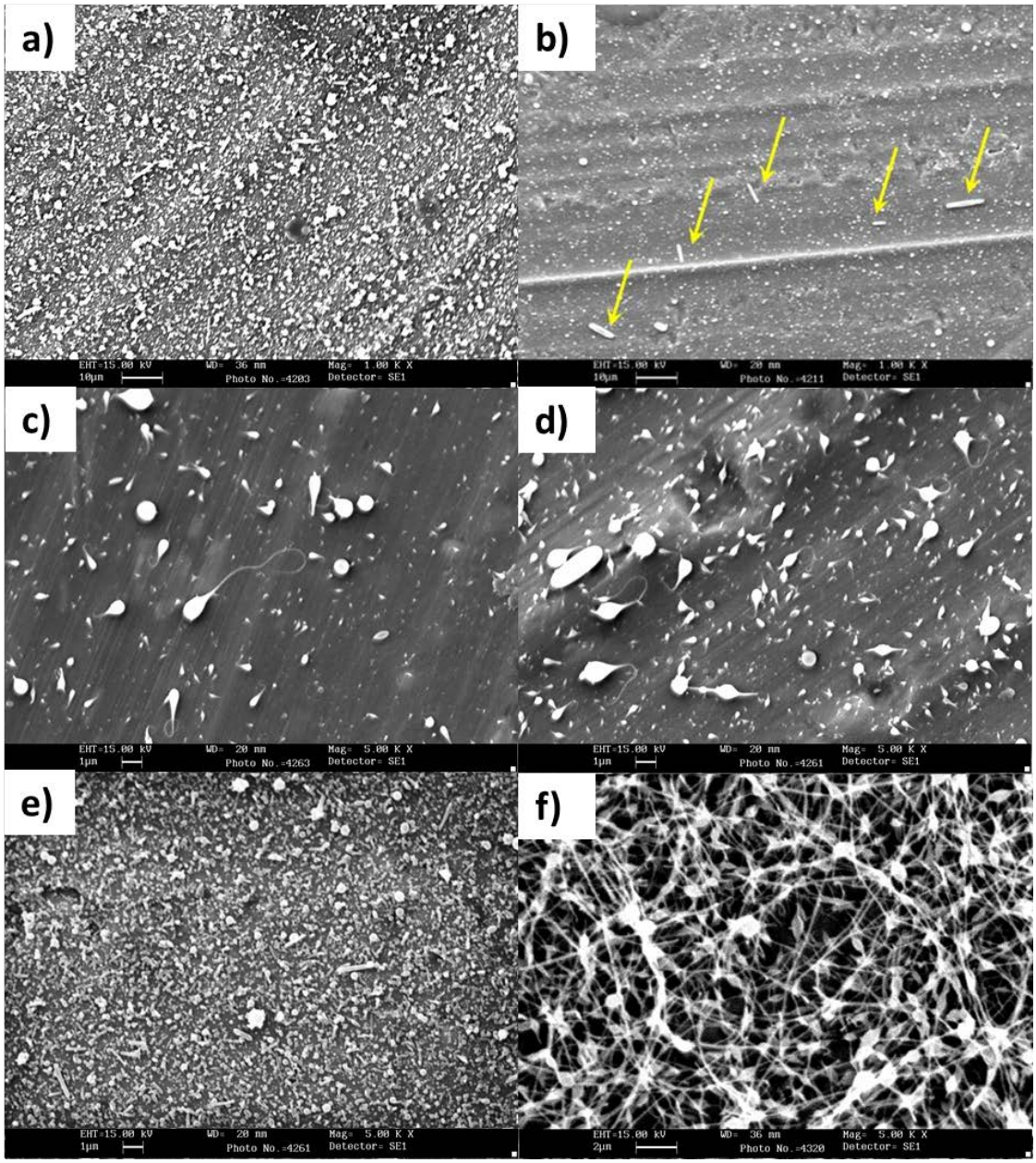

Figure 7.4 Electrospun keratin nanofibers from water based solutions. a) Test 1, b) Test 3, c) Test 5, d) Test 9, e) Test 11 and f) Test 13.

Viscosity of the two electrospinnable keratin solutions (formic acid and water based keratin/PEO solutions) was measured in order to characterize their rheological behaviour (Fig. 7.5).

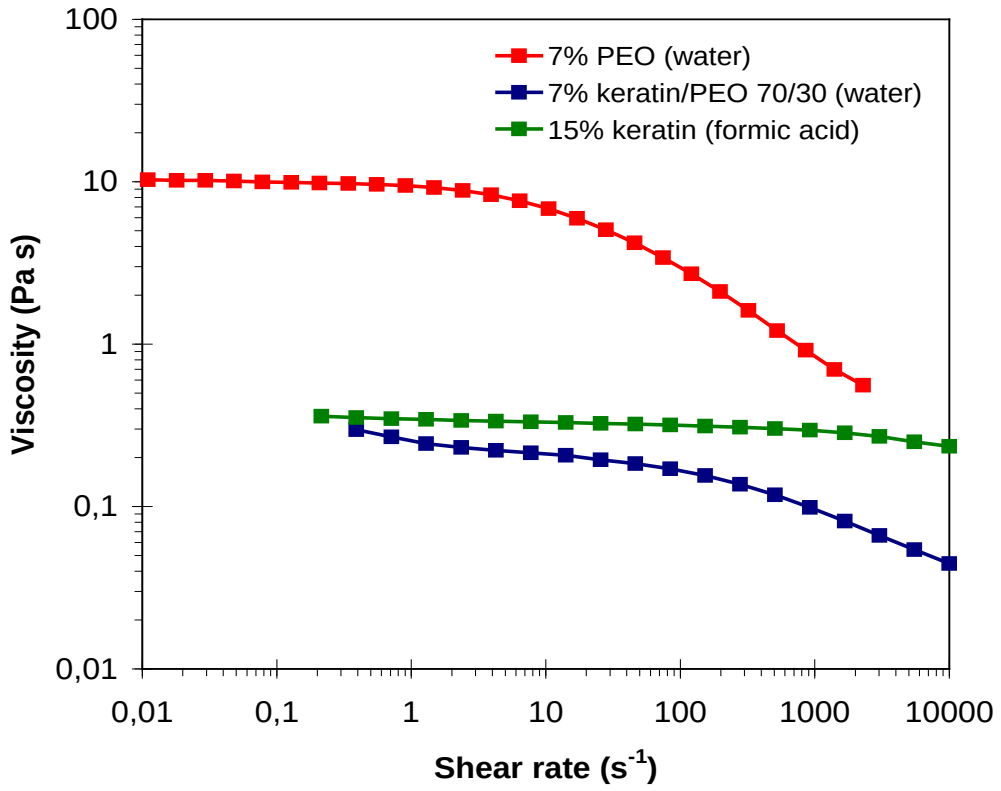

Figure 7.5 Viscosity measurements of electrospinnable keratin solutions compare with electrospinnable PEO solution.

Keratin formic acid based solution showed a quasi-Newtonian behaviour, viscosity did not depend on the shear rate.

On the contrary, keratin/PEO water based solution (weight ratio 70:30 with a total concentration of 7 wt%) had a non-Newtonian behaviour with an evident shear thinning at high shear rate that reduces the viscosity. This could explain the different morphologies of the nanofibers produced with the solutions. In fact, water based solution had a large number of defects (mainly beads) as compared with electrospun keratin nanofibers obtained from formic acid solution.

Moreover, it worth to be noted that both keratin solutions showed a viscosity one order of magnitude lower than the viscosity of electrospinnable PEO solution at low shear rate. But PEO solution had a great shear thinning that reduced the viscosity at high shear rate. Formic acid keratin solution having a quasi-Newtonian behaviour reduced the different in viscosity at high shear rate, which was the condition of the nanofiber forming process.

On the contrary, the non-Newtonian behaviour of water-based keratin solution further reduced the viscosity of this solution making possible the production of defects. Anyhow, mix keratin/PEO remained to be the best candidate to produce water based electrospinnable formulations.

Colloidal stability represents a key point in order to provide a suitable suspension for the electrospinning process, so a deep step by step evaluation was carried out. In order to assess the stability of nanosol in PEO, some dispersability tests (without keratin) were performed. Dynamic light scattering (DLS) was used to evaluate the NPs stability in the PEO solutions by monitoring the hydrodynamic diameter of particles and assessing the particle size distribution. DLS results (Fig. 7.6) confirmed the good stability showing no significant agglomerates.

From the size distribution curves, it could be observed a diameter decrease by adding progressive amounts of nanoparticles. In particular at low solid concentrations the signal due to PEO, as shown in the “blank”, prevails on the signal corresponding to the NPs so conditioning the mean value of the curves.

As highlighted by Table 7.3, when the NPs concentration was low (1 wt%) the average diameter was closer to the blank value and no differences were detected between TiO_2 and Ag samples.

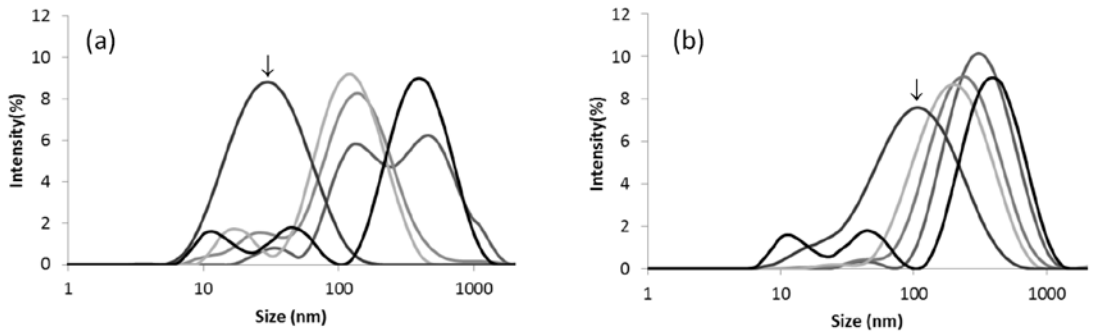

Figure 7.6 Particle size distribution of a) TAC and b) AgSOL nanosols at solid concentrations of 1 wt% (dark grey), 3 wt% (grey) and 6 wt% (light grey) in PEO solutions compared to aqueous nanosol (black curve indicated by the arrow) as reference sample and PEO solution (black curve) as blank sample.

Table 7.3 Average hydrodynamic diameters measured by DLS technique on Ag and TiO_2 nanosols in PEO solution.

Sample	AgSOL		TAC	
	d_{DLS} (nm)	PDI	d_{DLS} (nm)	PDI
Reference (aqueous nanosol)	73	0.3	26	0.3
1 wt%	271	0.3	265	0.6
3 wt%	217	0.4	107	0.6
6 wt%	175	0.4	87	0.5
Blank (PEO in water)	318	0.6	318	0.6

On the contrary, for higher amount of solid added (3-6 wt%) the signal by NPs became stronger and the hydrodynamic diameter was more consistent with the real hydrodynamic size. In fact the detected sizes for a sol concentration of 3 or 6 wt% were increased with respect to the reference sols in a different manner for Ag and TiO_2 and probably due to the presence of NPs embedded into the PEO matrix. The PDI values were lower for the reference samples containing the nanoparticles only, while they increased when PEO was added, reflecting the polymer polydispersity. The suspension stability of particles with PEO was a significant goal because the polymer acted as ligand and played a key role in the homogenization of electrospinnable suspensions. Among the prepared concentrations the more suitable NPs content was evaluated to be 3

wt%. An excellent stability over time was demonstrated, in fact no precipitation phenomenon occurred till several months [7].

Further dispersability tests were performed, testing the stability of samples containing keratin and NPs. In fact, it was necessary to study the compatibility of NPs with keratin in the conditions selected for the process. TiO_2 and Ag nanosols (TAC and AgSOL samples) were added to both formic acid and water based keratin solutions. The addition of nanosol to formic acid solution produced the precipitation of the proteins, constituting keratin, because nanosols were water based dispersions, limiting the use of formic acid as solvent.

On the contrary, the addition of nanosols to water based keratin solutions produced, in general, liquid dispersions. Only, in the case of Ag nanosol some flakes were observed, probably due to the interaction between highly reactive metallic silver and sulphur groups of keratin proteins. In order to increase dispersion stability, in the formulations containing Ag NPs, different commercial surfactants were tested: Tween 20 (T), dicycloexhylsulphosuccinate (DCSS) and sodium dodecyl sulphate (SDS).

The Figure 7.7 showed that only SDS (Fig. 7.7c) produced a stable dispersion of Ag nanosol in keratin solution.

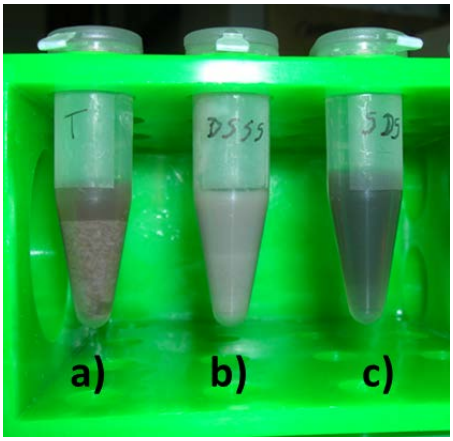

Figure 7.7 Stability evaluation of Ag nanosol in water based keratin solutions with the addition of : a) Tween 20, b) dicycloexhylsulphosuccinate and c) SDS.

Summarizing, the results inherent to optimization studies showed the incompatibility of formic acid with aqueous nanosols, so the water was chosen, as solvent. The electrospinnability of keratin from water solution can be performed if water soluble polymers were added to the electrospinning solution. In the specific, poly(ethylen oxide) (PEO) represented a perfect candidate to promote electrospinning of keratin from water, due to its action of enhancing electrospinnability of proteins [8-10]. In particular, viscosity tests revealed that the optimized formulation contained a mix keratin/PEO with a weight ratio of 70:30 respectively, at a total concentration of 7 wt%. The final optimized formulation provided keratin/PEO solutions with 3 wt% of nanosol (i.e. silver or titanium dioxide). In the presence of Ag nanosol, SDS was added, at the concentration of 1 wt% on keratin content, as surfactant agent, in order to avoid the formation of flakes.

7.2.2 Characterization of electrospun nanofibers

Initially, water based keratin/PEO solutions (without NPs) were electrospun.

Excellent results, in general, were obtained.

A deep morphological analysis by FE-SEM, on electrospun keratin/PEO nanofibers was carried out in order to characterize and quantify the defects present, originated during electrospinning process. They were mainly beads, films and holes. In Figure 7.8, an example for each possible defect, found on electrospun keratin/PEO nanofibers, was shown.

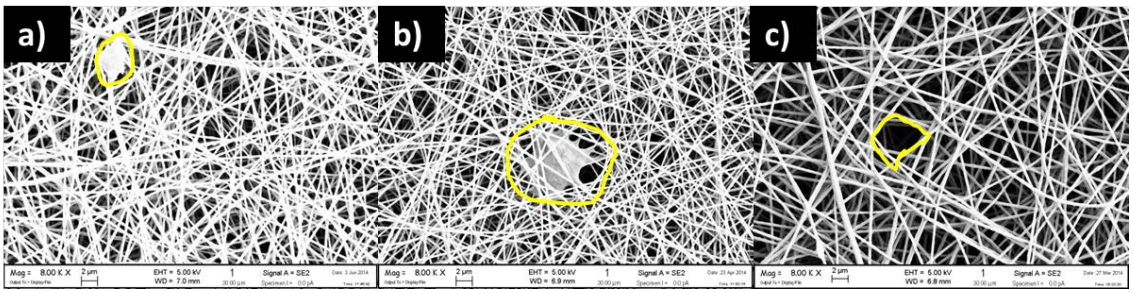

Figure 7.8 Representative images by FE-SEM of possible defects: a) beads, b) film and c) hole. The imagines were made on electrospun keratin/PEO nanofibers samples.

Furthermore, the FE-SEM images were collected, with the aim to optimized the parameters of electrospinning process. The electrospinning process parameters: voltage, flow rate and tip-to-collector distance were modified finding to minimize the number of defects, on the basis of results obtained from image analysis. The optimized electrospinning parameters were reported in Table 7.2.

Electrospun keratin nanofibres as spun were not stable in water, but were water soluble. A thermal stabilization process was needed in order to give water stability to keratin. Water stability was required for water filtration and humid gasses and obtained with a thermal stabilization process in the following conditions: temperature = 180° C and time = 2 h, without compromising the features of nanofibrous structure [11].

At last, water based keratin/PEO solutions with 3 wt% of NPs (Ag and TiO_2 nanosols) were electrospun. The adding of NPs caused the production of an higher number of defects during the electrospinning process than pure keratin/PEO solutions (Fig. 7.9). Anyhow, good nanofibers were obtained.

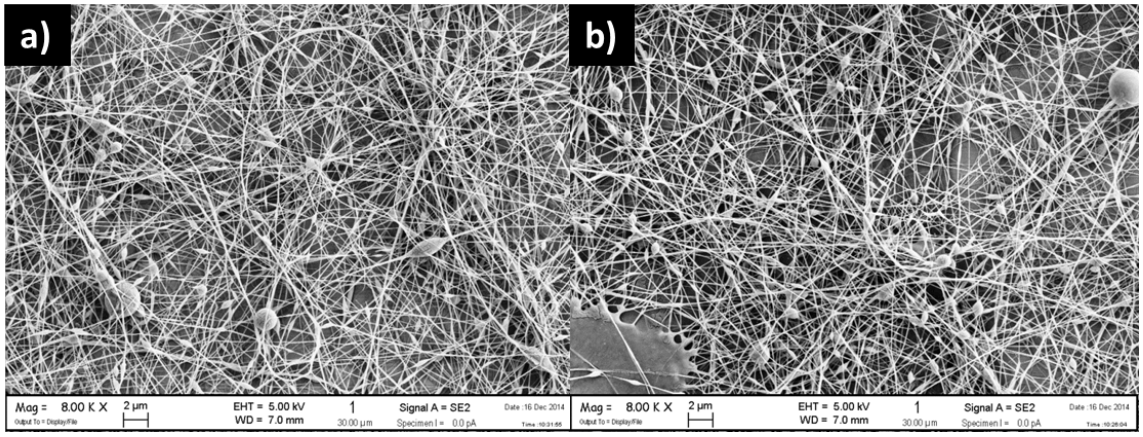

Figure 7.9 FE-SEM images of electrospun keratin/PEO nanofibers functionalized by a) TiO_2 and b) Ag NPs.

7.2.3 Antibacterial and photocatalytic results

Antibacterial property and photocatalytic activity of the NPs embedded into the electrospun nanofibers were assessed.

Antibacterial tests were carried out using *E. coli* on nanofibers with silver and titanium dioxide NPs. The results were reported in Table 7.4.

Table 7.4 Antibacterial results of TiO_2 and Ag NPs functionalized keratin/PEO nanofibers.

Sample	Bacterial reduction (%)
keratin/PEO+TiO_2	97
keratin/PEO+Ag	95

Both kinds of materials showed excellent antibacterial properties as sign that the nanoparticles can exert their functions even if embedded in keratin nanofibers. Both TiO_2 and Ag NPs functionalized nanocomposite materials could be exploited as potential antibacterial nanoreactive membranes.

Photocatalytic tests based on model reaction of Rhodamine B dye (RhB) were performed. The photodegradation showed promising photocatalytic properties for the TiO_2 NPs functionalized electrospun nanofibers. The results in terms of photocatalytic efficiency were listed in Table 7.5.

Table 7.5 Photocatalytic results of TiO_2 NPs functionalized keratin/PEO nanofibers.

Sample	Photocatalytic efficiency (%)
keratin/PEO+TiO_2	53%
keratin/PEO	14%
Control[a]	12%

[a] Degradation test of RhB solution carried out without electrospun material.

Despite the value of keratin/PEO+TiO_2 reached 53%, thus the photodegradation was not complete, good results were shown. In fact, a considerable activity improvement in comparison with the data obtained by the electrospun sample without TiO_2 NPs, which showed the same activity of the solution alone (control), was obtained. Since the performances can be probably enhanced by increasing the content of TiO_2, these results were surely very interesting. In fact, the main goal was that TiO_2, even if added in very

small quantity and if embedded in a polymeric matrix, acted as effective photocatalyst transferring its functional properties on the nanocomposite material.

7.3 Conclusions

Concluding, the possibility to use water effectively, as solvent, instead of toxic solvents, such as formic acid, for the production of keratin based nanofibers by electrospinning was demonstrated. The use of water was required for compatibility with aqueous colloids which allowed to attain good dispersion of NPs in the polymer nanofibers and overcome safety issues, respect to the wider use of nanopowders. In fact, existing papers report the electrospinning of TiO_2 and Ag nanopowders (or their precursors) dispersed into formic acid solutions of polyamides [12-16]. Besides, a practical benefit of embedding colloids in electrospun nanofibers was that both unprocessed and final materials can be handled more easily than nanopowders alone. Thus, the use of water and aqueous colloids, as solvent and NPs functionality, respectively, allowed a more eco-friendly, easily scalable and versatile electrospinning process. Finally, functional properties of the NPs embedded in the electrospun nanofibres, in degrading organic materials and/or in killing micro-organisms, were assessed.

The results demonstrated that electrospun keratin nanofibers guaranteed nanoparticle properties.

7.4 References

[1] J.A. Maclaren, B. Milligan, Wool Science: The Chemical Reactivity of the Wool Fibre; Science Press: Marrickville, New South Wales, 1981.

[2] S. De Vrieze, T. Van Camp, A. Nelvig, B. Hagstrom, P. Westbroek, K. De Clerck, J. Mater. Sci. 44 (2009) 1357–1362.

[3] O. Hardick, B. Stevens, D.G. Bracewell, J. Mater. Sci. 46 (2011) 3890–3898.

[4] Y. Cai, M. Gevelber, J. Mater. Sci. 48 (2013) 7812–7826.

[5] A. Alemdar, Y. Iridag, M. Kazanci, Int. J. Biol. Macromol. 35 (2005) 151–153.

[6] A. Idris, R. Vijayaraghavan, U. A. Rana, A. F. Pattia, D. R. MacFarlane, Green Chem. 16 (2014) 2857–2864.

[7] A. Varesano, C. Vineis, C. Tonetti, D. O. Sanchez Ramirez, G. Mazzuchetti, S. Ortelli, M. Blosi, A. L. Costa, Curr. Nanosci. 11 (2015) 41–48.

[8] J. Xie, Y.L. Hsieh, J. Mater. Sci. 38 (2003) 2125–2133.

[9] A. Aluigi, C. Vineis, A. Varesano, G. Mazzuchetti, F. Ferrero, C. Tonin, Eur. Polym. J. 44 (2008) 2465–2475.

[10] A. Varesano, A. Aluigi, C. Vineis, C. Tonin, J. Polym. Sci. Part B: Polym. Phys. 46 (2008) 1193–1201.

[11] A. Varesano, C. Vineis, C. Tonetti, D. O. Sanchez Ramırez, G. Mazzuchetti, J. Appl. Polym. Sci. 131 (2014) 40532.

[12] S.W. Park, H.S. Bae, Z.C. Xing, O.H. Kwon, M.W. Huh, I.K. Kang, J. Appl. Polym. Sci. 112 (2009) 2320–2326.

[13] H.R. Pant, M.P. Bajgai, K.T. Nam, Y.A Seo, D.R. Pandeya, S.T. Hong, H.Y. Kim, J. Hazard. Mater. 185 (2011) 124–130.

[14] H.R. Pant, D.R. Pandeya, K.T. Nam, W. Baek, S.T. Hong, H.Y. Kim, J. Hazard. Mater. 189 (2011) 465–471.

[15] Q. Shi, N. Vitchuli, J. Nowak, J. Noar, J.M. Caldwell, F. Breidt, M. Bourham, M. McCord, X. Zhang, J. Mater. Chem. 21 (2011) 10330–10335.

[16] M. Lombardi, P. Palmero, M. Sangermano, A. Varesano, Polym. Int. 60 (2011) 234–239.

Chapter 8: CONCLUSIONS

In this thesis, self-cleaning and antibacterial textiles, through the application of TiO_2 and Ag based nanostructured coatings have been developed. The production of TiO_2 and Ag functionalized materials was achieved both by the classical dip-padding-curing method and by the innovative electrospinning process to obtain nanofibers doped with nano-TiO_2 and nano-Ag. The functionalization of textile supports, starting from nanosols, transferred to the support the functional properties of nanostructured coating. In order to optimize the production of functionalized textiles, starting from lab-made and commercial nanosols, the study focused on the comprehension of mechanisms involved in the photocatalytic and antibacterial processes and on the real applicability of the production. Thus, through nano-TiO_2 and nano-Ag based coatings it was possible produce self-cleaning and antibacterial textiles.

A deep investigation on relationship between nanosol and nanocoating properties was performed. In order to identify the factors affecting the nano-TiO_2 photocatalytic reactivity, an exploratory study on photocatalytic mechanism was carried out. The performances of self-cleaning textiles have been optimized on the basis of a "performance by design" approach. Following the same method, antibacterial cotton based textiles, functionalized by Ag NPs, were produced.

Furthermore, the development of risk remediation strategies, based on "safety by design" approach, was carried out with the aim of controlling the biological reactivity of TiO_2 NPs. Merging the biological responses and photocatalytic performance of modified TiO_2 NPs (after the application of risk remediation strategies), the SiO_2 coating resulted the best strategy.

Finally, the innovative spinning technology with functionality embedding was studied. In particular, we used the electrospinning process. Composite keratin based nanofibers, functionalized by TiO_2 and Ag NPs, were developed. The optimization studies aimed at the preparation of electrospinnable formulations led to the use of water based keratin/PEO mix that favored the TiO_2 and Ag NP embedding, starting from aqueous nanosols. Therefore, the use of an eco-friendly, easily scalable and versatile electrospinning process to produce multifunctional membranes with nanofibrous

structure was demonstrated. The functionalization with TiO_2 and Ag NPs, providing photocatalytic and antibacterial properties, allowed to increase the performances of these composite nanomaterials. Their potential use as multifunctional filter media was confirmed.

The Figure 8.1 summarizes the essential activities and the main results obtained on

- self-cleaning and antibacterial textiles
- risk remediation strategies, based on “safety by design” approach
- nanofibers based multifunctional filter media.

The obtained results could drive industrial scale-up of functionalized textile processes towards a “technological transferability” concept. This is easily feasible since simplicity is the key characteristic of dip-padding-curing method. Moreover, regarding spinning technology, the use of water based formulations allow a more eco-friendly, easily scalable and versatile process, avoiding the use of organic (toxic) solvent.

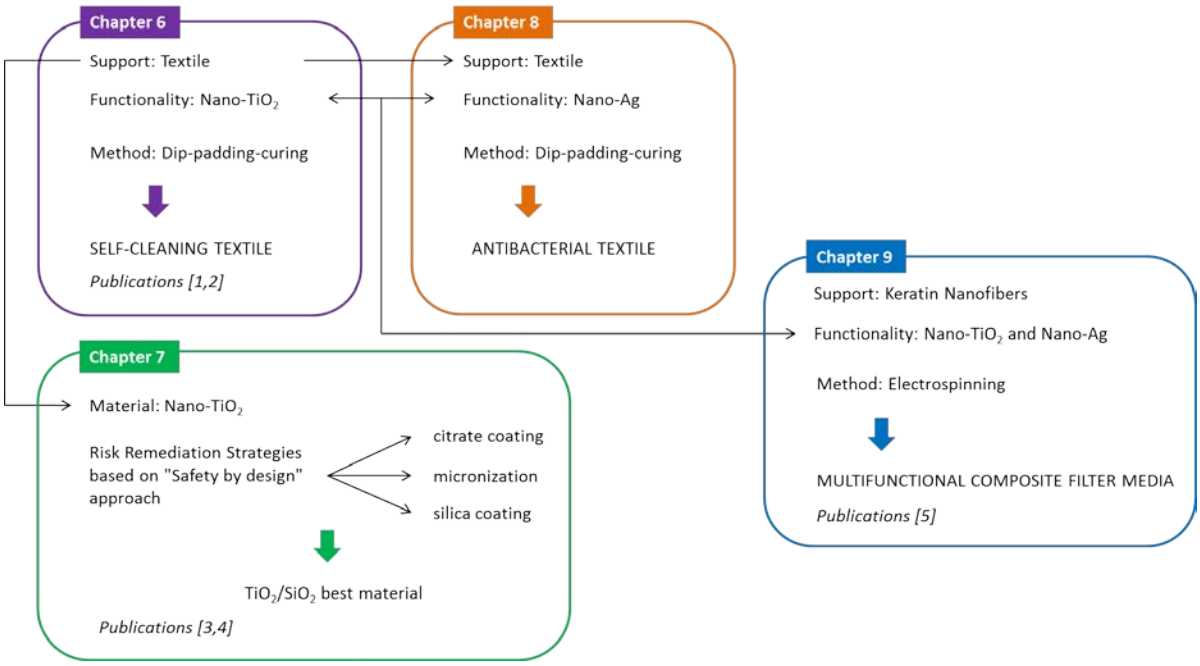

Figure 8.1 Schematic representation of essential activities and main results, with relative publications based on this thesis, for each chapter.

8.1 References

[1] A.L. Costa, S. Ortelli, M. Blosi, S. Albonetti, A. Vaccari, M. Dondi, Chem. Eng. J. 225 (2013) 880–886.

[2] S. Ortelli, M. Blosi, S. Albonetti, A. Vaccari, M. Dondi, A.L. Costa, J. Photochem. Photobiol. A: Chem. 276 (2013) 58–64.

[3] D. Gardini, M. Blosi, C. Delpivo, S. Ortelli, A.L. Costa, J. Phys. Conf. Ser. 429 (2013) 012052.

[4] S. Ortelli, M. Blosi, C. Delpivo, D. Gardini, M. Dondi, I. Gualandi, D. Tonelli, V. Aina, I. Fenoglio, A. Gandhi, S. Tofail, A.L. Costa, J. Photochem. Photobiol. A: Chem. 292 (2014) 26–33.

[5] A. Varesano, C. Vineis, C. Tonetti, D. O. Sanchez Ramirez, G. Mazzuchetti, S. Ortelli, M. Blosi, A. L. Costa, Curr. Nanosci. 11 (2015) 41–48.